A Boundary Element Method with Surface Conductive Absorbers for 3-D Analysis of Nanophotonics

by

Lei Zhang

B.Eng., Electrical Engineering, University of Science and Technology of China (2003)
M.Eng., Electrical Engineering, National University of Singapore (2005)
M.S., Computation for Design and Optimization, Massachusetts Institute of Technology (2007)

Submitted to the
Department of Electrical Engineering and Computer Science
in partial fulfillment of the requirements for the degree of
Doctor of Philosophy in Electrical Engineering and Computer Science
at the
MASSACHUSETTS INSTITUTE OF TECHNOLOGY
September 2010

© Massachusetts Institute of Technology 2010. All rights reserved.

Author .....
Department of Electrical Engineering and Computer Science
June 30, 2010

Certified by .....
Jacob K. White
Professor of Electrical Engineering and Computer Science
Thesis Supervisor

Certified by .....
Steven G. Johnson
Associate Professor of Mathematics
Thesis Supervisor

Accepted by .....
Terry P. Orlando
Chair, Department Committee on Graduate Students

A Boundary Element Method with Surface Conductive Absorbers for 3-D Analysis of Nanophotonics

by

Lei Zhang

Submitted to the Department of Electrical Engineering and Computer Science
on June 30, 2010, in partial fulfillment of the
requirements for the degree of
Doctor of Philosophy in Electrical Engineering and Computer Science

Abstract

Fast surface integral equation (SIE) solvers seem to be ideal approaches for simulating 3-D nanophotonic devices, as these devices generate fields both in an interior channel and in the infinite exterior domain. However, many devices of interest, such as optical couplers, have channels that cannot be terminated without generating reflections. Generating absorbers for these channels is a new problem for SIE methods, as the methods were initially developed for problems with finite surfaces.

In this thesis, we show that the obvious approach for eliminating reflections, making the channel mildly conductive outside the domain of interest, is inaccurate. We propose a new method in which the absorber has gradually increasing surface conductivity; such an absorber can be easily incorporated in fast integral equation solvers. We present two types of PMCHW-based formulations to incorporate the surface conductivity into the SIE method. The accuracy of the two-type formulations are examined and discussed using an example of the scattering of a Mie sphere with surface conductivities. Moreover, we implement two different FFT-accelerated algorithms for the periodic non-absorbing region and the non-periodic absorbing region.

In addition, we use perturbation theory and Poynting's theorem, respectively, to calculate the field decay rate due to the surface conductivity. We show a saturation phenomenon when the electrical surface conductivity is large. However, we show that the saturation is not a problem for the surface absorber since the absorber typically operates in a small surface conductivity regime.

We demonstrate the effectiveness of the surface conductive absorber by truncating a rectangular waveguide channel. Numerical results show that this new method is orders of magnitude more effective than a volume absorber. We also show that the transition reflection decreases in a power law with increasing the absorber length.

We further apply the surface conductive absorber to terminate a waveguide with period-a sinusoidally corrugated sidewalls. We show that a surface absorber that can perform well when the periodic waveguide system is excited with a large group-velocity mode may fail when excited with a smaller group-velocity mode, and give an asymptotic relation between the surface absorber length, transition reflections and

group velocity. Numerical results are given to validate the asymptotic prediction.

Thesis Supervisor: Jacob K. White
Title: Professor of Electrical Engineering and Computer Science

Thesis Supervisor: Steven G. Johnson
Title: Associate Professor of Mathematics

Acknowledgments

I would like to take this chance to thank my supervisor, Prof. Jacob K. White. He brought me to this great school in 2005, patiently helped me find my research direction, enlightened me through numerous discussions, and offered me freedom to pursue what I am interested. My sincere appreciation also goes to my co-supervisor Prof. Steven G. Johnson. He is a talented young scientist. His passion in research encourages everyone working with him. I learned everything about nanophotonics from him. He generously proposes his ideas through our discussions, and many ideas in this thesis came from him.

Many thanks should go to members in the Computational Prototyping group. Because of these wonderful colleagues, I really enjoyed working in this group for the five years. I would like to thank Prof. Luca Daniel, for his support and serving as my thesis committee member. I would like to thank our group assistant Chad Collins, who efficiently takes care of all executive stuff in our group. Then I would like to thank my amazing groupmates that includes my five-year officemate Bo Kim, Amit Hockman, Jung Hoon Lee, Brad Bond, Kin Sou, Tarek Moselhy, Homer Reid, Yu-Chung Hsiao, Dmitry Vasilyev, Zohaib Mahmood, Yan Zhao, Kai Pan, Laura Proctor and Steven Leibman.

I also would like to thank Ardavan Oskooi. Part of his thesis is on adiabatic absorber, based on which I worked on the analogue of the idea using surface integral equation method. I spent a summer as an intern in Ansoft Corp., I would like to thank my supervisor there, Dr. Istvan Bardi. I spent another summer in Schlumberger Doll Research in Cambridge, working on inverse algorithms. I would like to thank my advisor Dr. Aria Abubakar, and my friends there, Maokun Li, Jianguo Liu, Lin Liang, and Jiaqi Yang.

The last but not the least, actually the most important, my great thanks go to my beloved wife Yan Li and my parents. Yan and I have been married for nearly four years. I would like to thank for her generous support and care during my study. She is also a PhD student at MIT, I would like to wish her good luck next year to get her

PhD degree. I would like to greatly thank my parents for bringing me to this world, bringing me up, educating me with all their love. I am proud of you two, and I have done and will do my best to let you be proud of me.

Contents

List of Figures

List of Tables

Chapter 1

Introduction

In this thesis, we describe a surface conductive absorber technique for terminating optical channels with the boundary element method, which otherwise has difficulties with waveguides and surfaces extending to infinity. In order to attenuate waves reflected from truncated waveguides, we append a region with surface absorption to the terminations, as diagrammed in Fig. 1-1. The transition between the non-absorbing and absorbing regions will generate reflections that can be minimized by making the transition as smooth as possible. We show how this smoothness can be achieved with the surface absorber by smoothly changing integral-equation boundary conditions. Numerical experiments demonstrate that the reflections of our method are orders of magnitude smaller than those of straightforward approaches, for instance, adding a volume absorptivity to waveguide interior. In addition, We apply the surface absorber to truncate periodic waveguide channels, and show that the difficulty to eliminate transition reflections increases as the group velocity of excited modes decreases. To solve the difficulty, we show that the absorber length should be increased, and provide asymptotic relations between absorber length and group velocity.

1.1 Terminating Waveguide Channels with BEM

Many nanophotonic devices have input/output waveguide channels to couple power/signal into and out of the device system. By introducing a periodic modulation into an elec-

tromagnetic waveguide channel, one can obtain a variety of effects useful for photonic devices [2]: periodicity creates band gaps that can be used to confine light [2], while near the edge of the gap there are "slow light" modes with a group velocity $\to 0$ which can increase light-matter interactions for nonlinear devices [3–5], tunable time delays [6], dispersion compensation [7–12], or other applications. The periodicity can take many forms, such as a waveguide with periodically varying width as in Fig. 1-2 (inset), waveguides with periodic holes [2], "fiber Bragg gratings" with periodic index variation [7, 13], and so on. In this thesis, we consider the application of boundary element methods (BEM) [1, 14–17] to study devices incorporating waveguide channels with uniform or periodic cross section. The boundary element method is a powerful computational technique because it handles homogeneous regions analytically and only discretizes interfaces between materials, and no artificial truncation is needed for the infinite space surrounding a device—however, waveguide-based devices pose a challenge because the input/output waveguide surfaces must still be truncated with some artificial absorber in order to eliminate spurious reflections. In volume-discretization methods like the finite-difference time-domain (FDTD) method [18,19], one must truncate space as well as waveguides, and the traditional solution is a perfectly matched layer (PML) [20–23], but the PML idea is based on an analytic continuation that is not applicable to periodic waveguides [24]. A fallback is an adiabatic absorber, in which some kind of absorption is turned on gradually in order to absorb outgoing waves with minimal reflection [24]. In this thesis, we present the BEM analogue of the adiabatic absorber idea for truncating waveguides, by a gradually increasing surface conductivity that can be efficiently implemented with a surface-only

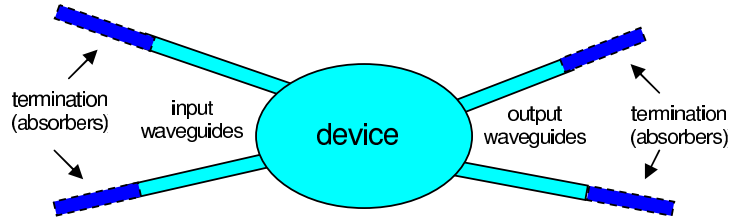

Figure 1-1: Schematic diagram of a photonic device with input and output waveguide channels, which must be truncated in a boundary element method.

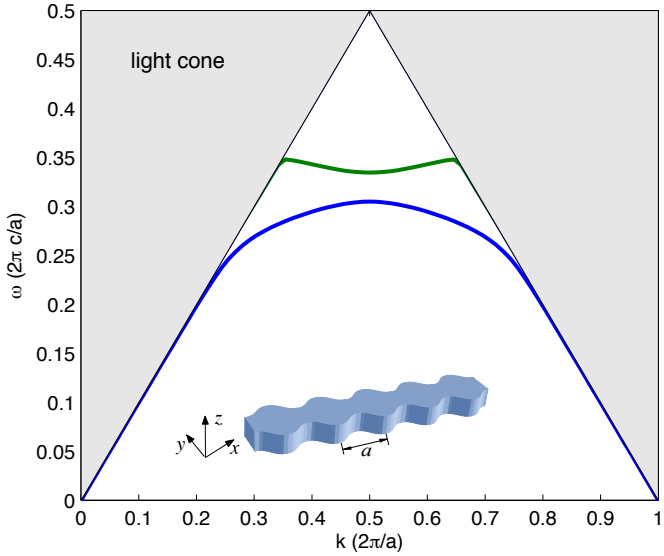

Figure 1-2: The band diagram of a waveguide with period-a sinusoidally corrugated sidewalls (inset), showing the frequencies of the lowest two modes for propagation constants in a period $k \in [0, \frac{2\pi}{a}]$. In between the lowest two modes, there is a "band gap". The period of the waveguide is denoted by a, and c denotes the speed of light in vacuum.

discretization. Moreover, we apply this technique to truncating periodic waveguides in BEM, where in this case we show that the problem becomes much more difficult in the limit of slow-light modes, due to a well-known phenomenon that transition reflections are exacerbated for slow light [6, 24, 25]. More generally, the same technique could be used for low-reflection termination of any periodic medium (photonic crystals [2]), not just waveguides.

Since many nanophotonic devices consist of piecewise homogeneous materials, the boundary element method (BEM) [1, 14–17] is a popular full-wave numerical method for a general photonics solver. Unlike the finite-difference or the finite-element volume-discretization methods, boundary element methods treat infinite homogeneous regions (and some other cases) analytically via Green's functions, and therefore often require no artificial truncation of space. Because BEM only requires surfaces to be discretized, they can be computationally efficient for problems involving piecewise homogeneous media, particularly since the development of fast $O(N\log N)$ solvers [26–29]. However, a truncation difficulty arises with unbounded surfaces of

infinitely extended channels common in photonics. Fig. 1-1 is a general photonic device schematic with input and output waveguide channels. In order to accurately simulate and characterize the device, such as calculating its scattering parameters, formally, the transmission channel must be extended to infinity, requiring infinite computational resources. A more realistic option is to truncate the domain with an absorber that does not generate reflections.

The key challenge is to design an absorber that both has small reflections and is also easily incorporated into a BEM solver. The best-known absorber is a perfectly matched layer (PML) [19–23, 30] as shown in Fig. 1-3. The idea behind the PML is the stretched coordinate in a complex space, so the PML should be a layer with infinitely large interface, which requires the BEM to truncate the interface. More importantly, in order to avoid discretization error, the PML should be a continuously varying anisotropic absorbing medium, whereas boundary element methods are designed for piecewise homogeneous media. A similar problem arises if one were to simply add some absorption within the waveguides—in order to minimize transition reflection, the absorption would need to increase gradually from zero [24], corresponding again to inhomogeneous media. One could also use a volume integral equation (VIE) [31] or a hybrid finite-element method in the inhomogeneous absorbing region, but then one would obtain numerical reflections from the discontinuous change in the discretization scheme from the BEM to the VIE. Moreover, it has been proposed that an integral-equation PML can be obtained by varying the Green's function instead of the media [32], but a continuously varying Green's function greatly complicates panel integrations and makes it difficult to implement a fast solver without the space-invariant property.

In this thesis, we examine an alternative approach to absorbers, adding electrical conductivity to the waveguide *surface* rather than to the volume, via a Dirac delta function conductivity on the absorber surface. The absorber's interior medium remains the same as the waveguide's, thus eliminating the need to discretize the waveguide-absorber interface. This surface-conductivity strategy permits an efficient surface-only discretization, but at the same time allows for a smoothly increasing

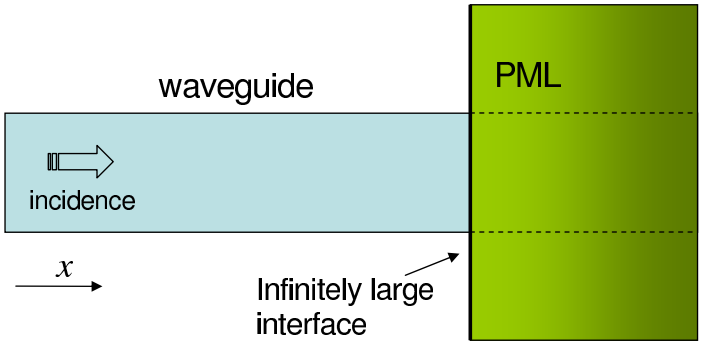

Figure 1-3: A perfectly matched layer for truncating a waveguide chanel in the boundary element method.

surface conductivity, thereby reducing transition reflections. Specifically, surface conductivity is easily implemented in boundary element methods as it corresponds to a jump discontinuity in the field boundary conditions at the absorber surface. Since boundary element methods explicitly discretize the surface boundary, continuously varying the field boundary conditions is easily implemented. Numerical results show that the reflections of the surface absorber can be made negligible by appropriate taper designs.

The reflections of an absorber include a round-trip reflection and a transition reflection. The round-trip reflection is caused by the wave traveling to the end of the absorbing region and reflecting back from the end without being completely absorbed, and it can be reduced by a larger absorption or a longer waveguide. The transition reflection is the immediate reflection at the waveguide-absorber interface due to the transition in medium properties. An adiabatic absorber [24] gradually increases the material absorption to reduce the transition reflection. It has been shown using coupled-mode theory [24] that the transition reflection decreases as a power law with increasing absorber length L, and the smoothness of the conductivity profile determines the power law. Specifically, the transition reflection scales proportional to $L^{-(2d+2)}$, where d is the order of the conductivity function.

Bloch's theorem [2] states that the propagating modes of a periodic waveguide can be written in the form $\mathbf{E}(\mathbf{r}) = e^{-jkx}\mathbf{E}_k(\mathbf{r})$, where x is the wave propagation

direction, k is the propagation constant in the x direction, and $\mathbf{E}_k(\mathbf{r})$ is a periodic function with the physical period a in x. While it may not be obvious that a periodic structure supports guided modes, the periodicity implies a conserved k, which allows true guided modes to be localized below the light cone in the band diagram [2]. As an example, we consider a waveguide with sinusoidally corrugated sidewalls, described in more detail in Sec. 5.2. The dispersion relation of such a "sine waveguide" can be calculated using a planewave method [33], and the two lowest modes for propagation constants $k \in [0, \frac{2\pi}{a}]$ are shown in Fig. 1-2. The frequency range between the two modes represents a band gap in the guided modes [2]. Note that the slope of the band $\frac{d\omega}{dk}$ is the group velocity V_g, the velocity at which energy, information and wavepackets propagate [2]. It is obvious that the group velocity approaches to zero as the frequency approaches the band-gap edge in the diagram. And it has been shown in [24] that the transition reflection increases in a power law as the group velocity decreases. Therefore, absorbers for the periodic waveguide will experience difficulty when the waveguide system is excited at the band-gap edge. This thesis will provide guidance for increasing the length of the absorber to reduce the transition reflections when the group velocity is small.

1.2 Integral Equation Method

The integral equation method is a popular full-wave method to solve Maxwell's equations in frequency domain. Based on discretization schemes, it could be divided into the volume integral equation (VIE) method [31], which discretizes the whole volume of a computational domain, and the surface integral equation (SIE) method, [1,14–17], which only discretizes the interfaces of piecewise homogeneous regions and, in each homogeneous region, analytical solution can be obtained via corresponding Green's functions. For inhomogeneous medium, the volume integration method (VIE) is generally chosen to use by discretizing the whole space domain and parameterizing the inhomogeneous material property, since Green's functions for inhomogeneous medium is usually difficult to obtain. For homogeneous or piecewise-homogeneous medium,

the surface integral equation method is appealing because one could simply use the homogeneous-space Green's function to make a general solver, and the surface-only discretizing scheme turns a 3-D geometry to a 2-D like surface, could significantly save computational costs.

The boundary element method (BEM) is a popular surface integral equation method, and has been developed for decades for simulating a variety of applications. The boundary element method with electric-field integral equation (EFIE) or magnetic-field integral equation (MFIE) formulations could be used to analyze microship antennas [34–36] based on the mixed-potential integration equation (MPIE), which yields a weaker singularity in its integrands than the single potential formulation. The development of the RWG functions defined on triangle panel pairs [1] offers great flexibility with non-uniform discretizations for analyzing objects with arbitrary surfaces, such as arbitrarily shaped microstrip patch antennas [37]. With either Poggio-Miller-Chang-Harrington-Wu (PMCHW) formulation [14, 15] or combined-field integral equation (CFIE) formulations, radiation and scattering problems by 3-D penetrable dielectric bodies could be modeled with the boundary element method [14, 17, 38].

As mentioned above, the boundary element method formulations include the EFIE, MFIE, PMCHW and CFIE [39, 40]. The EFIE and MFIE are typically used to analyze geometries involving perfectly electrical conductor (PEC) or perfectly magnetic conductor(PMC) bodies by enforcing electric field boundary condition (EFIE) or magnetic field boundary condition (MFIE) on the surfaces. However, the EFIE and MFIE could encounter singularities of the integral operators and generate spurious solutions when the analyzed body is exited at its resonating frequencies [14]. Instead, the PMCHW and CFIE formulations could avoid the singularity problem by enforcing both the electric and magnetic field boundary conditions at body surfaces, and are typically used to analyze dielectric bodies.

In this thesis, following the PMCHW formulation, we propose two types of boundary element method formulations for simulating dielectric bodies with electrical surface conductivities. The surface conductivity corresponds to a Dirac delta function on

the surface, and hence it creates a jump for tangential magnetic fields across the surface. We illustrate the two types of formulations using a scattering problem [41–44] of a Mie sphere with electrical surface conductivities. The numerical BEM results of scattered and interior fields of the two formulations are compared with derived analytical solutions. For small surface conductivities, the type II solution is as accurate as the type I solution. For large surface conductivities, the scattered field of type II remains the same accuracy as type I, but the interior field inside the sphere has a larger error and shows a larger coefficient of its power-law convergence with discretizations. The large error occurs because the interior field becomes smaller as the surface conductivity increases. The type II formulation, therefore, has more numerical cancellation errors with two sets of unknown currents. However, since the interior fields are several orders of magnitudes smaller than the scattered fields when the large error occurs, the error could be numerically ignored. We further show that the cancellation error of the type II formulation will not cause numerical problem for analyzing the surface conductive absorber. For waveguide channel, the excitation source is located in the interior region, and power is localized in the waveguide interior. Thus, the interior field is dominant, like the scattered field in the Mie scattering case. Also, the surface conductivity of the absorber remains small when chosen to minimize transition reflections at the waveguide-absorber interface.

The boundary element method becomes more competent for large scale simulations particularly since a few acceleration techniques was developed, like the precorrected-FFT (PFFT) method [26–28, 45–49] and the fast multipole method [29, 50]. These fast methods eliminate the need to fill and store a large full matrix. Instead, they only require storing a sparse matrix, which takes much less storage ($O(N)$) and computational time $O(N\log N)$. The Precorrected-FFT method was first proposed in [26, 45] to solve electrostatic problems, and it has been further developed in [27, 28, 46–49] to solve dynamic electromagnetic problems. In this thesis, to take advantage of periodicity of discretized channel structures, we use a straightforward and easily-implemented FFT-based fast algorithm to accelerate the boundary element method. With this implementation, the solver could nearly achieve $O(N\log N)$ computational requirement.

1.3 Thesis Outline

This thesis is organized as follows. In Chapter 2, we provide background knowledge in order for better understanding the thesis. The background includes the analysis of the reflections of generated by a general absorber for truncating a guided channel; the introduction of the PMCHW formulation, the boundary element method and corresponding integral operators; and the derivation of Mie theory.

In Chapter 3, we describe two types of boundary element method formulations to analyze dielectric bodies with electrical surface conductivities. We illustrate the derivation of the BEM formulations as well as analytical solutions using a scattering problem of a Mie sphere with surface conductivities. Error analysis is performed to compare the two types of of formulations.

In Chapter 4, we present a surface conductive absorber technique for truncating a dielectric waveguide with uniform cross section in the simulation using the boundary element method. Numerical results show that the surface absorber generates several orders of magnitudes smaller reflections than the straightforward volume absorber. The field decay rate due to the surface conductivity is calculated using two methods. The asymptotic attenuation of the transition reflection of the surface absorber with the absorber length is examined.

In Chapter 5, we apply the surface conductive absorber technique to truncate periodic waveguide channels. We demonstrate the performance of the absorber using an example of a waveguide with period-a sinusoidally corrugated sidewalls. We show the difficulty to terminate the periodic waveguide when excited with a small group-velocity mode, and show the relation between the absorber length and group velocity to achieve fixed transition reflection.

Chapter 6 concludes the thesis and describes future work.

In Appendix A, we describe a Gaussian beam generated by a dipole in a complex space, which is used as an excitation throughout the thesis.

Chapter 2

Background

This chapter presents background knowledge for better understanding this thesis. Since this thesis focuses on developing a new surface conductive absorber for terminating waveguide channels with generating minimal reflections, this chapter begins with an introduction of a general absorber, and the round-trip reflection and the transition reflections generated by the absorber. We describe formulations to evaluate the round-trip reflection and the key elements to determine the transition reflection. We briefly describe the PMCHW formulation with the boundary element method, based on which two types of formulations will be presented to incorporate surface conductivities in Chapter 3. In order to benchmark the new formulations, Chapter 3 will also provide an analytical solution of the scattering by a dielectric sphere with surface conductivities, and thus in this chapter, we describe the derivation of Mie theory.

2.1 Absorbers and Reflections

A waveguide channel with a general absorber attached is illustrated in Fig. 2-1. The absorber truncates the waveguide channel by absorbing propagating waves as if the wave propagates along an infinitely long channel without any reflection. The advantage to attach an absorber is that an infinitely long channel can then be numerically analyzed in a finite domain using finite computational resources. An absorber is an artificial part in the whole computational domain to aid the analysis of primary appli-

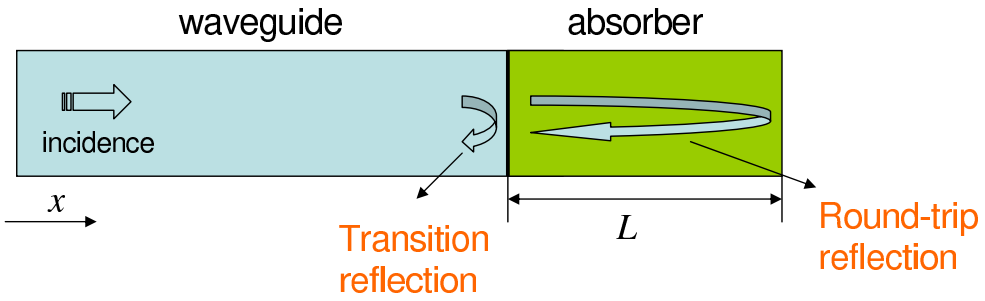

Figure 2-1: Illustration of a waveguide channel truncated by an absorber.

cations with infinitely extended channels, therefore, a good absorber should be small in size, and thus requiring reasonable computational power. And more importantly, it should generate small reflections within the tolerance of applications. In this section, we introduce the reflections generated by an absorber, and generally discuss the relations between the reflections and the property of the absorber including length, absorptivity and absorption profile.

As shown in Fig. 2-1, the reflections generated by an absorber can be divided into a round-trip reflection, R_r, and a transition reflection, R_t. The round-trip reflection is generated by waves entering into the absorber, propagating to the end without being completely absorbed, reflected off the end of the absorber, and eventually propagating back into the waveguide. As shown in Fig. 2-1, the length of the absorber is denoted by L, wave propagates in the $+\hat{x}$ direction, and the waveguide-absorber interface is located at $x = x_0$. The round-trip reflection coefficient is proportional to

$$R_r \sim e^{-4\int_L \alpha(x)dx}, \tag{2.1}$$

where $\alpha(x)$ is the field decay rate due to the absorptivity of the absorber, a factor of 2 in the exponent of (2.1) represents the effect of the round trip, and another factor of 2 indicates that the power is considered.

Consider a dth-order monomial function $s(u)$ defined in $u \in [0, 1]$

$$s(u) = \begin{cases} u^d & 0 \le u \le 1 \\ 0 & \text{else} \end{cases}, \tag{2.2}$$

and a conductivity function of the absorber is defined with $s(u)$

$$\sigma(x) = \sigma_0 s(\frac{x - x_0}{L}), \tag{2.3}$$

where σ_0 is the coefficient of the conductivity function. From the perturbation analysis in Sec. 4.4.1, the decay rate $\alpha(x)$ in (2.1) is proportional to $\frac{\sigma(x)}{V_g}$ in the limit of small σ_0, where V_g is the group velocity of the propagating mode. Therefore, after integrating the exponent in (2.1), the round-trip reflection asymptotically attenuates with

$$R_r \sim e^{-\frac{4L\sigma_0}{(d+1)V_g}}. \tag{2.4}$$

The round-trip reflection exponentially decays with the conductivity coefficient σ_0 and absorber length L, so that it can be reduced by increasing σ_0 or the absorber length. However, large σ_0 will increase the transition reflection, which will be discussed below. In general, the round-trip reflection is fixed with a very small value when discussing the transition reflections, and the conductivity coefficient is therefore made proportional to

$$\sigma_0 \sim \frac{(d+1)V_g}{L}. \tag{2.5}$$

The transition reflection R_t is the reflection generated by the transition in material properties at the waveguide-absorber interface. It can be analyzed using coupled-mode theory [51, 52] in a slowly varying medium along propagation direction. Here we skip the analysis process, and directly provide the conclusion. In the limit of large L, the magnitude of a reflected mode $c_r(L)$ in an asymptotic form is given [24]

$$c_r(L) = s^{(d)}(0^+)\frac{M(0^+)}{\Delta\beta(0^+)}[-jL\Delta\beta]^{-d} + O(L^{-(d+1)}), \tag{2.6}$$

where $\Delta\beta = \beta_i - \beta_r$ is the difference between the propagation constants of the incident and reflected modes, $s^{(d)}(0^+)$ is the dth-order derivative of $s(u)$ evaluated at $u = 0^+$, and M is a coupling coefficient between the incident and reflected modes, depends on the spatial field pattern but is a smooth function of u [24, 52], and $M(0^+)$ is

asymptotically proportional to

$$M(0^+) \sim \frac{\sigma_0}{\Delta\beta}. \tag{2.7}$$

Therefore, the transition reflection is proportional to

$$R_t \sim \left(\sigma_0 \cdot \frac{1}{L^d} \cdot \frac{1}{\Delta\beta^{(d+2)}}\right)^2. \tag{2.8}$$

As we know, the group velocity V_g is proportional to $\Delta\beta$ in the limit of small V_g [24], so $\Delta\beta$ can be replaced with V_g in (2.8).

For a single-mode excitation, the round-trip reflection could be fixed by following (2.5) as $\sigma_0 \sim \frac{V_g}{L}$ for a same-order conductivity profile (same d). Therefore, the transition reflection should be expected to be proportional to

$$R_t \sim \frac{1}{L^{2d+2}} \cdot \frac{1}{V_g^{2d+2}}. \tag{2.9}$$

For a multiple-mode excitation, the group velocity for each mode is generally different, therefore, we are unable to strictly fix the round-trip reflection. Instead, we could conservatively fix the round-trip reflection by picking the initial σ_0 working well for the large V_g mode (achieving small round-trip reflection for the large V_g mode) and making σ_0 inversely proportional to the absorber length as $\sigma_0 \sim \frac{1}{L}$. With this choice of σ_0, the asymptotic form of the transition reflection is

$$R_t \sim \frac{1}{L^{2d+2}} \cdot \frac{1}{V_g^{2d+4}}. \tag{2.10}$$

For the two choices of the conductivity coefficient σ_0, the transition reflection attenuates asymptotically in a power law with the absorber length as $R_t \sim \frac{1}{L^{2d+2}}$. The power-law behavior indicates that, with a higher-order conductivity function, the transition reflection decreases faster with increasing the absorber length. It does not follow that d should be made arbitrarily large, however, there is a tradeoff in which increasing d eventually delays the onset L of the asymptotic regime in which

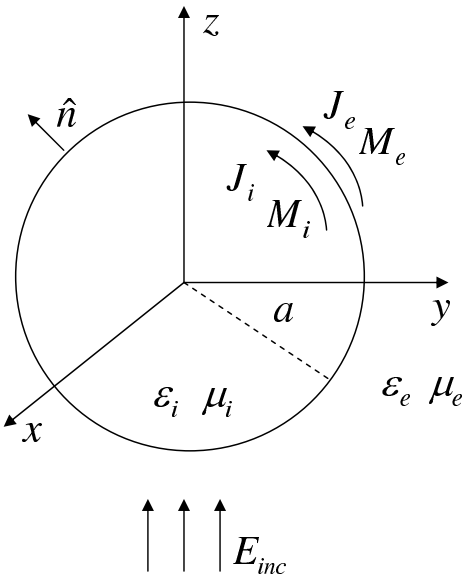

Figure 2-2: An illustration of Mie scattering using the boundary element method.

(2.9) and (2.10) are valid [24]. This will be further discussed in Chapter 5 with numerical results.

2.2 PMCHW formulation and Boundary Element Method

In this section, we briefly describe the PMCHW formulation [14,15] and the boundary element method [1,14–17] by numerically solving a Mie scattering problem, which will be analytically solved via a boundary value problem in Sec. 2.3.

2.2.1 Formulations

Fig. 2-2 shows a dielectric sphere embedded in an exterior medium. The radius of the sphere is denoted by a. The permittivities and permeabilities of the sphere medium and the exterior medium are denoted by ϵ_i, μ_i, and ϵ_e, μ_e, respectively. An x-polarized plane-wave propagating in the z direction shines on the sphere, and thereby generates scattered fields in the exterior region and interior fields in the sphere. The unknowns

of the BEM are equivalent electrical and magnetic currents $\mathbf{J}_e$, $\mathbf{M}_e$ on the exterior side of the sphere surface, and $\mathbf{J}_i$, $\mathbf{M}_i$ lying on the interior side of the surface, with the subscripts e and i denoting the exterior and interior side, respectively.

The scattered fields are treated as if being excited by the currents $\mathbf{J}_e$, $\mathbf{M}_e$ in a homogeneous space of ϵ_e and μ_e (exterior problem), and the interior fields are treated as if being excited by the currents $\mathbf{J}_i$, $\mathbf{M}_i$ in a homogeneous space of ϵ_i and μ_i (interior problem). According to the equivalence principle [53, 54], in order to treat the exterior or interior problem as in a homogeneous space, the following boundary conditions should be satisfied [39]

$$
\begin{aligned}
-\hat{n} \times [\mathbf{E}_{\text{inc}} + \mathbf{E}_s(\mathbf{J}_e, \mathbf{M}_e)] &= \mathbf{M}_e, && (2.11)\\
\hat{n} \times [\mathbf{H}_{\text{inc}} + \mathbf{H}_s(\mathbf{J}_e, \mathbf{M}_e)] &= \mathbf{J}_e, && (2.12)\\
\hat{n} \times \mathbf{E}_i(\mathbf{J}_i, \mathbf{M}_i) &= \mathbf{M}_i, && (2.13)\\
-\hat{n} \times \mathbf{H}_i(\mathbf{J}_i, \mathbf{M}_i) &= \mathbf{J}_i. && (2.14)
\end{aligned}
$$

where $\mathbf{E}_{\text{inc}}$ and $\mathbf{H}_{\text{inc}}$ are the incident electric and magnetic fields, respectively. $\mathbf{E}_s(\cdot)$, $\mathbf{H}_s(\cdot)$ are the integral operators of the electric and magnetic fields evaluated in a homogeneous space whose material property is the same as that of the exterior region, and $\mathbf{E}_i(\cdot)$, $\mathbf{H}_i(\cdot)$ are the integral operators evaluated in a homogeneous space whose material property is the same as that of the interior region. $\hat{n}$ is the normal exterior-pointing unit vector.

The boundary conditions are then enforced to couple the exterior and interior problems. Specifically, the continuity of the tangential components of the electric and magnetic fields on the sphere surface yields the PMCHW formulation

$$
\begin{aligned}
\hat{n} \times [\mathbf{E}_{\text{inc}} + \mathbf{E}_s(\mathbf{J}_e, \mathbf{M}_e)] &= \hat{n} \times \mathbf{E}_i(\mathbf{J}_i, \mathbf{M}_i), && (2.15)\\
\hat{n} \times [\mathbf{H}_{\text{inc}} + \mathbf{H}_s(\mathbf{J}_e, \mathbf{M}_e)] &= \hat{n} \times \mathbf{H}_i(\mathbf{J}_i, \mathbf{M}_i). && (2.16)
\end{aligned}
$$

The field-continuity boundary condition provides two independent equations (2.15)-(2.16) with four unknown currents $\mathbf{J}_e$, $\mathbf{M}_e$, $\mathbf{J}_i$, $\mathbf{M}_i$, leaving two degrees of freedom.

Substituting the field-current relations (2.11)-(2.14) into (2.15) and (2.16) yields the relations between the currents on the exterior and interior sides. It turns out that the current on the two sides have the same magnitude and sign flipped. Therefore, the four sets of unknown currents can be reduced to two sets, $\mathbf{J}$ and $\mathbf{M}$, by

$$\mathbf{J}_e = -\mathbf{J}_i = \mathbf{J}, \tag{2.17}$$

$$\mathbf{M}_e = -\mathbf{M}_i = \mathbf{M}. \tag{2.18}$$

Substituting (2.17), (2.18) into (2.15), (2.16) yields the final version of the PMCHW formulation

$$\hat{n} \times [\mathbf{E}_s(\mathbf{J}, \mathbf{M}) - \mathbf{E}_i(-\mathbf{J}, -\mathbf{M})] = -\hat{n} \times \mathbf{E}_{\text{inc}}, \tag{2.19}$$

$$\hat{n} \times [\mathbf{H}_s(\mathbf{J}, \mathbf{M}) - \mathbf{H}_i(-\mathbf{J}, -\mathbf{M})] = -\hat{n} \times \mathbf{H}_{\text{inc}}. \tag{2.20}$$

The fields can be substituted by the integral operators introduced in the next section, the integral equations can then be discretized to construct a linear matrix system using the Galerkin method [55], and the unknown currents $\mathbf{J}$ and $\mathbf{M}$ can be determined by solving the linear system.

2.2.2 Integral Operators

From Sec. 2.2.1, the two equivalent currents $\mathbf{J}$ and $\mathbf{M}$ on the sphere surface are to be determined by solving the PMCHW formulations (2.19)–(2.20). First of all, the sphere surface is discretized with triangle panels as show in Fig. 2-3, and the currents are approximated with the RWG basis function [1] on triangular-meshed surfaces as shown in Fig. 2-4, and the approximated currents become

$$\mathbf{J} = \sum_m J_m \mathbf{X}_m(\mathbf{r}'), \tag{2.21}$$

$$\mathbf{M} = \sum_m M_m \mathbf{X}_m(\mathbf{r}'), \tag{2.22}$$

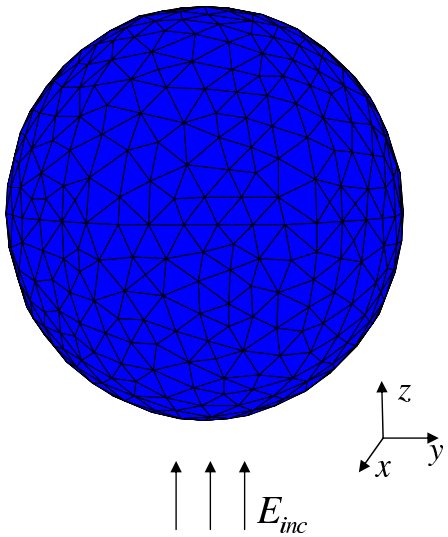

Figure 2-3: A dielectric sphere discretized using triangle panels.

where $\mathbf{X}_m(\mathbf{r}')$ is the RWG function on the mth triangle pair, and J_m, M_m are the corresponding coefficients for the electric and magnetic currents, respectively.

Electric and magnetic fields are represented using the mixed-potential integral equation (MPIE) [16] for a low-order singularity, with integral operators L and K as in [17]

$$\mathbf{E}_l(\mathbf{J},\mathbf{M}) = -Z_l L_l(\mathbf{J}) + K_l(\mathbf{M}), \tag{2.23}$$

$$\mathbf{H}_l(\mathbf{J},\mathbf{M}) = -K_l(\mathbf{J}) - \frac{1}{Z_l} L_l(\mathbf{M}), \tag{2.24}$$

where $Z_l = \sqrt{\mu_l/\epsilon_l}$ is the intrinsic impedance, and the subscript $l = e$ or i denotes the exterior or interior region. The integral operators due to the mth RWG function are given by

$$L_l(\mathbf{r}, \mathbf{X}_m(\mathbf{r}')) = jk_l \mathbf{A}_l(\mathbf{r}, \mathbf{X}_m(\mathbf{r}')) + \frac{j}{k_l} \nabla \Phi_l(\mathbf{r}, \mathbf{X}_m(\mathbf{r}')), \tag{2.25}$$

$$K_l(\mathbf{r}, \mathbf{X}_m(\mathbf{r}')) = -\nabla \times \mathbf{A}_l(\mathbf{r}, \mathbf{X}_m(\mathbf{r}')), \tag{2.26}$$

where $\mathbf{r}$ and $\mathbf{r}'$ are, respectively, the target and source positions and $k_l = \omega\sqrt{\mu_l \epsilon_l}$ is the wavenumber. The vector and scalar potentials $\mathbf{A}$, Φ due to the RWG function

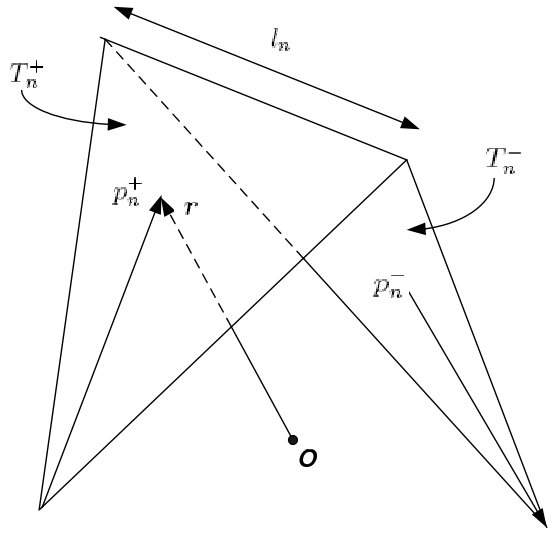

Figure 2-4: The nth RWG basis function [1] on a pair of triangle panels. The two triangle panels are denoted by T_n^+ and T_n^-, respectively. The length of the common edge is denoted by l_n. p_n^+ and p_n^- are the local vectors of the point on each triangle.

$\mathbf{X}_m(\mathbf{r}')$ are

$$\mathbf{A}(\mathbf{r}, \mathbf{X}_m(\mathbf{r}')) = \int_{S'_m} G_l(\mathbf{r}, \mathbf{r}')\mathbf{X}_m(\mathbf{r}')dS', \tag{2.27}$$

$$\Phi(\mathbf{r}, \mathbf{X}_m(\mathbf{r}')) = \int_{S'_m} G_l(\mathbf{r}, \mathbf{r}')\nabla' \cdot \mathbf{X}_m(\mathbf{r}')dS', \tag{2.28}$$

where S'_m is the surface of the mth triangle pair, and $G_l(\mathbf{r}, \mathbf{r}')$ is the Green's function in a homogeneous space whose material property is the same as region l, and it is

$$G_l(\mathbf{r}, \mathbf{r}') = \frac{e^{-jk_l|\mathbf{r}-\mathbf{r}'|}}{4\pi|\mathbf{r}-\mathbf{r}'|}. \tag{2.29}$$

When target points are far away from the source panel, the integral of (2.27) and (2.28) can be numerically calculated using Gauss quadrature [56]. For near-fields, the panel integration can be evaluated using a variety of methods [57–60].

We employ Galerkin method [55] by using the RWG function as the testing function on target triangle pairs. The tested L, K operators on the nth target triangle

pair due to the mth source triangle pair become

$$\mathcal{L}_{l,nm}(\mathbf{X}_m) = \int_{S_n} \mathbf{X}_n(\mathbf{r}) \cdot L_l(\mathbf{X}_m) dS, \tag{2.30}$$

$$\mathcal{K}_{l,nm}(\mathbf{X}_m) = \int_{S_n} \mathbf{X}_n(\mathbf{r}) \cdot K_l(\mathbf{X}_m) dS, \tag{2.31}$$

where S_n is the surface of the nth target triangle pair. Substituting the tested field operators into equations (2.19)-(2.20) yields a matrix with unknown vectors of the RWG coefficients. The linear equation system can be solved either directly or iteratively.

One may notice that in (2.19), the scattered field operator $\mathbf{E}_s(\mathbf{J}, \mathbf{M})$ and the interior field operator $\mathbf{E}_i(-\mathbf{J}, -\mathbf{M})$ take the flipped-direction input currents, but their difference should be equal to $\mathbf{E}_{\text{inc}}$ rather than just a sign flipped. On physical grounds, it is clear that $\mathbf{E}_i$ and $\mathbf{E}_s$ can have very different magnitudes. Consider the case of identical interior and exterior media, so that there will be zero scattered field $\mathbf{E}_s$ and the interior field $\mathbf{E}_i$ will be the same as the incident field. However, it may not be immediately obvious how such different field magnitudes can arise in this formulation, especially for identical media, given that $\mathbf{E}_s(\mathbf{J}, \mathbf{M})$ and $\mathbf{E}_i(-\mathbf{J}, -\mathbf{M})$ are generated by equal and opposite currents. (Note, however, that $\mathbf{E}_i$ is not a merely a mirror flip of $\mathbf{E}_s$ even for identical media: due to the pseudovector nature of magnetic fields and currents [61], a mirror flip across the interface would correspond to $+\mathbf{J}$, $-\mathbf{M}$ currents, or vice versa for an antimirror flip. So, flipping the sign of *both* currents changes $\mathbf{E}$ in a nonsymmetrical manner.)

Here, we briefly explain how this phenomenon arises in terms of the nature of the integral operators. In particular, this phenomenon is determined by the gradient and curl operators in the integral operators L and K in (2.25)-(2.26) for the self term (target and source triangles overlap, $m = n$ in (2.30)–(2.31)) of the system matrix.

Consider a source triangle panel S' lies on the xy plane where $z = 0$, as shown in Fig. 2-5. Two observation lines l_1 and l_2 are perpendicular to the triangle panel, and line l_1 intersects with the panel but l_2 doesn't. The x and y components of the vector potential $\mathbf{A}$ and scalar potential Φ along line l_1 due to the currents and charges (represented by RWG functions) on the source triangle panel is shown in Fig. 2-6.

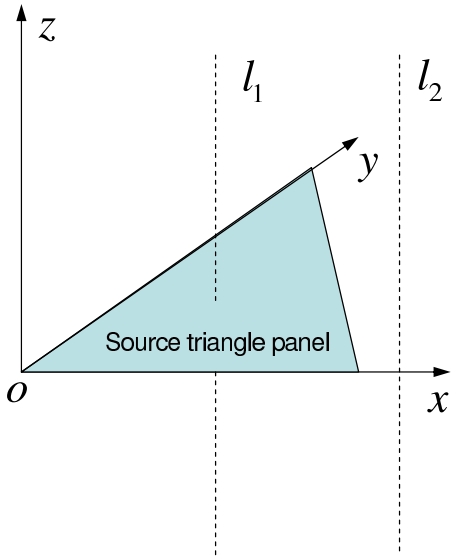

Figure 2-5: A triangle panel lying on the xy plane. Observation lines l_1 and l_2 are parallel to the z axis with l_1 penetrating the panel and l_2 far away from the panel.

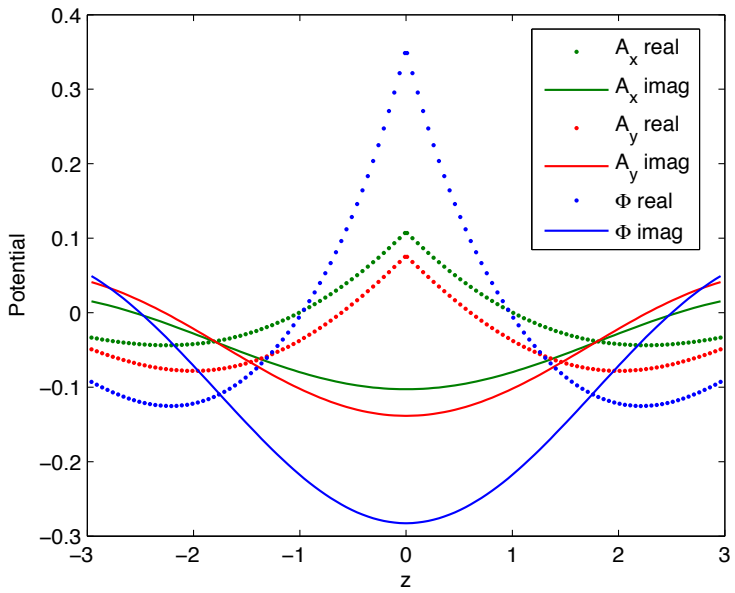

Figure 2-6: Components of the vector potential A and scalar potential Φ along line l_1 penetrating the source triangle panel in Fig. 2-5.

The potentials are symmetric with $z = 0$, and the real parts of the potentials $\mathbf{A}$ and Φ are non-differentiable with respect to z at $z = 0$. Therefore, the real part of $\frac{\partial \mathbf{A}}{\partial z}$ and $\frac{\partial \Phi}{\partial z}$ has a sign difference for $z = 0^+$ and $z = 0^-$. This is shown in Fig. 2-7 that

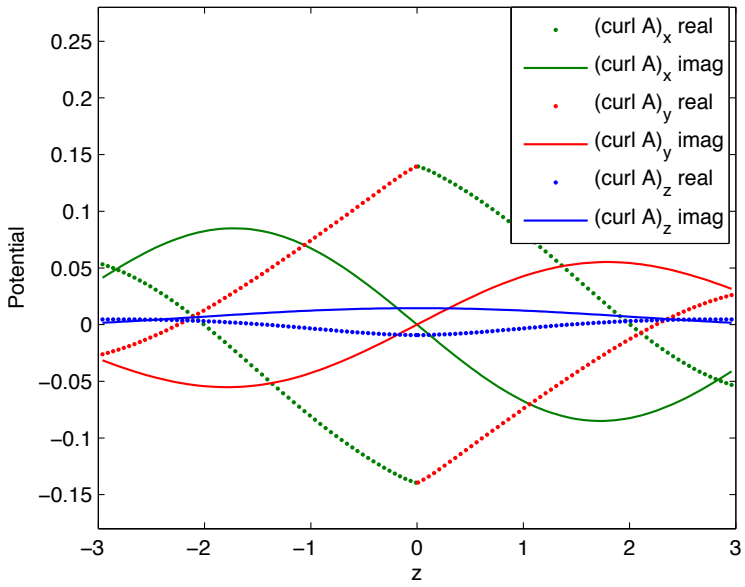

(a) $\nabla \times A$

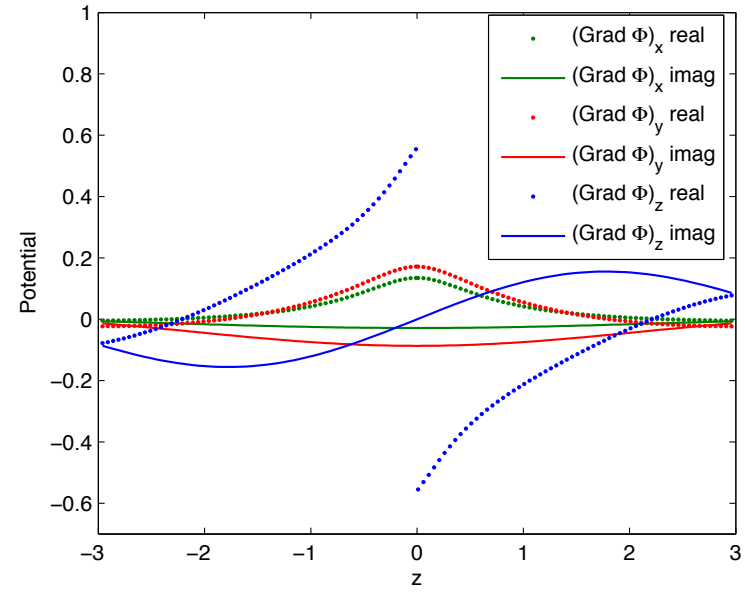

(b) $\nabla\Phi$

Figure 2-7: Components of $\nabla \times A$ and $\nabla\Phi$ along along line l_1 penetrating the source triangle panel in Fig. 2-5.

the real parts of the x and y components of $\nabla \times A$ and the z components of $\nabla\Phi$ are discontinuous and flip signs across $z = 0$. This jump at $z = 0$ is responsible for the

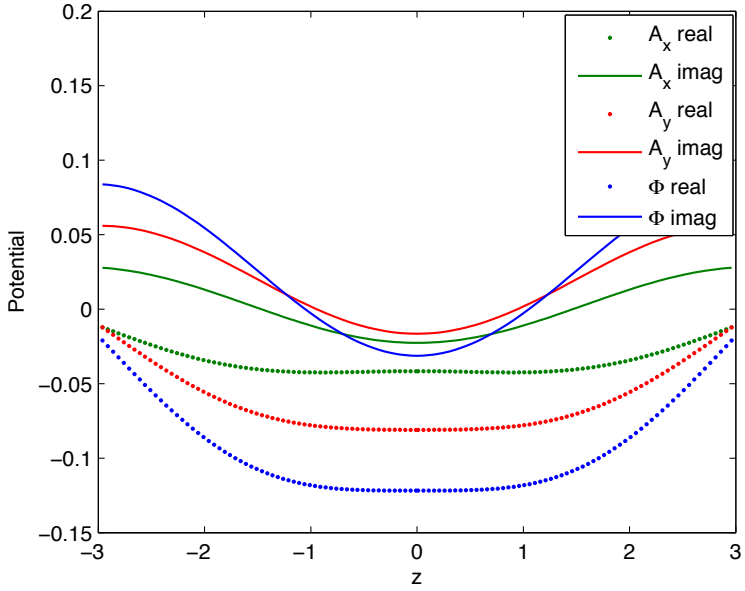

Figure 2-8: Components of the vector potential A and scalar potential Φ along a line l_2 away from the source triangle panel in Fig. 2-5.

difference of L and K in (2.25) and (2.26) in the self term at the exterior and interior sides of the surface. The imaginary part of the self-term potentials corresponds to a sinc function, so the derivative with respect to z is the same for both the exterior and interior sides.

Figure 2-8 shows the potentials along line l_2 which is away from the source triangle panels. The potentials are symmetric with $z = 0$ and are differentiable at $z = 0$. Therefore, $\frac{\partial \mathbf{A}}{\partial z}$ and $\frac{\partial \Phi}{\partial z}$ are equal to zeros at $z = 0$, the same for both exterior and interior sides of the surface. Fig. 2-9 shows all the components of $\nabla \times A$ and $\nabla\Phi$ along l_2 and they are continuous at $z = 0$. Therefore, the difference of $\mathbf{E}_s(\mathbf{J}, \mathbf{M})$ and $\mathbf{E}_i(-\mathbf{J}, -\mathbf{M})$ comes from the real parts of the L and K operators in the self term.

2.3 Mie Theory

The Mie theory [41–44, 53] provides an analytical solution of scattered field by a dielectric sphere shown in Fig. 2-10. The sphere is illuminated by an incident x-polarized plane wave, propagating in the z direction.

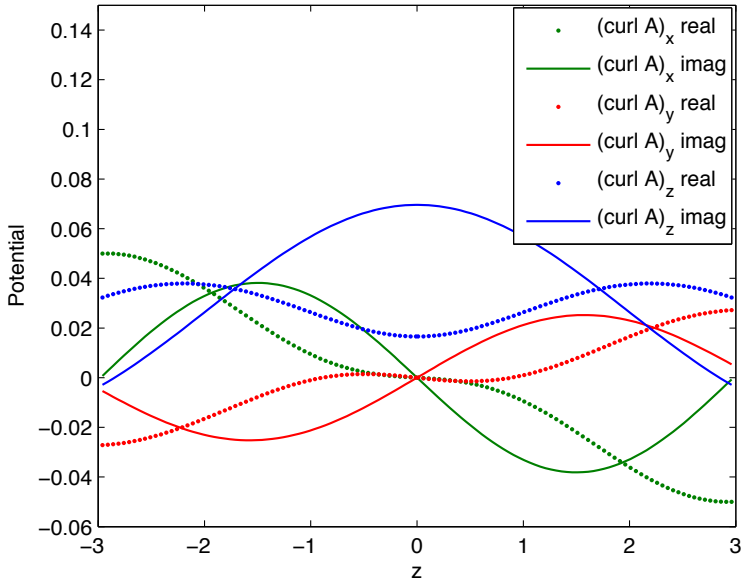

(a) $\nabla \times A$

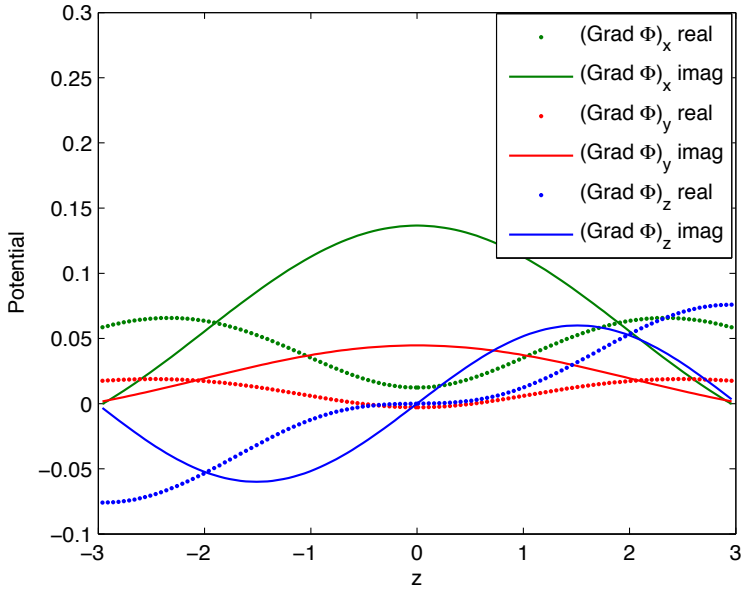

(b) $\nabla\Phi$

Figure 2-9: Components of $\nabla \times A$ and $\nabla\Phi$ along line l_2 away from the source triangle panel in Fig. 2-5.

In this section, we briefly derive the analytical solution in accordance with [43]. The derivation is basically solving a boundary value problem with governing Maxwell's

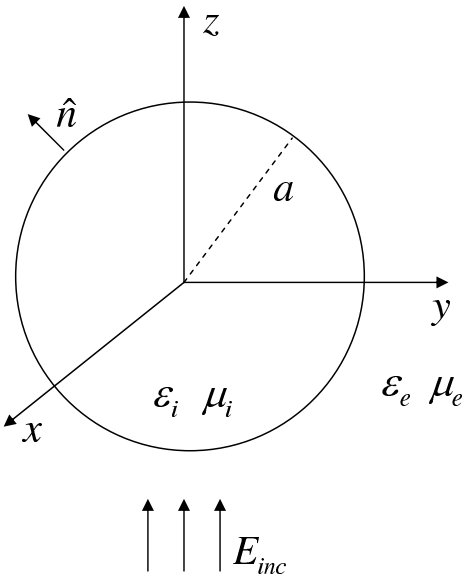

Figure 2-10: The scattering of a Mie sphere.

equations. First of all, The incident field, the scattered field and the interior field in the sphere are expanded in terms of vector harmonics **M** and **N** with unknown coefficients. The cooefficients are then obtained by matching boundary conditions on the surface of the sphere.

According to [43], the vector harmonics **M** and **N** both satisfy Helmholtz equations as

$$\nabla^2\mathbf{M} + k^2\mathbf{M} = 0 \tag{2.32}$$

$$\nabla^2\mathbf{N} + k^2\mathbf{N} = 0, \tag{2.33}$$

where k is the wavenumber. The two vectors are coupled in the way of

$$\mathbf{N} = \frac{\nabla \times \mathbf{M}}{k}, \tag{2.34}$$

and can be obtained through solving a scalar wave equation in spherical coordinates with spherical harmonics [43]. The solutions are denoted by $\mathbf{M}_{emn}$, $\mathbf{M}_{omn}$, $\mathbf{N}_{emn}$, and $\mathbf{N}_{omn}$, where subscripts e and o indicate even and odd modes in terms of φ, respectively; m and n are non-negative integers and satisfy $n \geq m$. The four vector

harmonics are

$$\mathbf{M}_{emn} = \frac{-m}{\sin\theta}\sin m\varphi P_n^m(\cos\theta) z_n(\rho)\hat{\theta} - \cos m\varphi \frac{dP_n^m(\cos\theta)}{d\theta} z_n(\rho)\hat{\varphi}, \tag{2.35}$$

$$\mathbf{M}_{omn} = \frac{m}{\sin\theta}\cos m\varphi P_n^m(\cos\theta) z_n(\rho)\hat{\theta} - \sin m\varphi \frac{dP_n^m(\cos\theta)}{d\theta} z_n(\rho)\hat{\varphi}, \tag{2.36}$$

$$\begin{aligned}\mathbf{N}_{emn} = &\frac{z_n(\rho)}{\rho}\cos m\varphi\, n(n+1) P_n^m(\cos\theta)\hat{r} \\ &+ \cos m\varphi \frac{dP_n^m(\cos\theta)}{d\theta}\frac{1}{\rho}\frac{d}{d\rho}[\rho z_n(\rho)]\hat{\theta} \\ &- m\sin m\varphi \frac{P_n^m(\cos\theta)}{\sin\theta}\frac{1}{\rho}\frac{d}{d\rho}[\rho z_n(\rho)]\hat{\varphi},\end{aligned} \tag{2.37}$$

$$\begin{aligned}\mathbf{N}_{omn} = &\frac{z_n(\rho)}{\rho}\sin m\varphi\, n(n+1) P_n^m(\cos\theta)\hat{r} \\ &+ \sin m\varphi \frac{dP_n^m(\cos\theta)}{d\theta}\frac{1}{\rho}\frac{d}{d\rho}[\rho z_n(\rho)]\hat{\theta} \\ &+ m\cos m\varphi \frac{P_n^m(\cos\theta)}{\sin\theta}\frac{1}{\rho}\frac{d}{d\rho}[\rho z_n(\rho)]\hat{\varphi},\end{aligned} \tag{2.38}$$

where $\rho = kr$, and $P_n^m(\cdot)$ is the associated Legendre function of the first kind of degree n and order m, as defined

$$P_m^n(x) = (1-x^2)^{m/2}\frac{d^m P_n(x)}{dx^m}. \tag{2.39}$$

One may notice that this definition of $P_n^m(\cdot)$ may differ from some other literatures with a factor of $(-1)^m$, commonly known as the Condon-Shortley phase [62]. $z_n(\rho)$ is the spherical Bessel function, and it can be the first kind, the second kind and the third kind (spherical Hankel function), denoted as $j_n(\rho)$, $y_n(\rho)$, and $h_n(\rho)$, respectively. The spherical Hankel function is the linear combinations of the first two kinds as

$$h_n^{(1)}(\rho) = j_n(\rho) + jy_n(\rho), \tag{2.40}$$

$$h_n^{(2)}(\rho) = j_n(\rho) - jy_n(\rho). \tag{2.41}$$

The vector harmonics $\mathbf{M}_{emn}$, $\mathbf{M}_{omn}$, $\mathbf{N}_{emn}$, and $\mathbf{N}_{omn}$ are mutually orthogonal to each other [43], and can form a basis for expanding the electric and magnetic fields.

The incident fields are expanded with the vector harmonics. Unlike the convention

used in [43], we use the conventional time harmonic term $e^{j\omega t}$. The electric and magnetic fields of the incident wave are

$$\mathbf{E}_{\text{inc}} = E_0 e^{-jk_e z}\hat{x} = E_0 e^{-jk_e r\cos\theta}\hat{x}, \tag{2.42}$$

$$\mathbf{H}_{\text{inc}} = \frac{k_e}{\omega\mu} E_0 e^{-jk_e z}\hat{y} = \frac{k_e}{\omega\mu} E_0 e^{-jk_e r\cos\theta}\hat{y}, \tag{2.43}$$

where $k_e = \omega\sqrt{\mu_e\epsilon_e}$ is the wavenumber of the exterior medium. By orthogonality, the coefficients of the vector harmonic expansions of the incident fields can be obtained, and the expansions are

$$\mathbf{E}_{\text{inc}} = E_0 \sum_{n=1}^{\infty}(-j)^n \frac{2n+1}{n(n+1)}(\mathbf{M}_{o1n}^{(1)} + j\mathbf{N}_{e1n}^{(1)}), \tag{2.44}$$

$$\mathbf{H}_{\text{inc}} = -\frac{k_e}{\omega\mu_e} E_0 \sum_{n=1}^{\infty}(-j)^n \frac{2n+1}{n(n+1)}(\mathbf{M}_{e1n}^{(1)} - j\mathbf{N}_{o1n}^{(1)}), \tag{2.45}$$

where the superscript (1) indicates using the first-kind spherical Bessel function $j_n(\rho)$ in the vector harmonics, because of the finite incident fields at the origin. Note that all terms with $m \neq 1$ vanished.

The scattered electric and magnetic fields are denoted by $\mathbf{E}_s$, $\mathbf{H}_s$ and the interior fields in the sphere are denoted by $\mathbf{E}_i$, $\mathbf{H}_i$. In order to obtain the expansions of the scattered and interior fields, the boundary conditions, that the total tangential fields are continuous across the sphere surface, are enforced

$$\hat{n} \times (\mathbf{E}_{\text{inc}} + \mathbf{E}_s) = \hat{n} \times \mathbf{E}_i, \qquad \text{at} \quad r = a, \tag{2.46}$$

$$\hat{n} \times (\mathbf{H}_{\text{inc}} + \mathbf{H}_s) = \hat{n} \times \mathbf{H}_i, \qquad \text{at} \quad r = a \tag{2.47}$$

where $\hat{n}$ is an exterior-pointed normal unit vector. The continuity boundary conditions and the orthogonality of vector harmonics determine that the scattered and interior fields can be expanded with the same set of vector harmonics as the incident

fields. Therefore, the expansions of the interior fields are

$$\mathbf{E}_i = \sum_{n=1}^{\infty} E_n(c_n\mathbf{M}_{o1n}^{(1)} + jd_n\mathbf{N}_{e1n}^{(1)}), \tag{2.48}$$

$$\mathbf{H}_i = -\frac{k_i}{\omega\mu_i}\sum_{n=1}^{\infty} E_n(d_n\mathbf{M}_{e1n}^{(1)} - jc_n\mathbf{N}_{o1n}^{(1)}), \tag{2.49}$$

where c_n, d_n are the unknown coefficients, $E_n = (-j)^n E_0\frac{2n+1}{n(n+1)}$, μ_i is the permeability of the interior medium, and k_i is the wavenumber in the sphere region. Note that E_n attenuates at a power-law $O(\frac{1}{n})$ with n. Similarly, the expansions of the scattered fields are

$$\mathbf{E}_s = \sum_{n=1}^{\infty} E_n(-ja_n\mathbf{N}_{e1n}^{(3)} - b_n\mathbf{M}_{o1n}^{(3)}), \tag{2.50}$$

$$\mathbf{H}_s = \frac{k_e}{\omega\mu_e}\sum_{n=1}^{\infty} E_n(-jb_n\mathbf{N}_{o1n}^{(3)} + a_n\mathbf{M}_{e1n}^{(3)}), \tag{2.51}$$

where a_n, b_n are the other two sets of the unknown coefficients. The superscript (3) indicates using the third-kind spherical Bessel function $h^{(2)}(\rho)$ in the vector harmonics for outgoing spherical waves to satisfy the boundary condition at the infinity.

The field expansions (2.44), (2.45), (2.48)-(2.51) are then substituted into the boundary conditions (2.46) and (2.47). Specifically, enforcing the continuity of the θ and φ components of the electric and magnetic fields at the spherical surface $r = a$, yields four linearly independent equations, and they are

$$b_n h_n^{(2)}(u) + c_n j_n(v) = j_n(u), \tag{2.52}$$

$$a_n\frac{k_i}{k_e}[u\, h_n^{(2)}(u)]' + d_n[v\, j_n(v)]' = \frac{k_i}{k_e}[u\, j_n(u)]', \tag{2.53}$$

$$a_n\mu_i h_n^{(2)}(u) + d_n\frac{k_i}{k_e}\mu_e j_n(v) = \mu_i j_n(u), \tag{2.54}$$

$$b_n\mu_i[u\, h_n^{(2)}(u)]' + c_n\mu_e[v\, j_n(v)]' = \mu_i[u\, j_n(u)]', \tag{2.55}$$

where

$$u = k_e a, \qquad v = k_i a. \tag{2.56}$$

The derivative of $\rho z_n(\rho)$, where $z_n(\cdot)$ is a spherical Bessel function $j_n(\cdot)$ or $h_n^{(2)}(\cdot)$, can be calculated using an identity

$$[\rho z_n(\rho)]' = \rho z_{n-1}(\rho) - n z_n(\rho). \tag{2.57}$$

Solving the four equations (2.52)-(2.55) yields the coefficients in closed form

$$a_n = \frac{(k_i/k_e)^2 j_n(v)[u\, j_n(u)]' - j_n(u)[v\, j_n(v)]'}{(k_i/k_e)^2 j_n(v)[u\, h_n^{(2)}(u)]' - h_n^{(2)}(u)[v\, j_n(v)]'}, \tag{2.58}$$

$$b_n = \frac{j_n(v)[u\, j_n(u)]' - j_n(u)[v\, j_n(v)]'}{j_n(v)[u\, h_n^{(2)}(u)]' - h_n^{(2)}(u)[v\, j_n(v)]'}, \tag{2.59}$$

$$c_n = \frac{j_n(u)[u\, h_n^{(2)}(u)]' - h_n^{(2)}(u)[u\, j_n(u)]'}{j_n(v)[u\, h_n^{(2)}(u)]' - h_n^{(2)}(u)[v\, j_n(v)]'}, \tag{2.60}$$

$$d_n = \frac{(k_i/k_e) j_n(u)[u\, h_n^{(2)}(u)]' - (k_i/k_e) h_n^{(2)}(u)[u\, j_n(u)]'}{(k_i/k_e)^2 j_n(v)[u\, h_n^{(2)}(u)]' - h_n^{(2)}(u)[v\, j_n(v)]'}. \tag{2.61}$$

In general, for a Mie scattering problem, the exterior and interior material are different, and the coefficients (2.58)-(2.61) attenuate exponentially with n. Fig. 2-11(a) shows the four coefficients attenuating with n in a semilog plot for an example of a large medium contrast with $k_i/k_e = 4$. The attenuation of c_n, d_n are slower than a_n, b_n, but the 20th terms of c_n, d_n are already smaller than 10^{-10}, where the truncation of the series can be made numerically.

However, the exponential attenuation rates of the coefficients c_n, d_n decrease with the medium contrast. Given an identical exterior and interior material, the curves of c_n and d_n with n are flat, equal to $1'$s, and coefficients a_n, b_n vanished, as shown in Fig. 2-11(b). This is as expected, because the space is homogeneous when the the exterior and and interior materials are identical, therefore, the scattered field vanishes, and the interior field is equal to the incident field. As a result, in this same-medium case, the expansions in (2.48) and (2.49) converge at a first-order power-law $O(\frac{1}{n})$,

due to the attenuation of the coefficient E_n.

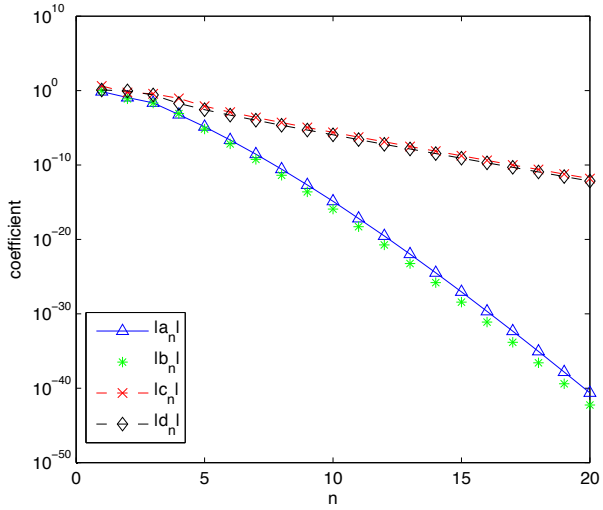

(a) Medium contrast=4. Relative permittivities of the exterior and interior medium are 1 and 16, respectively.

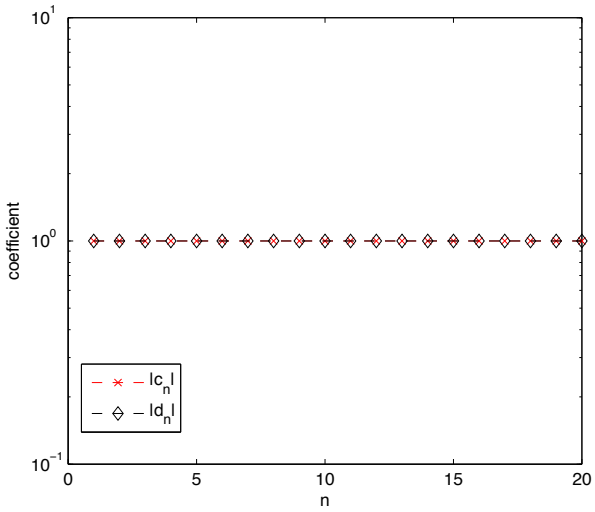

(b) Identical exterior and interior medium.Relative permittivity is 16.

Figure 2-11: The attenuation of the coefficients (2.58)-(2.61) with n of the Mie theory. The radius of the sphere is $1\lambda_i$, where λ_i is the wavelength in the interior medium.

Chapter 3

BEM Formulations for Surface Conductivities

This thesis will present a surface conductive absorber with the boundary element method (BEM) for truncating infinitely extended dielectric channels in Chapter 4 and Chapter 5. The absorber requires the BEM formulation to incorporate the varying surface conductivities. In this chapter, we propose two types of BEM formulations (type I and type II). We illustrate the formulations using the scattering of a dielectric sphere with surface conductivities, and benchmark the BEM results with analytical solutions. Our comparison shows that even though the type II formulation uses fewer unknowns, it is as accurate as the type I formulation for calculating exterior scattered fields for a whole range of surface conductivities. The type II formulation shows a large coefficient in a power-law convergence when calculating interior fields with large surface conductivities, for which the interior fields are several orders of magnitude smaller than the scattered field and thus are numerically negligible. To model the surface absorber, we will demonstrate in Chapter 4 that the type II formulation provides the same accuracy as type I, as power is localized and the interior fields of the dielectric waveguide dominate.

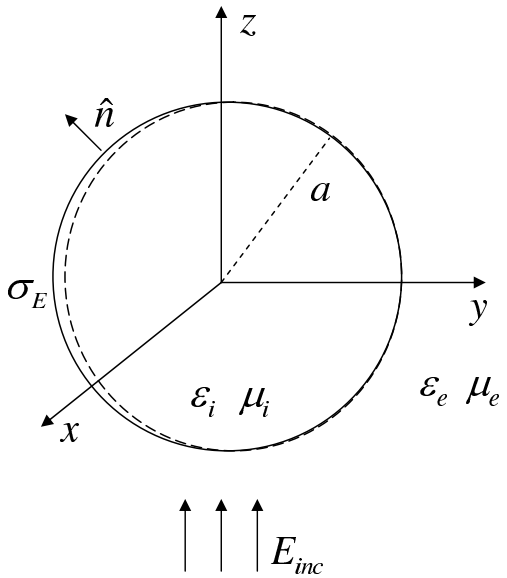

Figure 3-1: The scattering of a Mie sphere with electrical surface conductivity σ_E.

3.1 Analytical Solutions of the Scattering by a Sphere with Surface Conductivities

Mie theory [41–44, 53] provides an analytical solution for the scattered and interior fields by a Mie sphere that is illuminated by an incident x-polarized z-propagating plane wave. Its derivation has been shown in Sec. 2.3. The Mie sphere is in general either a dielectric sphere or a PEC sphere. However, in this chapter, we analyze the scattering by a dielectric sphere with a sheet of electrical surface conductivity. The electrical surface conductivity is denoted by $\sigma_E\delta(r-a)$, where $\delta(r-a)$ is a Dirac delta function on the sphere surface, and a is the radius of the sphere. Therefore, it is worth including a brief analytical derivation of the scattering by this sphere with surface conductivity, as shown in Fig. 3-1.

The derivation is solving a boundary value problem governed by Maxwell's equations. The incident field, the scattered field and the interior field in the sphere are expanded in terms of vector harmonics $\mathbf{M}$ and $\mathbf{N}$ (see Sec. 2.3) with unknown coefficients. The coefficients are then determined by enforcing boundary conditions on the surface of the sphere. The time-harmonic convention $e^{j\omega t}$ is adopted.

For the electric field boundary condition, the electrical surface conductivity does not affect the continuity of tangential electric field on the sphere surface, therefore, the boundary condition is

$$\hat{n} \times (\mathbf{E}_{\text{inc}} + \mathbf{E}_s) = \hat{n} \times \mathbf{E}_i, \qquad \text{at} \quad r = a. \tag{3.1}$$

where $\hat{n}$ is the exterior-pointed normal unit vector.

Due to the electrical surface conductivity, an electrical current $\mathbf{J}_{\text{ind}} = \sigma_E \mathbf{E}_{\tan}$ is induced on the sphere surface, and therefore, the continuity boundary condition of the magnetic field in (2.47) is no longer valid. Instead, the tangential magnetic field has a jump across the sphere surface as

$$\hat{n} \times (\mathbf{H}_{\text{inc}} + \mathbf{H}_s - \mathbf{H}_i) = \sigma_E \mathbf{E}_{\tan}, \qquad \text{at} \quad r = a, \tag{3.2}$$

where $\mathbf{E}_{\tan} = -\hat{n} \times \hat{n} \times \mathbf{E}$ is the tangential electric field on the sphere surface. The tangential electric field on the surface can be the tangential components of either $\mathbf{E}_i$ or $(\mathbf{E}_{\text{inc}} + \mathbf{E}_s)$ according to the continuity in (3.1). For simplicity, we use $\mathbf{E}_i$ later in this section.

As the same in section 2.3, the incident fields are expanded with the vector harmonics in the same way as in (2.44) and (2.45). With the same electric field boundary condition (3.1) and the modified magnetic field boundary condition (3.2), the scattered field and the interior field can be expanded with the same sets of vector harmonics in the same manner as in (2.48)-(2.51). Substituting these expansions into the boundary conditions (3.1) and (3.2) yields another four linearly independent equations with unknown coefficients a_n, b_n, c_n, d_n

$$b_n h_n^{(2)}(u) + c_n j_n(v) = j_n(u), \tag{3.3}$$

$$a_n K[u\, h_n^{(2)}(u)]' + d_n[v\, j_n(v)]' = K[u\, j_n(u)]', \tag{3.4}$$

$$a_n \mu_i h_n^{(2)}(u) + d_n K \mu_e j_n(v) - j\, d_n W_1[v j_n(v)]' = \mu_i j_n(u), \tag{3.5}$$

$$b_n \mu_i[u\, h_n^{(2)}(u)]' + c_n \mu_e[v\, j_n(v)]' + j c_n W_2 j_n(v) = \mu_i[u\, j_n(u)]', \tag{3.6}$$

where

$$K = k_i/k_e, \tag{3.7}$$

$$W_1 = \frac{\sigma_E \omega \mu_e \mu_i}{k_e k_i a}, \qquad W_2 = \sigma_E \omega \mu_e \mu_i a, \tag{3.8}$$

$$u = k_e a, \qquad v = k_i a, \tag{3.9}$$

in which k_i and k_e are the wavenumbers of the interior and exterior regions, respectively; μ_i and μ_e are the permeabilities of the interior and exterior regions, respectively; and ω is the angular frequency.

Solving the above four equations (3.3)-(3.6) yields the coefficients in close form

$$a_n = \frac{K^2 \mu_e j_n(v)[u\, j_n(u)]' - \mu_i j_n(u)[v\, j_n(v)]' - jKW_1[u\, j_n(u)]'[v\, j_n(v)]'}{K^2 \mu_e j_n(v)[u\, h_n^{(2)}(u)]' - \mu_i h_n^{(2)}(u)[v\, j_n(v)]' - jKW_1[u\, h_n^{(2)}(u)]'[v\, j_n(v)]'}, \tag{3.10}$$

$$b_n = \frac{\mu_e j_n(u)[v\, j_n(v)]' - \mu_i j_n(v)[u\, j_n(u)]' + jW_2 j_n(u) j_n(v)}{\mu_e h_n^{(2)}(u)[v\, j_n(v)]' - \mu_i j_n(v)[u\, h_n^{(2)}(u)]' + jW_2 h_n^{(2)}(u) j_n(v)}, \tag{3.11}$$

$$c_n = \frac{\mu_i h_n^{(2)}(u)[u\, j_n(u)]' - \mu_i j_n(u)[u\, h_n^{(2)}(u)]'}{\mu_e h_n^{(2)}(u)[v\, j_n(v)]' - \mu_i j_n(v)[u\, h_n^{(2)}(u)]' + jW_2 h_n^{(2)}(u) j_n(v)}, \tag{3.12}$$

$$d_n = \frac{\mu_i K j_n(u)[u\, h_n^{(2)}(u)]' - \mu_i K h_n^{(2)}(u)[u\, j_n(u)]'}{\mu_e K^2 j_n(v)[u\, h_n^{(2)}(u)]' - \mu_i h_n^{(2)}(u)[v\, j_n(v)]' - jKW_1[u\, h_n^{(2)}(u)]'[v\, j_n(v)]'}. \tag{3.13}$$

With these coefficients, the analytical solutions of the scattered and interior fields can be calculated with the expansions (2.48)-(2.51).

Similarly as discussed in section 2.3, the coefficients (3.10)-(3.13) attenuate exponentially fast with n for a geometry of different exterior and interior media. Fig. 3-2(a) shows the exponential attenuations of the coefficients for a geometry with medium contrast $k_i/k_e = 4$. As the difference of the two media decreases, the attenuation of the coefficients c_n and d_n becomes slower while a_n and b_n remain the same attenuation rate. Fig. 3-2(b) shows the coefficients of a geometry of identical exterior and

interior media. The curves of the coefficients c_n and d_n are close to flat with the magnitudes being several orders of magnitude smaller than 1, while the coefficients a_n, b_n attenuate exponentially fast. This implies that, for this identical-media case, the interior field converges at a power law thanks to the attenuation of the coefficient E_n, while the scattered field can still converge exponentially fast.

3.2 Boundary Element Method Formulations with Surface Conductivities

In this section, we numerically solve the scattering by a dielectric sphere with electrical surface conductivity using the boundary element method (BEM), as opposed to the analytical solution in Sec. 3.1. A dielectric sphere with an electrical surface conductivity is embedded in an exterior medium, as shown in Fig. 3-3. The surface conductivity is a Dirac delta function across the sphere surface, denoted as $\sigma_E \delta(r-a)$, where a is the radius of the sphere and σ_E is the magnitude of the surface conductivity, with the subscript E indicating that the electrical surface conductivity is considered. The permittivities and permeabilities of the sphere medium and the exterior medium are ϵ_i, μ_i, and ϵ_e, μ_e, respectively. An x-polarized plane-wave propagating in z direction shines on the sphere, and thereby generates scattered fields in the exterior region and fields in the interior. In the following sections, we describe two types of BEM formulations.

3.2.1 Formulation Type I based on Equivalence Principle

The type I formulation is derived based on the equivalence principle [53]. The unknowns are equivalent electrical and magnetic currents lying on the sphere surface, specifically, $\mathbf{J}_e$ and $\mathbf{M}_e$ on the exterior side; and $\mathbf{J}_i$ and $\mathbf{M}_i$ on the interior side. The scattered electric and magnetic fields $\mathbf{E}_s$ and $\mathbf{H}_s$ are treated equivalently as if being excited by the currents $\mathbf{J}_e$ and $\mathbf{M}_e$ in a homogeneous space whose material property is equal to that of the exterior region (denoted as an exterior problem). Similarly,

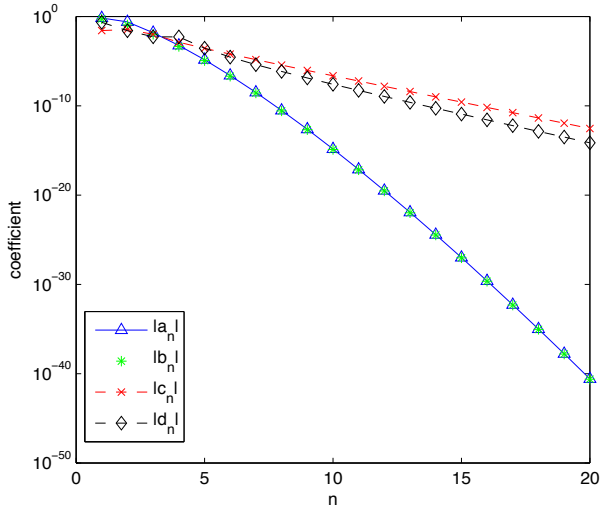

(a) Medium contrast=4. Relative permittivities of the exterior and interior medium are 16 and 1, respectively.

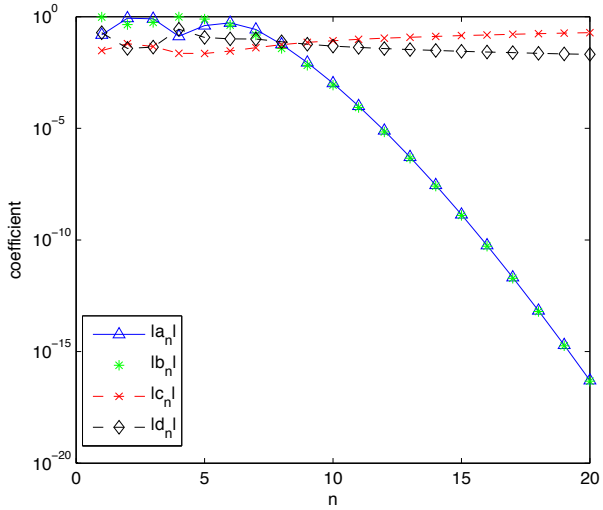

(b) Identical exterior and interior medium. Relative permittivity is 16.

Figure 3-2: The convergence of the coefficients (3.10)-(3.13) of the Mie scattering with surface conductivity $\sigma_E = 0.01\text{S/m}$. The radius of the sphere is $1\lambda_i$.

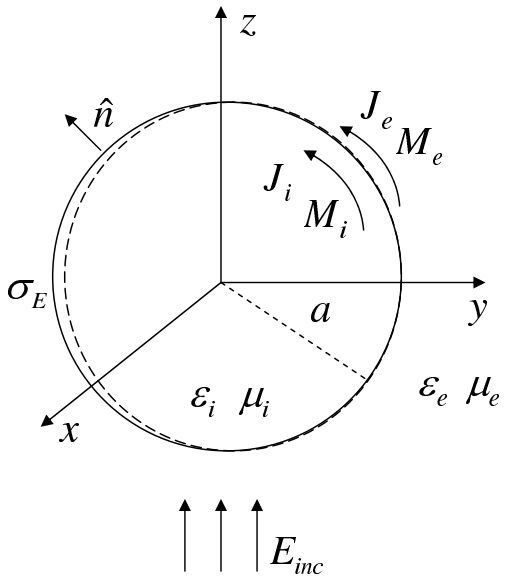

Figure 3-3: An illustration of Mie scattering with electrical surface conductivity σ_E using the boundary element method.

the interior electric and magnetic fields $\mathbf{E}_i$ and $\mathbf{H}_i$ are treated as if being excited by the currents $\mathbf{J}_i$ and $\mathbf{M}_i$ in a homogeneous space whose material property is the same as that of the interior region (denoted as an interior problem). According to the equivalence principle [53], in order to treat the exterior or interior problem as in a homogeneous space, the boundary conditions in (2.11)-(2.14) should be satisfied [39], and we rewrite them here

$$-\hat{n} \times [\mathbf{E}_{\text{inc}} + \mathbf{E}_s(\mathbf{J}_e, \mathbf{M}_e)] = \mathbf{M}_e, \tag{3.14}$$

$$\hat{n} \times [\mathbf{H}_{\text{inc}} + \mathbf{H}_s(\mathbf{J}_e, \mathbf{M}_e)] = \mathbf{J}_e, \tag{3.15}$$

$$\hat{n} \times \mathbf{E}_i(\mathbf{J}_i, \mathbf{M}_i) = \mathbf{M}_i, \tag{3.16}$$

$$-\hat{n} \times \mathbf{H}_i(\mathbf{J}_i, \mathbf{M}_i) = \mathbf{J}_i, \tag{3.17}$$

where $\mathbf{E}_{\text{inc}}$ and $\mathbf{H}_{\text{inc}}$ are the incident electric and magnetic fields, respectively. $\mathbf{E}_s(\cdot)$ and $\mathbf{H}_s(\cdot)$ are, respectively, the integral operators of the electric and magnetic fields evaluated in the homogeneous space of the exterior problem. $\mathbf{E}_i(\cdot)$ and $\mathbf{H}_i(\cdot)$ are the field operators evaluated in the homogeneous space of the interior problem. The

details of these integral operators can be found in Sec. 2.2.2. The exterior-directed normal unit-vector is $\hat{n}$.

The boundary conditions are enforced to couple the exterior and interior problems. The tangential electric fields on the sphere surface are continuous; that is

$$\hat{n} \times [\mathbf{E}_{\text{inc}} + \mathbf{E}_s(\mathbf{J}_e, \mathbf{M}_e)] = \hat{n} \times \mathbf{E}_i(\mathbf{J}_i, \mathbf{M}_i). \tag{3.18}$$

The electrical surface conductivity induces an electrical current in the way of $J_{\text{ind}} = \sigma_E E_{\tan}$; the induced current causes a jump of tangential magnetic fields across the sphere surface. As a result, the boundary condition of the tangential magnetic field becomes

$$\hat{n} \times [\mathbf{H}_{\text{inc}} + \mathbf{H}_s(\mathbf{J}_e, \mathbf{M}_e) - \mathbf{H}_i(\mathbf{J}_i, \mathbf{M}_i)] = \sigma_E \mathbf{E}_{\tan}, \tag{3.19}$$

where $\mathbf{E}_{\tan} = -\hat{n} \times (\hat{n} \times \mathbf{E})$ is the tangential component of the electrical field on the surface and could choose the fields on either side of the surface according to the equality of (3.18).

The boundary conditions (3.18) and (3.19) provide two linearly independent equations for four unknowns, $\mathbf{J}_e$, $\mathbf{M}_e$, $\mathbf{J}_i$, and $\mathbf{M}_i$; thus, it is necessary to find another two equations. Combining (3.14), (3.16) and (3.18) yields the relation of the two magnetic currents; the currents have the same magnitude with the direction flipped:

$$\mathbf{M}_e = -\mathbf{M}_i = \mathbf{M}. \tag{3.20}$$

Therefore, the two unknown magnetic currents $\mathbf{M}_e$ and $\mathbf{M}_i$ can be simply reduced to one variable $\mathbf{M}$. Similarly, combining (3.15), (3.17) and (3.19) yields the relation of the electrical currents on the two sides of the surface

$$\mathbf{J}_e + \mathbf{J}_i = \sigma_E \mathbf{E}_{\tan}. \tag{3.21}$$

Unlike the equivalent magnetic currents, the two electrical currents cannot be simply

reduced to one, because $\mathbf{E}_{\tan}$ in the right-hand-side of (3.21) is an integral operator of the currents. Therefore, it is necessary to use this equation together with (3.18) and (3.19) to solve for the three unknown currents $\mathbf{J}_e$, $\mathbf{J}_i$ and $\mathbf{M}$.

Substituting (3.20) into (3.18) and (3.19), and replacing $\mathbf{E}_{\tan}$ in (3.19) and (3.21) with the tangential electric field on the interior and exterior side of the sphere surface, respectively, yields the complete formulation of type I

$$\hat{n} \times [\mathbf{E}_s(\mathbf{J}_e, \mathbf{M}) - \mathbf{E}_i(\mathbf{J}_i, -\mathbf{M})] = -\hat{n} \times \mathbf{E}_{\text{inc}}, \tag{3.22}$$

$$\hat{n} \times [\mathbf{H}_s(\mathbf{J}_e, \mathbf{M}) - \mathbf{H}_i(\mathbf{J}_i, -\mathbf{M}) + \sigma_E \hat{n} \times \mathbf{E}_i(\mathbf{J}_i, -\mathbf{M})] = -\hat{n} \times \mathbf{H}_{\text{inc}}, \tag{3.23}$$

$$\mathbf{J}_e + \mathbf{J}_i + \sigma_E \hat{n} \times [\hat{n} \times \mathbf{E}_s(\mathbf{J}_e, \mathbf{M})] = -\sigma_E \hat{n} \times (\hat{n} \times \mathbf{E}_{\text{inc}}). \tag{3.24}$$

Note that one can obtain other forms of the type I formulation by replacing the $\mathbf{E}_{\tan}$ with any linear combinations of the tangential electric fields on the exterior side and the interior side of the sphere surface.

The surface conductivity σ_E scales the field operators in (3.23) and (3.24), so variations in σ_E do not affect the field operators.

Given the number of discretized basis functions N on the sphere surface, the type I formulation yields a system of $3N$ equations with $3N$ unknowns, three currents for each basis function.

3.2.2 Formulation Type II based on BVP

Unlike the equivalence principle based derivation of the type I formulation, the type II formulation is derived by solving a two-domain boundary value problem (BVP) governed by Maxwell's equations (similar to the source formulations in [14]). In this derivation, we first obtain the electric and magnetic fields due to equivalent currents, and these fields must satisfy Maxwell's equations in the exterior and interior region, as well as satisfy the boundary conditions at the interface between the two regions. Note that the type II derivation does not require the field-current relations (3.14)-(3.17) associated with the homogeneity in the whole space for each sub-problem.

The unknowns are the same as type I: surface electrical and magnetic currents $\mathbf{J}_e$

and $\mathbf{M}_e$ on the exterior side, and $\mathbf{J}_i$ and $\mathbf{M}_i$ on the interior side of the sphere surface. In the exterior region, the total electric and magnetic fields satisfying Maxwell's equations are $\mathbf{E}_{\text{inc}}+\mathbf{E}_s(\mathbf{J}_e,\mathbf{M}_e)$ and $\mathbf{H}_{\text{inc}}+\mathbf{H}_s(\mathbf{J}_e,\mathbf{M}_e)$, respectively. In the interior region, the total electric and magnetic fields are $\mathbf{E}_i(\mathbf{J}_i,\mathbf{M}_i)$ and $\mathbf{H}_i(\mathbf{J}_i,\mathbf{M}_i)$ respectively. The integral operators $\mathbf{E}_s(\cdot)$ and $\mathbf{H}_s(\cdot)$ relate the scattered electric and magnetic fields to $\mathbf{J}_e,\mathbf{M}_e$, and the integral operators $\mathbf{E}_i(\cdot)$ and $\mathbf{H}_i(\cdot)$ relate the interior electric and magnetic fields to $\mathbf{J}_i$ and $\mathbf{M}_i$. The four field operators are identical to the $\mathbf{E}_s$, $\mathbf{H}_s$, $\mathbf{E}_i$ and $\mathbf{H}_i$ operators for the type I formulation used in (3.14)-(3.17).

In the derivation of the type I formulation $\mathbf{M}_e$, $\mathbf{J}_e$, $\mathbf{M}_i$ and $\mathbf{J}_i$ were assumed to be equal to the surface electric and magnetic fields just outside and just inside the sphere. In the derivation for this alternative formulation, these surface currents $\mathbf{J}_e$, $\mathbf{M}_e$, $\mathbf{J}_i$ and $\mathbf{M}_i$ are fictitious quantities used to generate fields that both satisfy Maxwell's equations and match the boundary conditions. Following the approach in [14], one has freedom to define the relations between the currents on the two sides to reduce the four sets of the currents to two sets. By convention and for simplicity, we constrain the exterior and interior currents to match in magnitudes but have flipped directions

$$\mathbf{J}_e \;=\; -\mathbf{J}_i \;=\; \mathbf{J}, \tag{3.25}$$

$$\mathbf{M}_e \;=\; -\mathbf{M}_i \;=\; \mathbf{M}. \tag{3.26}$$

The four current are thus reduced to $\mathbf{J}$ and $\mathbf{M}$. Substituting (3.25) and (3.26) into the boundary conditions (3.18) and (3.19) yields the type II formulation

$$\hat{n}\times[\mathbf{E}_s(\mathbf{J},\mathbf{M}) - \mathbf{E}_i(-\mathbf{J},-\mathbf{M})] = -\hat{n}\times\mathbf{E}_{\text{inc}}, \tag{3.27}$$

$$\hat{n}\times[\mathbf{H}_s(\mathbf{J},\mathbf{M}) - \mathbf{H}_i(-\mathbf{J},-\mathbf{M}) + \sigma_E\hat{n}\times\mathbf{E}_i(-\mathbf{J},-\mathbf{M})] = -\hat{n}\times\mathbf{H}_{\text{inc}}. \tag{3.28}$$

Compared with the Type I formulation, the type II formulation reduces the number of unknowns by one third, requiring a size of $2N\times 2N$ matrix system.

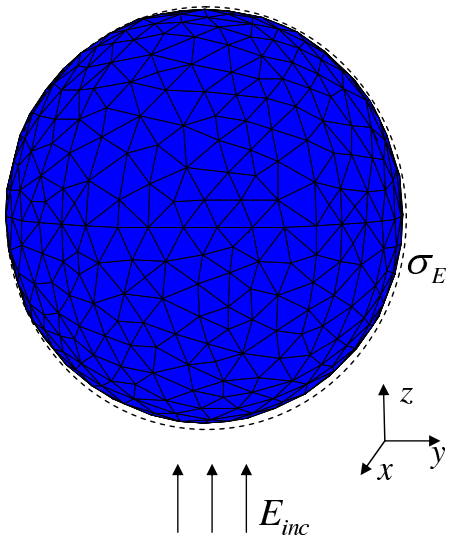

Figure 3-4: A discretized Mie sphere with surface conductivity σ_E.

3.3 Numerical Results and Error Analysis

In this section, the scattered and interior fields by the Mie sphere with surface conductivity are computed by solving discretized versions of the type I and type II BEM formulations, and the numerical results are compared to analytical solutions. The sphere is discretized with triangle panels as shown in Fig. 3-4. The radius of the sphere is $1\lambda_i$, where λ_i is the wavelength in the sphere medium. The center of the sphere is at the origin. The relative permittivities of the sphere and exterior medium are 11.9 and 1. respectively. The relative permeability of both the media is 1.

The first example is a scattering case by a sphere with a small surface conductivity $\sigma_E = 0.01$S. The scattered electric and magnetic fields with respect to θ in a polar coordinate are shown in Fig. 3-5. The fields calculated by the two types of the BEM formulations are completely aligned and perfectly match analytical solutions. To further look into each component of the electric fields, we show the real and imaginary parts of each component of the scattered fields in Fig. 3-6(a) and the interior fields in Fig. 3-6(b). The figure shows excellent agreement of the fields calculated by the two types of BEM formulations with analytical solutions.

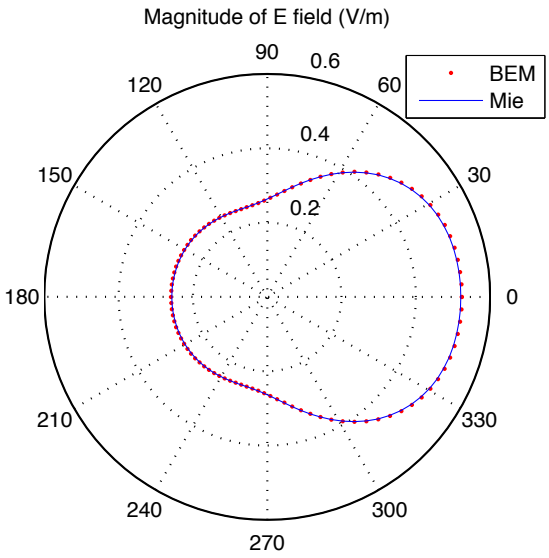

(a) Electric scattered field

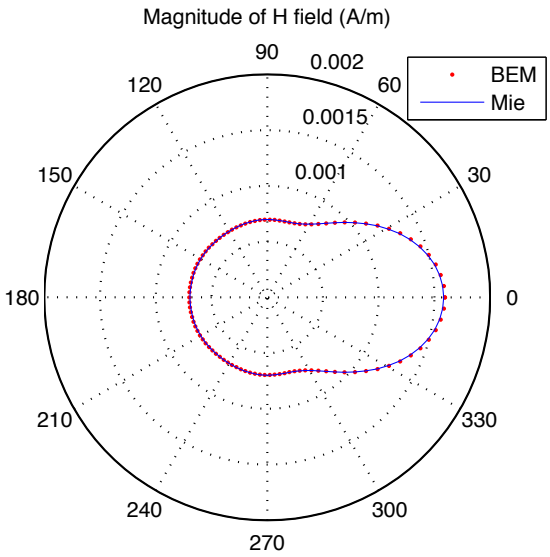

(b) Magnetic scattered field

Figure 3-5: Comparisons of the analytical Mie solution and the two types of the BEM formulations for calculating the magnitude of the scattered fields by a Mie sphere with surface conductivity in a polar coordinate with respect to θ. The radius of the sphere is $1\lambda_i$, and the electrical surface conductivity is 0.01 S. The observation circle is located at $r = 2\lambda_i$, $\varphi = \pi/6$.

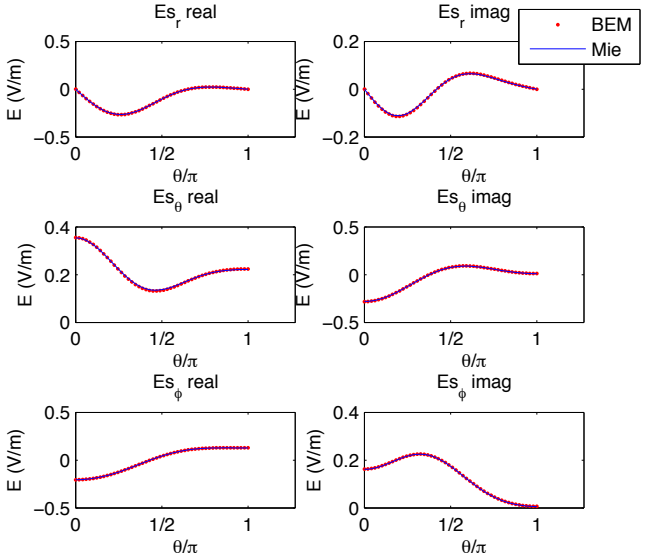

(a) The components of the scattered electric field observed at $r = 2\lambda_i$ and $\varphi = \pi/6$.

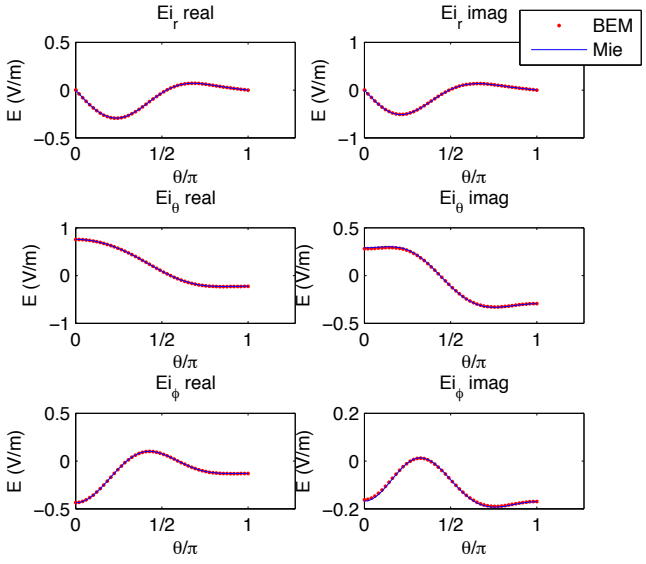

(b) The components of the interior electric field inside the Mie sphere observed at $r = 0.6\lambda_i$ and $\varphi = \pi/6$.

Figure 3-6: Comparisons of the analytical Mie solution and the two types of the BEM formulations for calculating each component of the scattered and interior fields by a Mie sphere with surface conductivity with respect to θ. The radius of the sphere is $1\lambda_i$, and the electrical surface conductivity is 0.01 S.

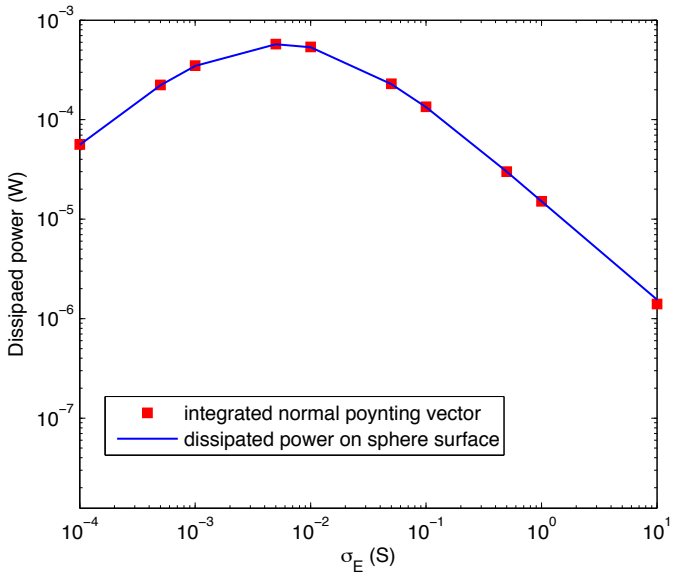

Figure 3-7: The examination of the agreement in the equation (3.29) of the dissipated power on sphere surface versus surface conductivity, calculated by type I formulation.

Applying Poynting's theorem to the sphere with surface conductivity yields

$$-\mathrm{Re}\int_{S^+}\hat{n}\cdot(\mathbf{E}\times\mathbf{H}^*)dS=\int_S\sigma_E|\mathbf{E}_{\tan}|^2dS, \tag{3.29}$$

where S denotes the sphere surface, S^+ denotes the surface of a larger sphere containing the Mie sphere, and $\hat{n}$ is the exterior-directed normal unit vector. The equation basically states that the power dissipation by the surface conductivity should be equal to the real part of the integrated normal-directed Poynting's vector over a closed surface containing the sphere. Fig. 3-7 shows the magnitude of the left side and the right side of (3.29) and examines the agreement in a range of surface conductivity calculated by the type I formulation. Note that the power dissipation does not increase monotonically with the surface conductivity. The reason is that as the electrical surface conductivity grows, more fields are reflected back to the exterior rather than penetrating the sphere surface and being dissipated. In the limit as the surface conductivity approaches to infinity, the sphere will become completely reflective, like a perfectly electrically conductive sphere, and no power will be dissipated.

The accuracy of the two types of BEM as increasing the surface conductivity is investigated. Fig. 3-8(a) shows the magnitudes of the scattered fields at an observation point ($r = 2\lambda_i$, $\theta = 0$), when the electrical surface conductivity increases from 0.001 S to 10 S. The scattered fields using the two types of the BEM formulations are both aligned with analytical solutions in the entire range of the surface conductivity. The relative errors of the two types of formulations for calculating the scattered fields are shown in Fig. 3-9(a). The errors are in the range of $1\% - 2\%$ for this discretization of 2000 triangle panels.

The magnitudes of the interior fields at an observation point ($r = 0.6\lambda_i$, $\theta = 0$) versus surface conductivity are shown in Fig. 3-8(b). As noted above, the sphere becomes more reflective with increasing the surface conductivity, so less waves penetrate into the sphere as σ_E increases. Hence, the magnitude of the interior field decreases with increasing the surface conductivity. As shown in Fig. 3-8(b), the fields calculated using the type I formulation closely follow the analytical solution. However, the type II formulation generates relatively significant numerical error when the surface conductivity increases and the interior field is 100 times smaller than the incident field. Fig. 3-9(b) shows the relative errors versus surface conductivity.

The discrepancy of the BEM calculated interior fields are primarily determined by the type II formulation. With large electrical surface conductivity, the consequent small interior fields require accurate numerical cancellations. However the type II formulation uses the same set of electrical and magnetic currents to calculate both the exterior and interior fields, and thus the smaller interior field is unable to gain the same accuracy as the scattered fields. Table 3.1 shows the average magnitudes of the coefficients of the RWG functions, which are used to approximate the unknown currents, for the two types of formulations. As expected, for the small surface conductivity ($\sigma_E = 0.001$S) example, the magnitudes of the currents of the two types are comparable. For the large surface conductivity ($\sigma_E = 10$S), the currents of the type II formulation remain the same order of magnitude as the corresponding ones for the small conductivity, but those currents are used to generate several orders of magnitudes smaller interior fields. The interior currents of the type I formulation be-

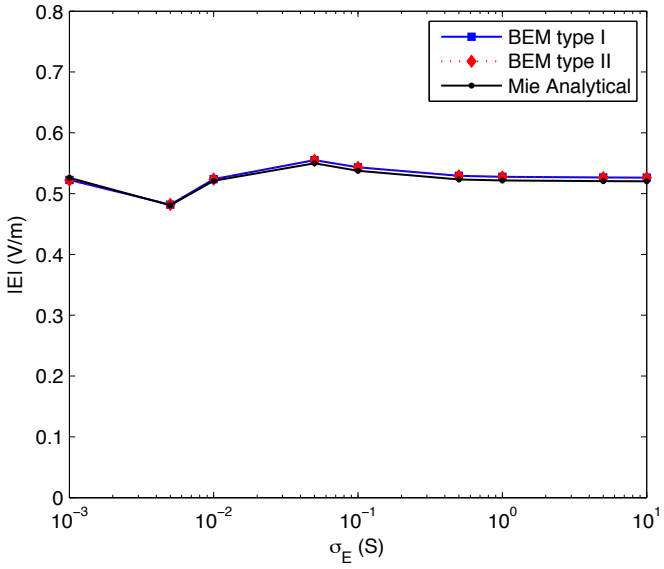

(a) The magnitude of the scattered field observed at $r = 2\lambda_i$, $\theta = 0$.

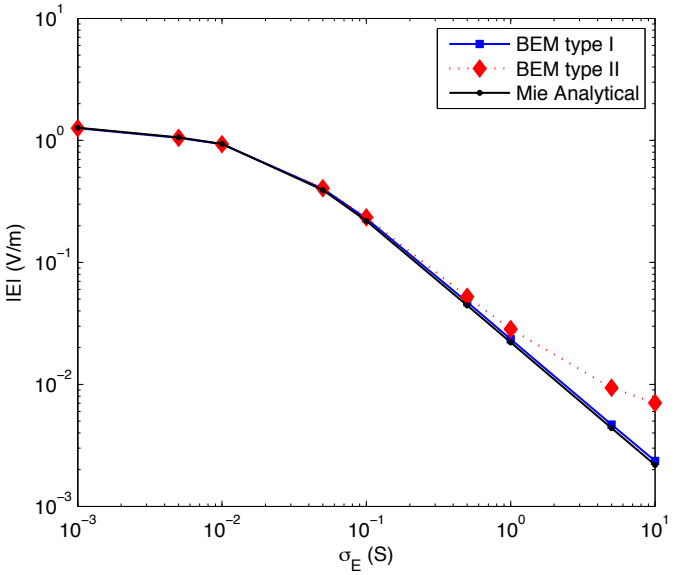

(b) The magnitude of the interior field observed at $r = 0.6\lambda_i$, $\theta = 0$.

Figure 3-8: Comparisons of the analytical Mie solution and the two types of the BEM for calculating the scattered and interior fields of a Mie sphere with surface conductivity, versus electrical surface conductivity σ_E. The radius of the sphere is $1\lambda_i$

comes several orders smaller than the corresponding ones for the small conductivity, and thus the type I formulation is able to approximate the small interior fields more

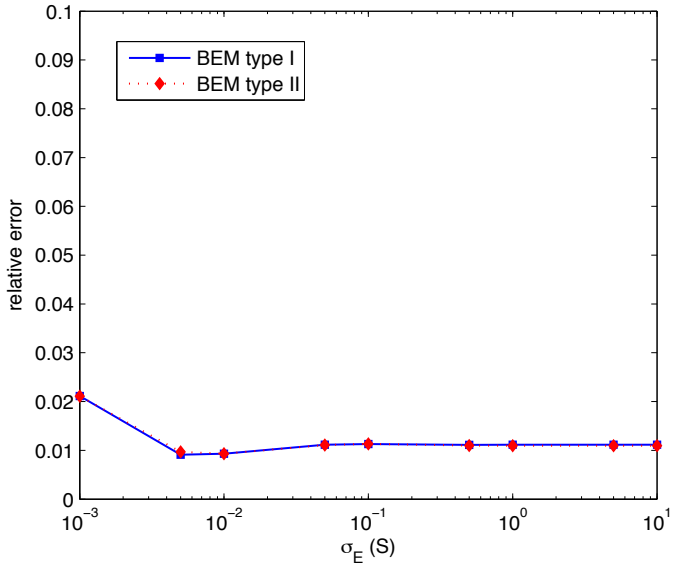

(a) The relative error of scattered electric fields.

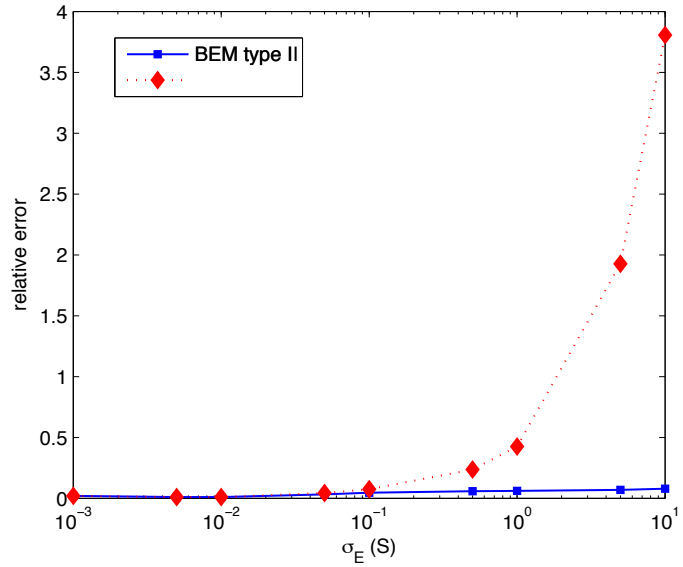

(b) The relative error of interior electric fields.

Figure 3-9: The relative error of scattered and interior fields calculated by the two types of the BEM, versus electrical surface conductivity σ_E.

accurately.

We have demonstrated that the type II formulation is not as accurate as the type I formulation for calculating the interior fields for large surface conductivities, but the calculated interior fields by the type II formulation still converges with discretizations.

Table 3.1: The average magnitudes of the RWG-function coefficients of the unknown currents for the two types of formulations

	$\sigma_E = 0.001$S		$\sigma_E = 10$S	
	Type I	Type II	Type I	Type II
$\mathbf{J}_e$	0.0019	0.0019	0.0023	0.0023
$\mathbf{J}_i$	0.0019	N.A.	1.439×10^{-5}	N.A.
$\mathbf{M}$	0.3393	0.3037	9.554×10^{-4}	0.2435

Fig. 3-10 shows the interior field at an observation point along with the surface conductivities for different discretizations, and it's clear that the numerically calculated field converges to the analytical solution as the mesh becomes finer. The difficulty for the type II formulation to accurately approximate the small interior fields for large surface conductivities results in a large coefficient of the power law convergence with respect to discretizations. The convergence rate of the interior fields calculated using the two formulations are examined in Fig. 3-11 by showing numerical errors versus the number of triangle panels N in discretizations, for four different surface conductivities $\sigma_E = 0.001$S, 0.01S, 1S, 10S. Fig. 3-11(a) shows the error of the interior fields calculated using the type I formulation converges at an identical $\frac{1}{N}$ rate for all the four surface conductivities, and the coefficients for the large conductivities ($\sigma_E =$ 1S, 10S) are about the same order. However, in Fig. 3-11(b), the error calculated using the type II formulation still converges at the $\frac{1}{N}$ rate, but the coefficient of the $\frac{1}{N}$ rate increases dramatically with the surface conductivity. Therefore, it requires a much finer discretization when using the type II formulation for large conductivities to achieve a small error.

The phenomenon of the large coefficient in the power-law convergence of the type II formulation for calculating the interior field when surface conductivity is large, is often not problematic. Because for most scattering cases, one is mostly interested in the scattered fields. Moreover, the convergence with a large power-law coefficient only occurs when the interior field is several orders of magnitude smaller compared with the scattered fields, and thus in general the error can be numerically ignored.

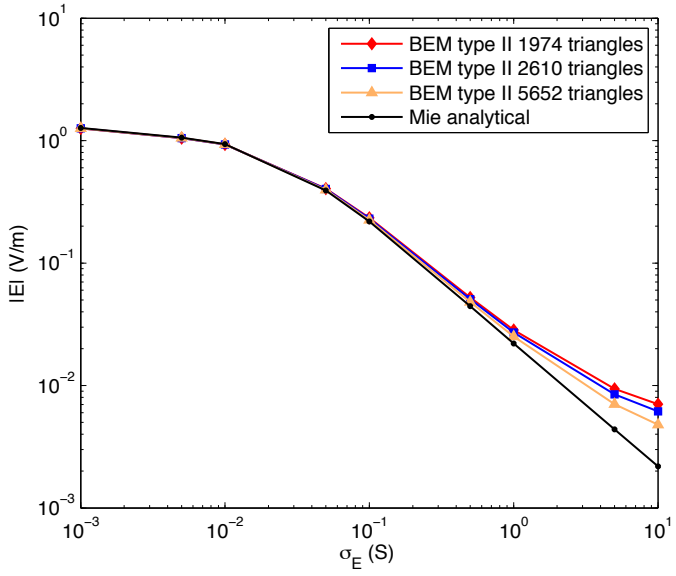

Figure 3-10: The convergence of the magnitude of the interior field calculated by the type II formulation, versus electrical surface conductivity σ_E. The radius of the sphere is $1\lambda_i$. The observation point is at $r = 0.6\lambda_i$, $\theta = 0$.

The two types of the BEM formulations will be further used to analyze surface conductive absorbers in the following chapters. For the type II formulation, the convergence with a large power-law coefficient for calculating the interior field of a Mie sphere with a large surface conductivity will not occur when the type II formulation is used to analyze a surface absorber to truncate a waveguide channel. For the waveguide channel, the excitation source is located in the interior region, and power is localized in the waveguide interior. Thus, the interior field is dominant, like the scattered field in the Mie scattering case. Also, the surface conductivity of the absorber remains small when chosen to minimize transition reflections at the waveguide-absorber interface, which will be discussed in Sec. 4.5. We will compare the numerical results calculated by the two BEM formulations in the next chapter.

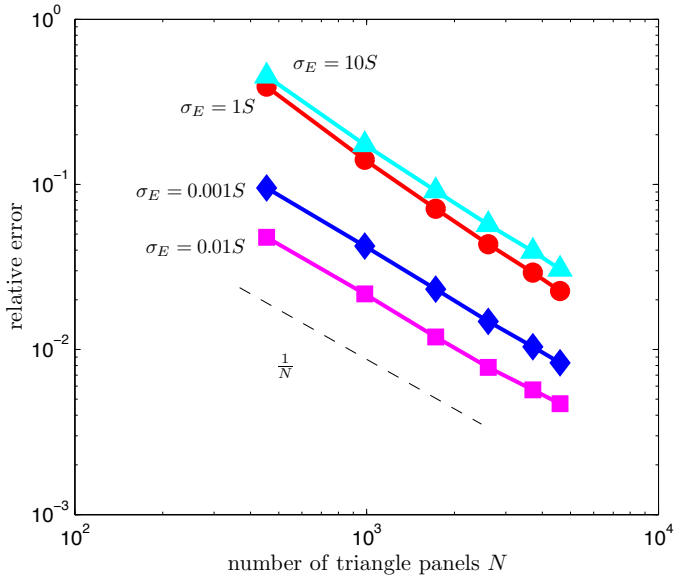

(a) The convergence of the interior fields using the type I formulation.

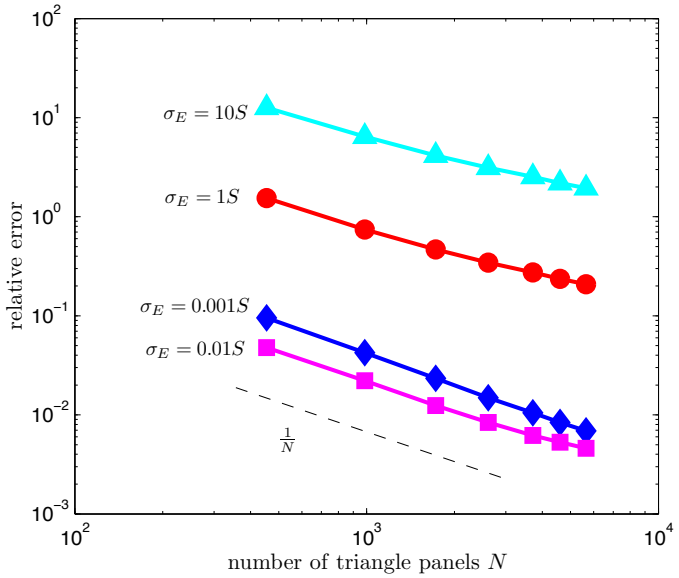

(b) The convergence of the interior fields using the type II formulation.

Figure 3-11: The convergence of the relative errors of BEM calculated interior fields with the number of discretized triangle panels for different surface conductivities.

Chapter 4

Surface Conductive Absorber

In this chapter, we describe an absorber technique for terminating optical waveguides with the boundary element method, which otherwise has difficulties with waveguides and surfaces extending to infinity. In order to attenuate waves reflected from truncated waveguides, we append a region with surface conductivities to the terminations. The transition between the non-absorbing and absorbing regions will generate reflections that can be minimized by making the transition as smooth as possible. We show how this smoothness can be achieved with the surface absorber by smoothly changing integral-equation boundary conditions. Numerical experiments demonstrate that the reflections of our method are orders of magnitude smaller than those of a volume absorber. we show the asymptotic power-law behavior of transition reflections as a function of the length of the surface absorber and demonstrate that the power law is determined by the smoothness of the transition. In addition, we calculate the field decay rate due to the surface conductivity and show a saturation phenomenon of the electrical surface conductivity.

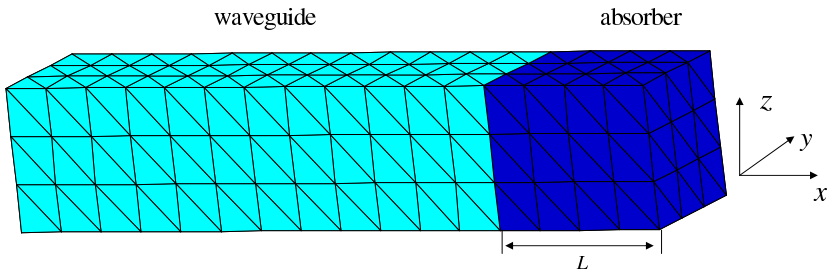

Figure 4-1: A discretized dielectric waveguide with an absorber attached.

4.1 BEM formulations for the Surface Conductive Absorber

In this section, we describe the 3-D BEM formulation for a waveguide truncated with a surface conductive absorber shown in Fig. 4-1. The xz plane cross-section of the x-directed truncated rectangular waveguide is shown in Fig. 4-2, where the surface conductive absorber region is to the right of the dashed line. The permittivity and permeability of the waveguide interior and the exterior media are denoted as ϵ_e, μ_e and ϵ_i, μ_i, where the subscripts e and i denote the exterior and the interior, respectively. The electrical surface conductivity $\sigma_E(\mathbf{r})$ is subscripted with E as a reminder that only electrical conductivity is being considered, though the generalization of what follows to both electrical and magnetic conductivity could be considered. As is described in section 4.4, using only electrical conductivity can have a saturation phenomenon that can be avoided at the cost of using a longer absorber. The system is excited by a Gaussian beam propagating in $+\hat{x}$ direction. The Gaussian beam is generated by a dipole in a complex space [64], where the real part of the dipole position is inside the waveguide, $\frac{1}{4}\lambda_i$ from the left end. The convention of the $e^{j\omega t}$ time-harmonic mode is adopted.

In SIE methods, for computing time-harmonic solutions, the unknowns are surface variables. In our case, we use surface electric and magnetic currents on both the interior, $\mathbf{J}_i$ and $\mathbf{M}_i$, and exterior, $\mathbf{J}_e$ and $\mathbf{M}_e$, of every surface. The currents on surfaces with $\sigma_E = 0$ on the left side of Fig. 4-2, satisfy a simpler set of equations than

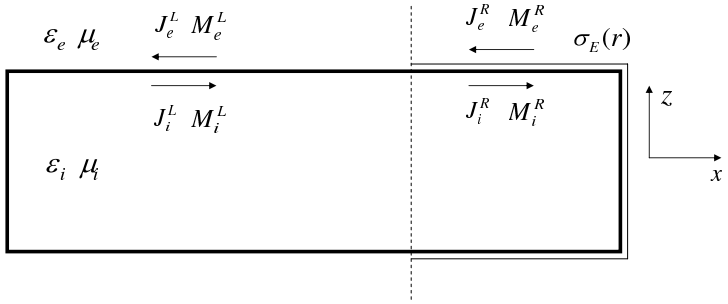

Figure 4-2: The 2-D longitudinal section of a waveguide with a surface conductive absorber. The lengths of the waveguide and absorber are $20\lambda_i$ and $10\lambda_i$, respectively, with λ_i denoting the wavelength in the waveguide medium. The waveguide cross section size is $0.7211\lambda_i \times 0.7211\lambda_i$. The relative permittivities of the waveguide (silicon) and the external medium (air) are 11.9 and 1, respectively.

the currents on surfaces where $\sigma_E \neq 0$, the right side of Fig. 4-2. When appropriate, we distinguish between the $\sigma_E = 0$ and $\sigma_E \neq 0$ currents with superscripts L and R, respectively.

Invoking the equivalence principle [53] yields relations between surface currents and fields, which are similar to (3.14)-(3.17) except for the location of the incident fields, and they are

$$-\hat{n} \times \mathbf{E}_e = \mathbf{M}_e, \tag{4.1}$$

$$\hat{n} \times \mathbf{H}_e = \mathbf{J}_e, \tag{4.2}$$

$$\hat{n} \times (\mathbf{E}_i + \mathbf{E}_{\text{inc}}) = \mathbf{M}_i, \tag{4.3}$$

$$-\hat{n} \times (\mathbf{H}_i + \mathbf{H}_{\text{inc}}) = \mathbf{J}_i, \tag{4.4}$$

where $\hat{n}$ is an exterior-directed normal unit-vector, $\mathbf{E}_{\text{inc}}$, $\mathbf{H}_{\text{inc}}$, are the electric and magnetic fields of the Gaussian beam in a homogeneous space with material parameters equal to those of the waveguide interior, and $\mathbf{E}_e$, $\mathbf{H}_e$ and $\mathbf{E}_i$, $\mathbf{H}_i$ are electric and magnetic fields due to the equivalent currents in the exterior and interior, respectively.

On the surface of the waveguide, the continuity of the tangential components of the electric and magnetic fields yields the well-known PMCHW formulation [14, 15],

which has been described in Sec. 2.2.1, and the equations are

$$\hat{n} \times \mathbf{E}_e^L(\mathbf{J}_e^L, \mathbf{M}_e^L, \mathbf{J}_e^R, \mathbf{M}_e^R) = \hat{n} \times [\mathbf{E}_i^L(\mathbf{J}_i^L, \mathbf{M}_i^L, \mathbf{J}_i^R, \mathbf{M}_i^R) + \mathbf{E}_{\text{inc}}^L], \tag{4.5}$$

$$\hat{n} \times \mathbf{H}_e^L(\mathbf{J}_e^L, \mathbf{M}_e^L, \mathbf{J}_e^R, \mathbf{M}_e^R) = \hat{n} \times [\mathbf{H}_i^L(\mathbf{J}_i^L, \mathbf{M}_i^L, \mathbf{J}_i^R, \mathbf{M}_i^R) + \mathbf{H}_{\text{inc}}^L], \tag{4.6}$$

where $\mathbf{E}^L(\cdot)$ and $\mathbf{H}^L(\cdot)$ are integral operators described in the Appendix. From (4.1)-(4.4) and the tangential field continuity in the surface conductivity free region, the equivalent currents on the two sides of the waveguide surface are of the equal magnitude, but are opposite in direction. Specifically,

$$\mathbf{J}_e^L = -\mathbf{J}_i^L = \mathbf{J}^L, \tag{4.7}$$

$$\mathbf{M}_e^L = -\mathbf{M}_i^L = \mathbf{M}^L. \tag{4.8}$$

Thus, the unknown currents on the waveguide side are reduced to $\mathbf{J}^L$ and $\mathbf{M}^L$.

For the surfaces where $\sigma_E \neq 0$, a modified surface formulation is needed, one that incorporates the discontinuity due to the surface conductivity. In Sec. 3.2, two types of the BEM formulation have been proposed and discussed. Here, we briefly describe them in this surface absorber case. When $\sigma_E \neq 0$, the tangential electric field is still continuous across the absorber surface, and therefore

$$\hat{n} \times \mathbf{E}_e^R(\mathbf{J}_e^L, \mathbf{M}_e^L, \mathbf{J}_e^R, \mathbf{M}_e^R) = \hat{n} \times [\mathbf{E}_i^R(\mathbf{J}_i^L, \mathbf{M}_i^L, \mathbf{J}_i^R, \mathbf{M}_i^R) + \mathbf{E}_{\text{inc}}^R]. \tag{4.9}$$

The tangential magnetic field is not continuous as a sheet of surface electric current $\mathbf{J}_{\text{ind}} = \sigma_E \mathbf{E}_{\text{tan}}^R$ is induced due to the electrical surface conductivity, thus creating a jump. Therefore,

$$\hat{n} \times [\mathbf{H}_e^R(\mathbf{J}_e^L, \mathbf{M}_e^L, \mathbf{J}_e^R, \mathbf{M}_e^R) - \mathbf{H}_i^R(\mathbf{J}_i^L, \mathbf{M}_i^L, \mathbf{J}_i^R, \mathbf{M}_i^R) - \mathbf{H}_{\text{inc}}^R] = \sigma_E \mathbf{E}_{\text{tan}}^R, \tag{4.10}$$

where $\mathbf{E}_{\text{tan}}^R = -\hat{n} \times (\hat{n} \times \mathbf{E}^R)$ is the tangential electric field on the absorber surface, and could choose the field on either side of the absorber surface according to the enforced equality in (4.9).

As a result of (4.1), (4.3) and (4.9), the interior and exterior magnetic currents can be represented with a single variable

$$\mathbf{M}_e^R = -\mathbf{M}_i^R = \mathbf{M}^R. \tag{4.11}$$

For the type I formulation, the discontinuity of tangential magnetic field implies $|\mathbf{J}_e^R| \neq |\mathbf{J}_i^R|$, and (4.2), (4.4), and (4.10) must be combined to generate a local equation

$$\mathbf{J}_e^R + \mathbf{J}_i^R = \sigma_E \mathbf{E}_{\tan}^R. \tag{4.12}$$

Finally, using the integral operator relation between $\mathbf{E}_{\tan}^R$ and $\mathbf{J}$ and $\mathbf{M}$, and substituting into (4.10), (4.12), yields

$$\begin{aligned} \hat{n} \times [\mathbf{H}_e^R(\mathbf{J}_e^L,\mathbf{M}_e^L,\mathbf{J}_e^R,\mathbf{M}_e^R) - \mathbf{H}_i^R(\mathbf{J}_i^L,\mathbf{M}_i^L,\mathbf{J}_i^R,\mathbf{M}_i^R) \\ -\mathbf{H}_{\text{inc}}^R] = \sigma_E \mathbf{E}_{e,\tan}^R(\mathbf{J}_e^L,\mathbf{M}_e^L,\mathbf{J}_e^R,\mathbf{M}_e^R), \end{aligned} \tag{4.13}$$

$$\mathbf{J}_e^R + \mathbf{J}_i^R = \sigma_E[\ \mathbf{E}_{i,\tan}^R(\mathbf{J}_i^L,\mathbf{M}_i^L,\mathbf{J}_i^R,\mathbf{M}_i^R) + \mathbf{E}_{\text{inc},\tan}^R]. \tag{4.14}$$

Thus, the type I formulation has five sets of unknowns, the surface currents $\mathbf{J}^L$, $\mathbf{M}^L$, $\mathbf{J}_e^R$, $\mathbf{J}_i^R$ and $\mathbf{M}^R$, and they can be determined by solving equations (4.5), (4.6) on the left waveguide surfaces and (4.9), (4.13), (4.14) on the right absorber surfaces.

For the type II formulation, the electrical currents on the two sides of the absorber surface are forced to be equal in magnitude and opposite in sign, and they are

$$\mathbf{J}_e^R = -\mathbf{J}_i^R = \mathbf{J}^R. \tag{4.15}$$

Then the electrical currents on the absorber surface are reduced to one set, the same as the magnetic currents. Thus, the type II formulation has four sets of unknowns, the surface currents $\mathbf{J}^L$, $\mathbf{M}^L$, $\mathbf{J}^R$ and $\mathbf{M}^R$, and they can be determined by solving equations (4.5), (4.6) on the left waveguide surfaces and (4.9), (4.10) on the right absorber surfaces.

4.2 Solving A Linear System

4.2.1 Construction of A Linear System

From section 4.1, the equivalent currents on the waveguide surfaces and the absorber surfaces, are to be determined by solving the equations (4.5), (4.6), (4.9), (4.13) and (4.14) for the type I formulation or the equations (4.5), (4.6), (4.9) and (4.10) for the type II formulations. The currents are approximated with the RWG basis function [1] on triangular-meshed surfaces,

$$\mathbf{J} = \sum_m J_m \mathbf{X}_m(\mathbf{r}'), \tag{4.16}$$

$$\mathbf{M} = \sum_m M_m \mathbf{X}_m(\mathbf{r}'), \tag{4.17}$$

where $\mathbf{X}_m(\mathbf{r}')$ is the RWG function on the mth triangle pair, and J_m, M_m are the corresponding coefficients for the electric and magnetic currents, respectively. These unknown coefficients of the five equivalent currents assemble a vector $\mathbf{x}$ to be solved for, specifically, for the type I formulation the vector $\mathbf{x}$ is

$$\mathbf{x} = \left[\begin{array}{ccccc} J^L & M^L & J_e^R & J_i^R & M^R \end{array} \right]^T, \tag{4.18}$$

and for the type II formulation, the unknown vector $\mathbf{x}$ is

$$\mathbf{x} = \left[\begin{array}{cccc} J^L & M^L & J^R & M^R \end{array} \right]^T. \tag{4.19}$$

Electric and magnetic fields are represented using the mixed-potential integral equation (MPIE) [16] for a low-order singularity, with integral operators L and K as in (2.23) and (2.24). The details of the integral operators L and K can be found in Sec. 2.2.2.

We employ Galerkin method [55] on the waveguide by using the RWG function as the testing function on target triangle pairs. The tested L, K operators on the nth

target triangle pair due to the mth source triangle pair become

$$\mathcal{L}^t_{l,nm}(\mathbf{X}_m) = \int_S \mathbf{X}_n(\mathbf{r}) \cdot L^t_l(\mathbf{X}_m) dS, \tag{4.20}$$

$$\mathcal{K}^t_{l,nm}(\mathbf{X}_m) = \int_S \mathbf{X}_n(\mathbf{r}) \cdot K^t_l(\mathbf{X}_m) dS, \tag{4.21}$$

where S is the surface of the nth target triangle pair, and $\mathbf{X}(\mathbf{r})$ is the RWG function. The subscript $l = e$ or i denotes the exterior or interior region, and the superscript $t = L$ or R denotes the waveguide or absorber surfaces. Substituting the tested field operators into equations (4.5), (4.6) yields a matrix $\mathbf{A}_{LL}$ due to the currents $\mathbf{J}^L$, $\mathbf{M}^L$, and a matrix $\mathbf{A}_{LR}$ due to the currents $\mathbf{J}^R_e$, $\mathbf{J}^R_i$, $\mathbf{M}^R$.

On the absorber surfaces, the term $\sigma_E(\mathbf{r})\mathbf{E}^R_{l,\tan}$ in (4.13) and (4.14) requires another testing procedure in order to incorporate the surface conductivity

$$\mathcal{L}^{R\sigma_E}_{l,nm}(\mathbf{X}_m) = \int_S \sigma_E(\mathbf{r})\mathbf{X}_n(\mathbf{r}) \cdot L^R_l(\mathbf{X}_m) dS, \tag{4.22}$$

$$\mathcal{K}^{R\sigma_E}_{l,nm}(\mathbf{X}_m) = \int_S \sigma_E(\mathbf{r})\mathbf{X}_n(\mathbf{r}) \cdot K^R_l(\mathbf{X}_m) dS. \tag{4.23}$$

Similarly, substituting the above four tested integral operators into (4.9), (4.10), (4.13) and (4.14) generate a matrix $\mathbf{A}_{RL}$ due to the currents on the waveguide surfaces and a matrix $\mathbf{A}_{RR}$ due to the currents on the absorber surfaces.

Assembling the four matrices according to (4.5), (4.6), (4.9), (4.13) and (4.14) for the type I formulation or (4.5), (4.6), (4.9) and (4.10) for the type II formulation yields a dense linear system

$$\mathbf{A}\mathbf{x} = \mathbf{b}, \tag{4.24}$$

where

$$\mathbf{A} = \begin{bmatrix} \mathbf{A}_{LL} & \mathbf{A}_{LR} \\ \mathbf{A}_{RL} & \mathbf{A}_{RR} \end{bmatrix}. \tag{4.25}$$

The right-hand-side vector $\mathbf{b}$ contains tested incident electric and magnetic fields,

and the vector $\mathbf{b}$ for the type I formulation is

$$\mathbf{b} = \begin{bmatrix} b_E^L & b_H^L & b_E^R & b_H^R & b_{E\sigma}^R \end{bmatrix}^T, \tag{4.26}$$

and the vector $\mathbf{b}$ for the type II formulation is

$$\mathbf{b} = \begin{bmatrix} b_E^L & b_H^L & b_E^R & b_H^R \end{bmatrix}^T, \tag{4.27}$$

in which the nth entry of each subvector is given by

$$b_{E,n}^t = \int_S \mathbf{X}_n(\mathbf{r}) \cdot \mathbf{E}_{\text{inc}}^t(\mathbf{r}) dS, \tag{4.28}$$

$$b_{H,n}^t = \int_S \mathbf{X}_n(\mathbf{r}) \cdot \mathbf{H}_{\text{inc}}^t(\mathbf{r}) dS, \tag{4.29}$$

$$b_{E\sigma,n}^R = \int_S \sigma_E(\mathbf{r}) \mathbf{X}_n(\mathbf{r}) \cdot \mathbf{E}_{\text{inc}}^t(\mathbf{r}) dS. \tag{4.30}$$

4.2.2 Acceleration and Preconditioning with FFT

The linear system (4.24) can be solved with iterative algorithms, for instance, GMRES for this non-symmetrically dense system. In each iteration, the matrix-vector product takes $O(N^2)$ time, where N is the number of unknowns. Moreover, to explicitly store the matrix $\mathbf{A}$ is expensive, requiring $O(N^2)$ memory. In fact, there have been many well-developed fast algorithms to reduce the costs of the integral equation solvers [26–29]. Here, we use a straightforward and easily-implemented FFT-based fast algorithm to accelerate the SIE method on periodic guided structures.

As shown in Fig. 4-3, the waveguide is discretized into a periodically repeating set of the RWG triangle pairs. Due to the mesh periodicity and the space invariance of the operators (4.20), (4.21), the matrices $\mathbf{A}_{LL}$ and $\mathbf{A}_{LR}$ are block Toeplitz, requiring explicit calculation and storage of only a block row and a block column, reducing memory to approximately $O(N)$. A Toeplitz matrix can be embedded in a circulant matrix, and the circulant matrix-vector product can be computed with the FFT [36, 65]. In this way, the computational costs are reduced approximately to $O(N \log N)$.

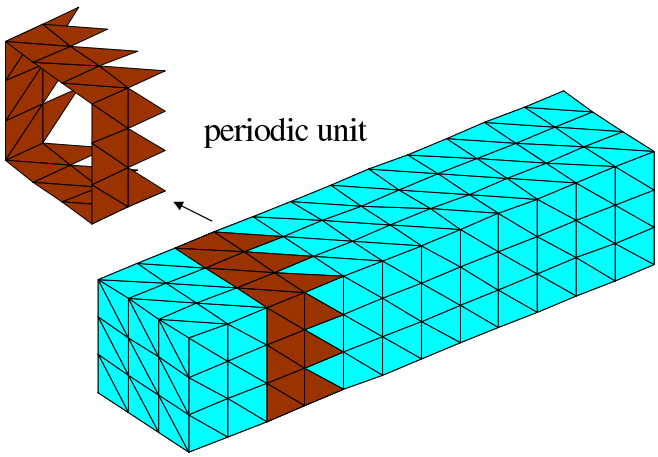

Figure 4-3: A discretized waveguide with a periodic unit.

Because the surface conductivity σ_E must vary with distance from the waveguide-absorber interface, the tested potential operators (4.22), (4.23) are not space invariant. Therefore, accelerating the σ_E parameterized matrices $\mathbf{A}_{RL}$ and $\mathbf{A}_{RR}$ is not as straightforward as $\mathbf{A}_{LL}$ and $\mathbf{A}_{LR}$. Typically, the integral of (4.22), (4.23) is calculated numerically using Gauss quadrature [56], summing up the tested potentials at quadrature (target) points with Gauss weights. For instance, (4.22) is numerically calculated through

$$\mathcal{L}^{R\sigma_E}_{l,nm}(\mathbf{X}_m) = A_n \sum_{k=1}^{K} \omega_k \sigma_E(\mathbf{r}_k) \mathbf{X}_n(\mathbf{r}_k) \cdot L^R_{l,k}(\mathbf{X}_m), \tag{4.31}$$

where $\mathbf{r}_k$ is the kth quadrature point of the nth RWG triangle pair, ω_k is the Gauss weight of the kth point, A_n is the area of the nth triangle pair, and $L^R_{l,k}(\mathbf{X}_m)$ is the potential L evaluated at the k the quadrature point due to the currents on the mth RWG triangle pair. The space invariance of the potential operators L in (2.25) and K in (2.26) and periodicity of the mesh allows assembling a matrix of the potentials $L^R_{l,k}(\mathbf{X}_m)$ and $K^R_{l,k}(\mathbf{X}_m)$ at target points by explicitly calculating only a block row and block column of that matrix. Then the potentials at target points are summed after testing and multiplications with Gauss weights and surface conductivity as in (4.31), and eventually stamped into matrices $\mathbf{A}_{RL}$ and $\mathbf{A}_{RR}$.

Another great advantage of working with a Toeplitz or a block Toeplitz matrix is the existence of a highly efficient preconditioner [66–68]. A circulant matrix is approximated from the Toeplitz matrix, and then can be easily inverted with the FFT. We use this method to calculate a preconditioner for $\mathbf{A}_{LL}$, and use the block-diagonal preconditioner [29] for $\mathbf{A}_{RR}$.

4.3 Numerical Results of Absorbers

In this section, we will present numerical results of the surface conductive absorber using the boundary element method described in the last two sections. But before that, we show examples of a straight-forward volume conductive absorbers with constant electrical and magnetic volume conductivities. The constant volume conductivities are required by the piecewise homogeneity limitation of the general boundary element method using the homogeneous Green's function, and therefore we are not allowed handling varying volume conductivity. The volume absorber can effectively absorb the propagating wave, but the large material transition at the waveguide-absorber interface generates significant reflections. Instead, the surface conductive absorber with quadratically increasing surface conductivity can reduce reflections by as much as 45dB.

4.3.1 Volume Conductive Absorbers

With SIE methods, one could, in principle, implement a scalar waveguide absorption in a piecewise homogeneous fashion as a discontinuous increase in absorption, but this will obviously generate large reflections due to the discontinuity of the medium and also the numerical reflection due to the discretization of the interfaces. We demonstrate this with a finite rectangular waveguide, to which an absorber with constant volume electrical conductivity σ_E and magnetic conductivity σ_M is attached. The longitudinal cross-section of this arrangement is shown in Fig. 4-4. To achieve small reflections, the intrinsic impedance of the absorber is matched to that of the waveguide. Hence, the electrical volume conductivity σ_E and the magnetic volume

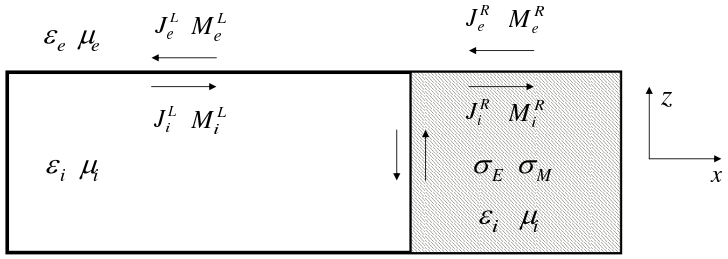

Figure 4-4: The 2-D cross section of a waveguide with a *volume* absorber. The lengths of the waveguide and absorber are $20\lambda_i$ and $10\lambda_i$, respectively, with λ_i denoting the wavelength in the waveguide medium. The waveguide cross section size is $0.7211\lambda_i \times 0.7211\lambda_i$. The relative permittivities of the waveguide (silicon) and the external medium (air) are 11.9 and 1, respectively

conductivity σ_M should satisfy $\sigma_E/\sigma_M = \epsilon_i/\mu_i$, where ϵ_i and μ_i are the permittivity and permeability of both the waveguide and absorber media, respectively.

We quantify the reflection by use of the standing wave ratio (SWR), the ratio of the maximum field magnitude to the minimum field magnitude in the standing-wave region, evaluated on the waveguide axis. From the SWR, a reflection coefficient is then readily obtained as in a conventional transmission line. The first example is a short volume conductive absorber with constant volume conductivities. The lengths of the waveguide and the attached volume absorber in this example are $20\lambda_i$ and $10\lambda_i$, respectively, where λ_i is the wavelength in the interior region. We calculated the field reflection coefficients in this way for a range of σ_E and σ_M, and the smallest field reflection coefficient obtained was 2.5% when $\sigma_E = 0.0087$ S/m. Fig. 4-5 shows the complex magnitude of the corresponding electric field along the central axis. In this complex magnitude plot, the peak-to-peak magnitudes of ripples are an indication of the amount of reflections. Obviously, the large ripples in the plot indicate significant reflections. The reflection coefficient, which is listed in the first column of Table 4.1, is unacceptable for many design applications. In particular, the design of tapers [6] requires field reflection from terminations in the order of 10^{-3} or smaller.

The volume absorber is then made much longer with a smaller volume conductivity in order to reduce the discontinuity of the material at the interface. Fig. 4-6 shows the complex magnitudes of the electric field when the absorber length is increased

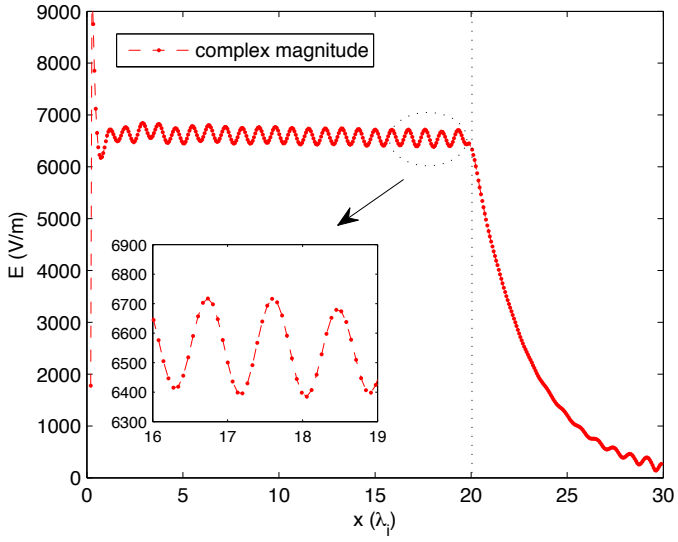

Figure 4-5: The complex magnitude of the electric field inside a waveguide and a volume absorber of constant electrical and magnetic conductivity. The lengths of the waveguide and the volume absorber are $20\lambda_i$ and $10\lambda_i$, respectively. The constant electrical volume conductivity of the volume absorber is $\sigma_E = 0.0087$ S/m. The dashed line indicates the position of the waveguide-absorber interface.

to $60\lambda_i$ and the electrical volume conductivity is reduced to $\sigma_E = 0.0015$ S/m. The ratio of the electrical and magnetic conductivities is still fixed. In Fig. 4-6, the size of the ripples of the complex magnitudes is reduced (clearly shown in the inset), and the numerically measured field reflection coefficient is 1.09%, still larger than the tolerance of most applications. Evidently, a more sophisticated way of terminating waveguides is called for.

4.3.2 Surface Conductive Absorbers

Unlike the volume conductive absorber shown in the last section, the surface conductive absorber can significantly reduce reflections by using a short absorber due to the capability of smoothly increasing the conductivity from the waveguide-absorber interface. As shown in Fig. 4-2, a waveguide attached with a surface absorber of the same short length ($10\lambda_i$) as the volume absorber in the last section is computed using the type I boundary element method formulation described in Sec. 4.1 and Sec. 4.2.

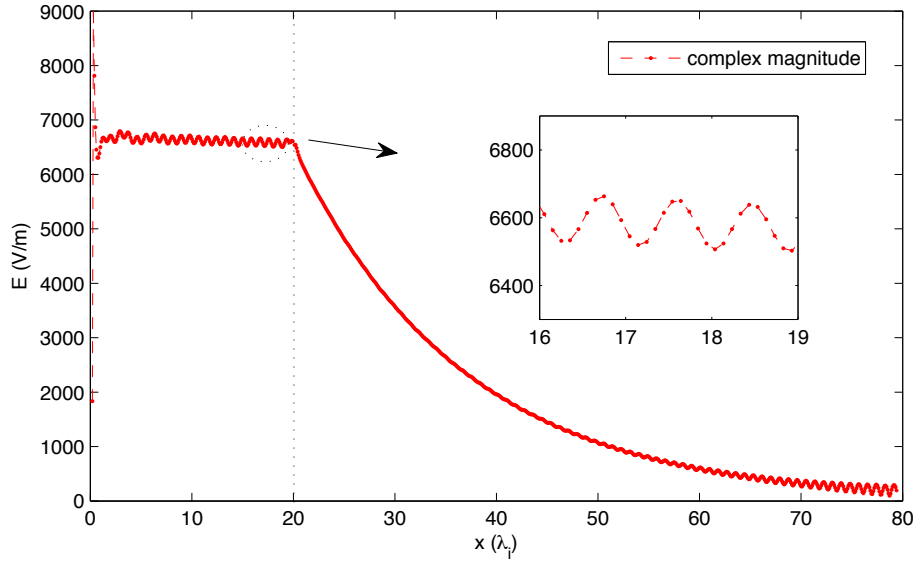

Figure 4-6: The complex magnitude of the electric field inside a waveguide and a volume absorber of constant electrical and magnetic conductivity. The lengths of the waveguide and the volume absorber are $20\lambda_i$ and $60\lambda_i$, respectively. The constant electrical volume conductivity of the volume absorber is $\sigma_E = 0.0015$ S/m

In Fig. 4-7, we show the numerically computed complex magnitudes of the electric field along the x direction inside a rectangular waveguide with several different surface absorbers. The surface absorber is in the region where $x_0 < x < (x_0 + L)$ in which x_0 is the position of the interface and L is the absorber length. The surface electrical conductivity in this region is given by $\sigma_E(x) = \sigma_0(\frac{x-x_0}{L})^d$, where $d = 0, 1, 2$ for constant, linear and quadratic profiles. The constant σ_0 is chosen so that the total attenuation over the length of the absorbing region matches that of the optimal volume absorber above. The approach for calculating the attenuation along the absorber was explained in Sec. 2.1. As is easily seen in Fig. 4-7, there are substantial reflections when using a constant conductivity, smaller reflections when using a linearly increasing conductivity, and almost no reflections for a quadratically increasing conductivity. The magnitudes of the field reflection coefficients r are listed in Table 4.1, and show that the reflection coefficient for the quadratically varying surface conductivity is nearly one thousand times smaller than the reflection coefficient for the volume absorber. The results for the constant, linearly and quadratically varying

Table 4.1: The Standing wave ratio (SWR) and field reflection versus the conductivity distribution of the absorber, whose length is $10\lambda_i$.

Absorber type	Volume	Surface		
Conductivity profile	Constant	Constant	Linear	Quadratic
SWR	1.0503	1.0509	1.0022	1.0002
Reflection R(dB)	-32.2	-32.1	-59.2	-79.7

surface absorber verify the results in [24], that the smoothness of any transition in the waveguide largely determines the resulting reflection.

We further compare the fields calculated using the two types of the BEM formulations. We use a quadratic conductivity function $\sigma_E(x) = 0.01(\frac{x-x_0}{L})^2$ S, where x_0 is the position of the waveguide absorber interface and L is the absorber length. Fig. 4-8 shows the magnitude of the electric field along the center of the waveguide and absorber. As expected, the two types of the BEM generate the same results, while the type II BEM reduces the unknowns of on the absorber surface by one third.

4.4 The Field Decay Rate Due to the Electrical Surface Conductivity

In this section, the exponential decay rate of waves propagating through the surface absorber region is analyzed. We demonstrate the relation between the decay rate and the surface conductivity using an example of a single dielectric waveguide with uniformly distributed surface conductivity. The longitudinal cross-section is shown in Fig. 4-9. The behavior of the interior fields generated by a Gaussian beam source were computed using a BEM method based on solving (4.9), (4.13) and (4.14).

The plot in Fig. 4-10 shows the complex magnitudes of the electric fields along the x axis inside the waveguide for two cases, $\sigma_E = 0.001$ S and $\sigma_E = 0.002$ S. As expected, the complex magnitude decays exponentially with distance from the source with a surface-conductivity dependent rate. Also, as can be seen, waves reflect back

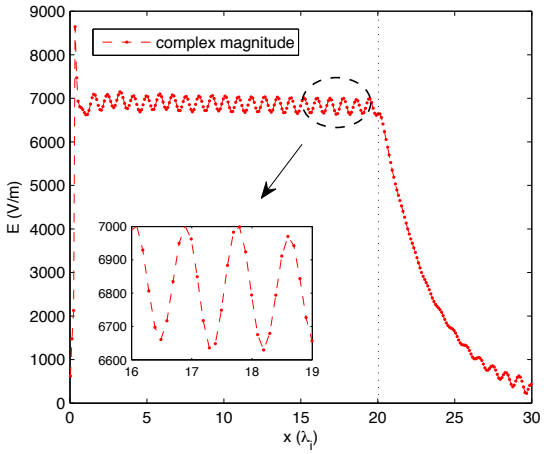

(a) constant surface conductivity

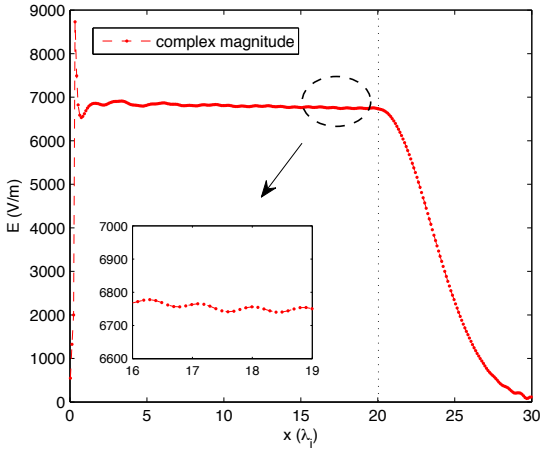

(b) linear surface conductivity along x direction

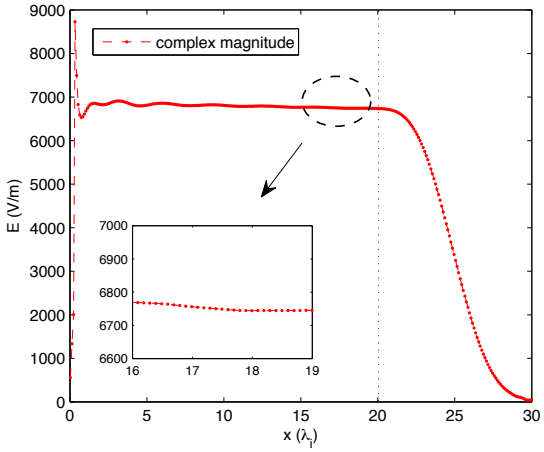

(c) quadratic surface conductivity along x direction

Figure 4-7: The complex magnitude of the electric field inside a waveguide and a surface absorber. The dashed line indicates the position of the waveguide-absorber interface.

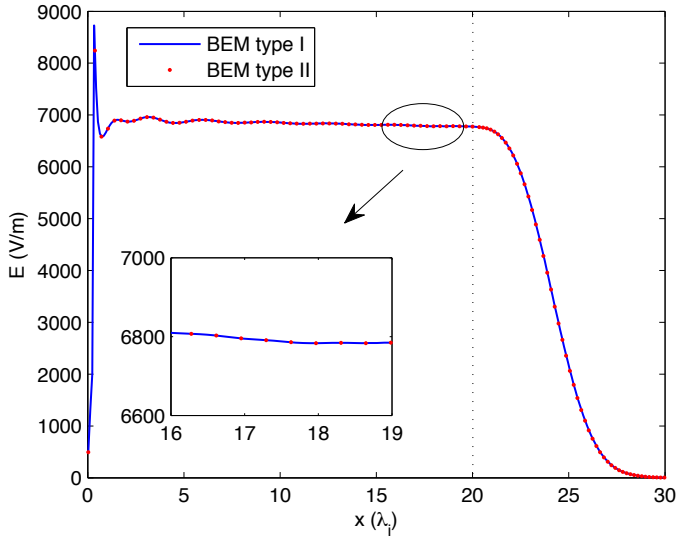

Figure 4-8: The complex magnitude of the electric field inside a waveguide and a surface absorber. The dashed line indicates the position of the absorber interface

from the right end and presumably these reflections decay as they travel to the left.

An approximation to the rate of exponential decay can be determined by fitting the field plots. The fitted decay rates for a range of σ_E are shown in Fig. 4-11 and denoted with a dashed star curve. The decay rate does not monotonically increase with the surface conductivity. The curve shape can be explained as follows. When σ_E is small, the propagating wave is able to penetrate the lossy surface and is absorbed, with the absorption increasing with σ_E as expected. However, for large σ_E,

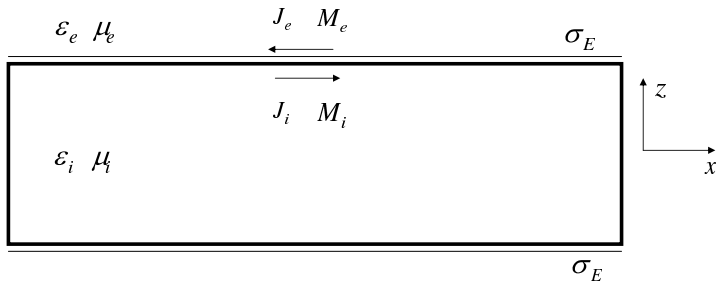

Figure 4-9: The 2-D longitudinal section of a waveguide with uniform surface conductivity. The waveguide length is $10\lambda_i$ and cross section size is $0.7211\lambda_i \times 0.7211\lambda_i$. The relative permittivity of the waveguide and external medium are 11.9 and 1, respectively.

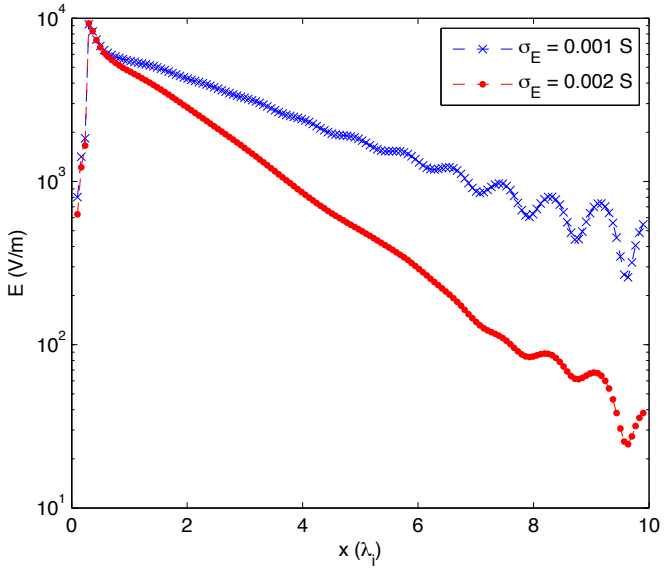

Figure 4-10: The complex magnitude of the electric field along x inside the waveguide in Fig. 4-9 with uniform surface conductivity.

the surface conductor itself becomes reflecting, forming essentially an enclosed metallic waveguide; as $\sigma_E \to \infty$ the tangential electric field vanishes at the surface and therefore there is no absorption. The practical implications of this upper bound on effective values for σ_E are limited, and are described in section 4.5.

The following sections introduce two alternative approaches to calculate the decay rate from surface conductivities, to confirm and further illustrate the numerical observations above.

4.4.1 Decay rate calculation by perturbation theory

In this section, a first-order closed-form decay rate formula, valid for low surface conductivity, is derived using perturbation theory.

Assume the electric field $\mathbf{E}^{(0)}(\mathbf{r})$ of the fundamental mode of a lossless rectangular waveguide is given, and the superscript (0) denotes the unperturbed quantity. When electrical surface conductivity σ_E is put on the waveguide surface, it is equivalent to

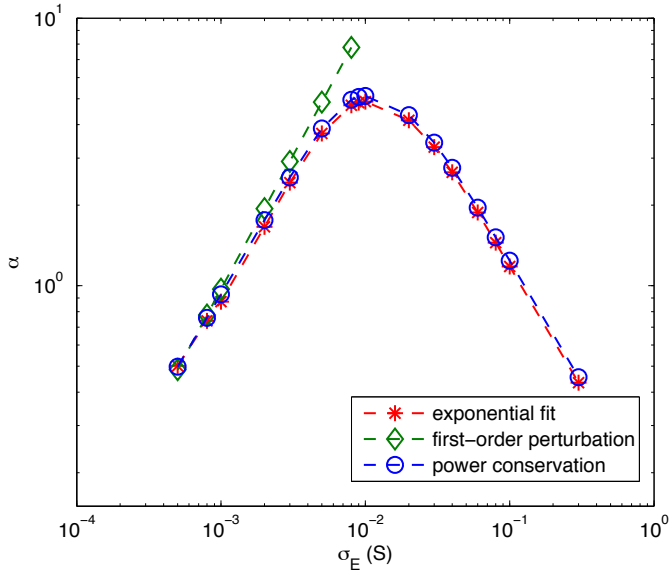

Figure 4-11: A comparison of three methods for computing the rate of field exponential decay along the propagation direction versus surface conductivity.

a perturbation of permittivity, denoted as

$$\Delta\epsilon(\mathbf{r}) = -\frac{j\sigma_E}{\omega}\delta_S(\mathbf{r}), \tag{4.32}$$

where $\delta_S(\mathbf{r})$ is the Dirac delta function across the waveguide surface. According to [53], [2], the first-order variance of angular frequency due to the perturbation of permittivity $\Delta\epsilon(\mathbf{r})$ is

$$\Delta\omega^{(1)} = -\frac{\omega}{2}\frac{\int_V \Delta\epsilon(\mathbf{r})|\mathbf{E}^{(0)}(\mathbf{r})|^2 dV}{\int_V \epsilon|\mathbf{E}^{(0)}(\mathbf{r})|^2 dV}, \tag{4.33}$$

where V is the whole volume domain and the superscript (1) denotes a first-order approximation. Apply the triple product rule to the three interdependent variables ω, k, σ_E. The total derivative $d\omega$ can be written as

$$d\omega = \left.\frac{\partial\omega}{\partial\sigma_E}\right|_k d\sigma_E + \left.\frac{\partial\omega}{\partial k}\right|_{\sigma_E} dk, \tag{4.34}$$

where the variable in the subscript on the right of $|$ is held constant when the derivative

on the left of | is taken. Holding ω constant yields $d\omega = 0$ and $dk = \frac{\partial k}{\partial \sigma_E}\Big|_\omega d\sigma_E$. Substituting these two equations into (4.34) yields

$$\frac{\partial \omega}{\partial \sigma_E}\bigg|_k + \frac{\partial \omega}{\partial k}\bigg|_{\sigma_E} \frac{\partial k}{\partial \sigma_E}\bigg|_\omega = 0. \tag{4.35}$$

From (4.35), we obtain

$$\frac{\partial \omega}{\partial k}\bigg|_{\sigma_E} = -\frac{\partial \omega}{\partial \sigma_E}\bigg|_k \frac{\partial \sigma_E}{\partial k}\bigg|_\omega = -\frac{\partial \omega}{\partial k}. \tag{4.36}$$

As we know, the group velocity is $V_g = \frac{\partial \omega}{\partial k}|_{\sigma_E}$. Therefore, the left side of (4.36) can be replaced with V_g, and it becomes $V_g = -\frac{\partial \omega}{\partial k}$. Then we obtain a first-order change in propagation constant k due to the frequency change in (4.33), denoted as $\Delta k^{(1)} = -\frac{\Delta \omega}{V_g}$. Combining (4.32), (4.33) and the $\Delta k^{(1)}$ equation above, the integral in the numerator of (4.33) is reduced to a surface integral of the tangential components of the electric field, therefore

$$\Delta k^{(1)} = -\frac{j\sigma_E}{2V_g} \frac{\int_S |\mathbf{E}^{(0)}_{\tan}(\mathbf{r})|^2 dS}{\int_V \epsilon |\mathbf{E}^{(0)}(\mathbf{r})|^2 dV}, \tag{4.37}$$

where S is the surface of the waveguide. As expected, the perturbation in the propagation constant is imaginary, which in turn represents the decay rate $\alpha^{(1)} = -\mathrm{Im}\{\Delta k^{(1)}\}$. With a uniform cross section, the volume and surface integrals in (4.37) can be further reduced to surface and line integrals on the cross section, respectively. The electric field before the perturbation $\mathbf{E}^{(0)}(\mathbf{r})$, along with V_g, can be obtained numerically, for example, with a planewave method [33].

The decay rate calculated using the perturbation is plotted in Fig. 4-11 with a dashed diamond curve. Note that the curve overlaps with decay rates computed with other methods when the surface conductivity is small, and deviates for larger conductivity as should be expected given the first-order approximation.

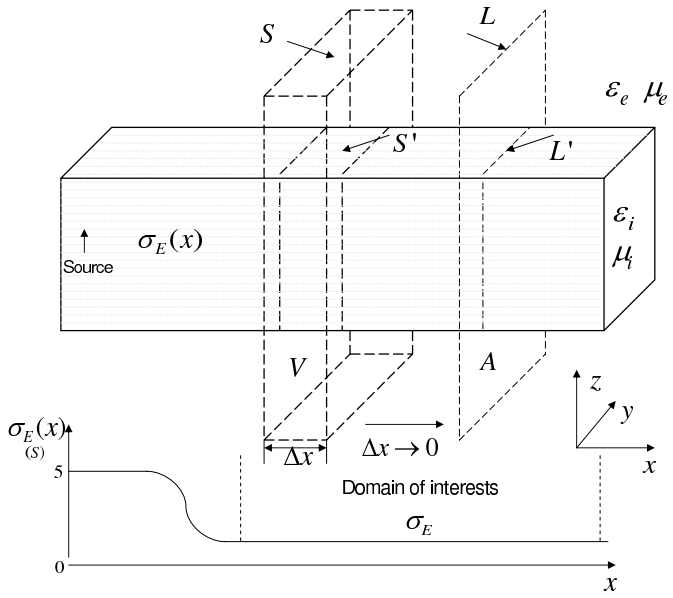

Figure 4-12: Illustration of the approach using Poynting's theorem to calculate the decay rate of a waveguide with surface conductivity. The plot of the surface conductivity distribution $\sigma_E(x)$ along the longitudinal direction is aligned with the waveguide.

4.4.2 Decay rate calculation using Poynting's theorem

The perturbation method above predicts the decay rate when the surface conductivity is small. An alternative approach, based on Poynting's theorem, can be used to calculate the decay rate for the entire σ_E range.

Figure 4-12 shows a waveguide with surface conductivity as well as a plot of the conductivity function $\sigma_E(x)$ with x-axis aligned with the x-axis of the waveguide. Since this approach requires integrating the fields of source-excited propagating modes in the exterior region, some inevitably excited modes, such as radiation modes that will be discussed in section 4.6, must be suppressed. For this reason, the surface conductivity starts with a large constant value (5 S). The large surface conductivity leads to the saturation as seen in Fig. 4-11, and therefore, the Gaussian-beam source excites metallic waveguide modes at the beginning, propagating in $+\hat{x}$ direction in the closed interior region. The surface conductivity is then smoothly reduced to a smaller value, with which the decay rate is to be calculated. In this way, the metallic waveguide modes can smoothly change to the desired decaying dielectric waveguide

modes with minimal radiation modes excited.

The decaying propagating mode in the domain of interest, shown in Fig. 4-12, is assumed in the form

$$\mathbf{E}(\mathbf{r}) \sim \mathbf{E_0}(y,z)e^{-\alpha x - j\beta x}, \tag{4.38}$$

$$\mathbf{H}(\mathbf{r}) \sim \mathbf{H_0}(y,z)e^{-\alpha x - j\beta x}, \tag{4.39}$$

where β is the real propagation constant, and α is the unknown decay rate. The Poynting vector in frequency domain is given by $\mathbf{S} = \frac{1}{2}\mathbf{E} \times \mathbf{H}^*$, and together with the assumed forms of $\mathbf{E}$ in (4.38) and $\mathbf{H}$ in (4.39), the derivative with respect to x is given by

$$\frac{d\mathbf{S}}{dx} = -2\alpha\mathbf{S}. \tag{4.40}$$

As illustrated in Fig. 4-12, apply Poynting's theorem in the closed volume V

$$\mathrm{Re}\int_S \mathbf{S}\cdot\hat{n}dS = -\frac{1}{2}\int_{S'}\sigma_E|\mathbf{E}_{\tan}|^2 dS', \tag{4.41}$$

where S is the surface of the volume V, $\hat{n}$ is an exterior-directed normal unit-vector, and S' is the waveguide surface within V. In the limit as $\Delta x \to 0$, the closed integration surface S becomes a surface A, and one component of the integrand of the left side of (4.41) becomes $\frac{d\mathbf{S}}{dx}\cdot\hat{x}$. Combining (4.40) and this $\Delta x \to 0$ limit of (4.41) yields a closed-form representation of the decay rate α

$$\alpha = \frac{\int_{L'}\sigma_E|\mathbf{E}_{\tan}|^2 dl' + \mathrm{Re}\int_L(\mathbf{E}\times\mathbf{H}^*)\cdot\hat{n}dl}{2Re\int_A(\mathbf{E}\times\mathbf{H}^*)\cdot\hat{x}dS}, \tag{4.42}$$

where L denotes the boundary of the surface A, and L' denotes the integral line on the waveguide surface within the surface A.

The decay rate calculated using (4.42) is plotted in Fig. 4-11 with a dashed circle curve. It shows good agreement with the decay rate computed using fitting for the entire σ_E range, verifying that the surface conductivity is handled correctly by the BEM in accordance with Maxwell's equations.

4.5 Asymptotic Convergence of Transition Reflections

In section 4.3, we showed that a smoothly varying surface conductive absorber easily implemented in the SIE method is orders of magnitude more effective at eliminating reflections than a volume absorber of comparable length. And, since computational cost increases with the length of the absorber, it is worth examining the relationship between reflections and the absorber length. In order to do this, we first require a more sensitive numerical measure of reflections than the standing wave ratio method. In the following subsections, we will present a measure of the power-law asymptotic convergence of transition reflections.

In Sec. 2.1, reflections in a domain of interest can be divided into a round-trip reflection, R_r, and a transition reflection, R_t. Here, the surface conductivity function is a dth order monomial function as defined in (2.3). The round-trip reflection R_r can be fixed by making the conductivity coefficient inversely proportional to the absorber length L. Therefore, using a longer absorber implies a smaller transition reflection. It was further shown in Sec. 2.1 that, given a fixed round-trip reflection, the transition reflection decreased as a power law with increasing absorber length L. The power-law exponent is determined by the order of the differentiability of the medium (conductivity) function. Moreover, with the surface conductivity function $\sigma_E(x)$ as defined in (2.3) and a fixed round-trip reflection, the asymptotic behavior of the transition reflection in terms of the length of the absorber is

$$R_t(L) \sim \frac{1}{L^{2d+2}}. \tag{4.43}$$

We present numerical results to verify the asymptotic power-law convergence of the transition reflection of the surface absorber. Because it is hard to explicitly measure the transition reflection in the integral equation method, instead, we measure alternative electric field expressions as in [24].

First, we define $\mathbf{E}(L)$ as the electric field at a fixed position in the waveguide

when the length of the absorber is L, with unit λ_i. Thus $\mathbf{E}(L)$ includes the incident field, the round-trip reflection and the transition reflection. With a small fixed round-trip reflection, the difference of $\mathbf{E}(L+1)$ and $\mathbf{E}(L)$ is the difference of the transition reflections, which in the limit of large L approaches to zero, so $\mathbf{E}(L+1)-\mathbf{E}(L) \to 0$. Therefore, $|\mathbf{E}(L+1)-\mathbf{E}(L)|$, and similarly $|\mathbf{E}(2L)-\mathbf{E}(L)|$, can be a measure of transition reflection, and specifically, derived from (4.43), they are subject to the following asymptotic behavior

$$\frac{|\mathbf{E}(L+1)-\mathbf{E}(L)|^2}{|\mathbf{E}(L)|^2} \sim \frac{1}{L^{2d+4}}, \tag{4.44}$$

$$\frac{|\mathbf{E}(2L)-\mathbf{E}(L)|^2}{|\mathbf{E}(L)|^2} \sim \frac{1}{L^{2d+2}}. \tag{4.45}$$

In the example of a rectangular waveguide attached with a surface absorber, the asymptotic convergence of (4.44) is shown in Fig. 4-13(a) in a log-log scale for constant, linear, quadratic, and cubic surface conductivity profiles ($d = 0, 1, 2, 3$). The curve for $d = 0$ slowly approaches to the L^{-4} curve. The other three curves align with the expected L^{-6}, L^{-8}, L^{-10} curves respectively. The curves would eventually converge to a small quantity, which is the difference of the small round-trip reflections due to a phase difference. Fig. 4-13(b) shows the asymptotic convergence of (4.45) with the same waveguide example for constant, linear, quadratic, and cubic profile surface conductivities. Again, the curve for the constant conductivity profile converges slowly, and is expected to be aligned with the L^{-2} curve. The other three power-law convergence are the same as the predicted L^{-4}, L^{-6}, L^{-8}. The agreement of the figures verifies the power-law behavior of the transition reflection of the surface absorber and further illustrates that a higher-order conductivity function leads to smaller transition reflections.

4.6 Radiation in the surface absorber

A surface absorber with a conductivity that rises smoothly with distance from the waveguide-absorber interface would be expected to have interior fields whose mag-

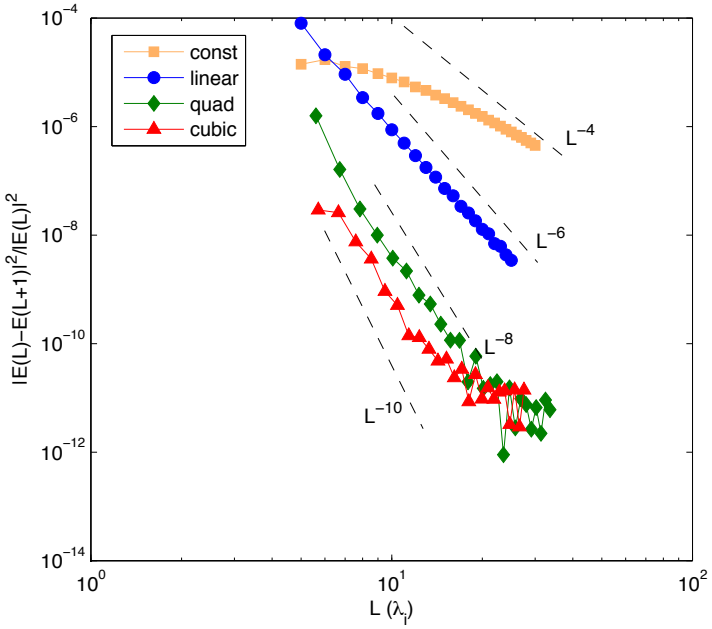

(a) The asymptotic convergence of the transition reflection measured using $\frac{|\mathbf{E}(L+1)-\mathbf{E}(L)|^2}{|\mathbf{E}(L)|^2}$.

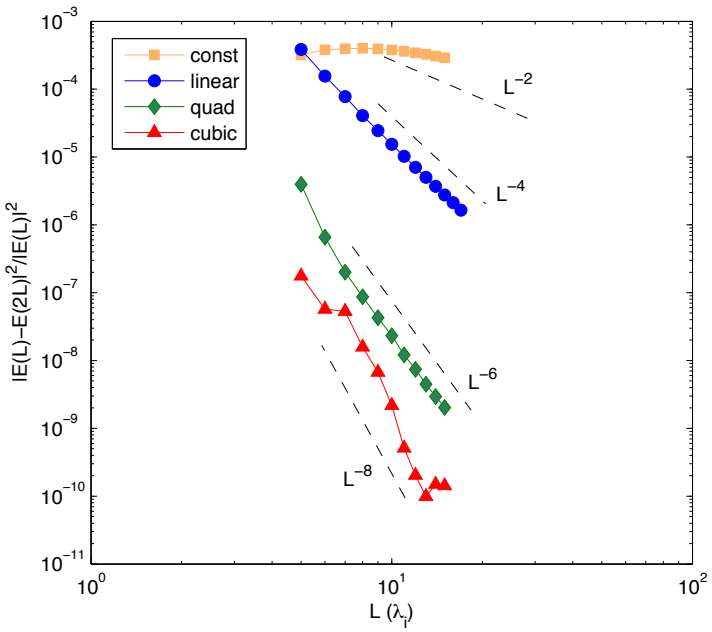

(b) The asymptotic convergence of the transition reflection measured using $\frac{|\mathbf{E}(2L)-\mathbf{E}(L)|^2}{|\mathbf{E}(L)|^2}$.

Figure 4-13: Asymptotic power-law convergence of the transition reflection with the length of the surface absorber. The length of the waveguide is $10\lambda_i$, with λ_i denoting the wavelength in the waveguide medium. The waveguide cross section size is $0.7211\lambda_i \times 0.7211\lambda_i$. The relative permittivities of the waveguide (silicon) and the external medium (air) are 11.9 and 1, respectively.

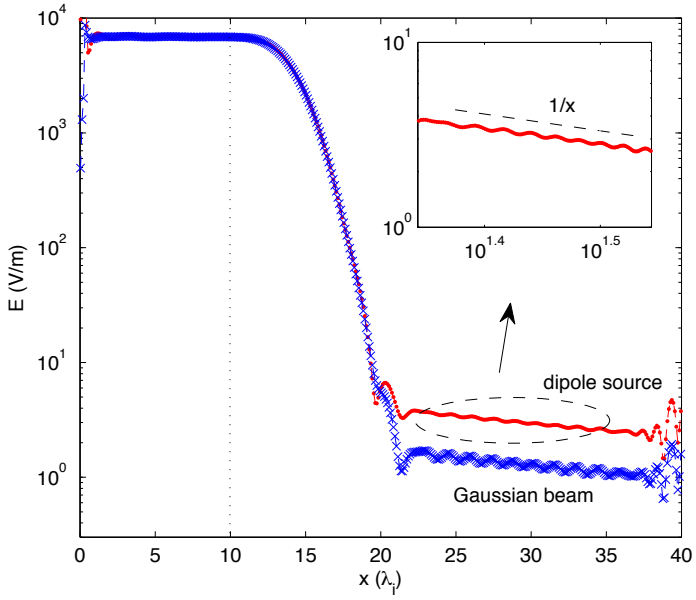

Figure 4-14: The complex magnitude of the electric field inside a waveguide and a long surface absorber excited by a dipole source and a Gaussian beam, respectively. The lengths of the waveguide and the absorber are $10\lambda_i$ and $30\lambda_i$, respectively. The surface conductivity on the absorber increases quadratically.

nitude decays with distance at an accelerating exponential rate. Instead, the field magnitudes decay exponentially near the interface, but then switch to an $\frac{1}{r}$ decay, as shown in Fig. 4-14. The cause of this switch in decay rate is due to coupled radiation. The radiation is generated by the inevitable mismatch between the excitation source and waveguide modes. The situation is similar to a source radiating in a lossy half-space, in which the dominant field contribution is due to a lateral wave that decays algebraically [69, 70]. Fig. 4-14 shows the complex magnitude of the interior electric field in a waveguide attached with a long quadratic-profile surface absorber. The waveguide system is excited by a dipole source and a Gaussian beam, respectively, located inside the waveguide. In the semilog plot, the dominant waveguide mode decays at an accelerating exponential rate, and then because the guided mode decays faster than the $\frac{1}{r}$ radiation, the radiation dominates at a certain distance from the waveguide-absorber interface. The coupled radiation results in an $\frac{1}{r}$ floor, as is clearly shown in the inset with a log-log scale. Note that using a Gaussian beam

source results in a lower floor than using a dipole source, because the Gaussian beam is more directional, and generates less radiation.

The coupled $\frac{1}{r}$ radiation does not affect the performance of the surface absorber, because the coupled radiation itself is several orders of magnitude smaller than the propagating modes in the waveguide, and little will be reflected. The asymptotic convergence of the transition reflections in section 4.5 and the -79.7dB reflection coefficient in section 4.3 consistently showed the excellent performance of surface absorbers, obviously unhampered by the effects of radiation.

4.7 Electrical and Magnetic Surface Conductivities

Up to now, we have investigated the surface absorber with electrical surface conductivity both theoretically and experimentally. In Sec. 4.4, we have shown that large electrical surface conductivity leads to a saturation phenomenon as the large surface conductivity turns the dielectric waveguide into a metallic waveguide, making propagating waves stop attenuating. But this phenomenon does not cause problems for the surface absorber because Sec. 4.5 has shown that the surface absorber in general operates at the small surface conductivity regime to reduce transition reflectons. However, it would be nice if we could figure out ways to eliminate the saturation phenomenon, and leave the large surface conductivity an option in future to apply to surface absorbers. Another way to consider the saturation phenomenon is the impedance match between the interior region and the surface conductivity region (though the thickness of the surface conductivity region is in the limit to 0) in the cross section plane (yz plane in Fig. 4-12).

Consider the normal-incident wave from the interior region to the surface conductivity region in the yz plane, whose reflection is determined by the mismatch of the intrinsic impedance of the two regions. The intrinsic impedance of the interior region is $Z_i = \sqrt{\frac{\mu_i}{\epsilon_i}}$, where ϵ_i and μ_i are the permittivity and permeability of the

interior material, respectively. The impedance of the surface conductivity region is $Z_{\text{surf}} = \sqrt{\frac{\mu_i}{\epsilon_i - j\frac{\sigma_E}{\omega}}}$. When σ_E increases from zero, the impedances of the two regions start to mismatch, making some of the incident waves reflected back to the interior region without being dissipated in the conductivity region. When σ_E goes to infinity, the impedance completely mismatches and all waves are reflected. With the electrical surface conductivity only, it is difficult to match the impedance when σ_E is nonzero. Therefore, in this section, we propose use both the electrical and magnetic surface conductivities σ_E and σ_M, and the impedance of the surface conductivity region becomes

$$Z_{\text{surf}} = \sqrt{\frac{\mu_i - j\frac{\sigma_M}{\omega}}{\epsilon_i - j\frac{\sigma_E}{\omega}}}. \tag{4.46}$$

Given a fixed ratio of the surface conductivities $\frac{\sigma_M}{\sigma_E} = \frac{\mu_i}{\epsilon_i}$, the impedances of the interior region and the conductivity region are matched with increasing the conductivities, and the normal incidence could completely penetrate into the surface conductivity region and be dissipated. For this reason, even if the surface conductivities σ_E and σ_M are large, there are at least the normal incidence (probably some obliquely incidence) which could be eliminated as the wave propagates down the waveguide, and the decay rate should increase with the conductivities. In this way, we expect to eliminate the saturation phenomenon.

However, the next sections will describe the difficulties to generate accurate BEM formulations to incorporate both the electrical and magnetic surface conductivities. Instead, we use an alternative approximate formulation to model a waveguide with both the surface conductivities. The numerical experiments will show that the approximation leads to another saturation phenomenon. The difference is that the decay rate does not decrease to zero as the conductivities approach to infinity, but converges to a constant small value. This demonstrates that the idea of the impedance match partially works with the approximated formulation.

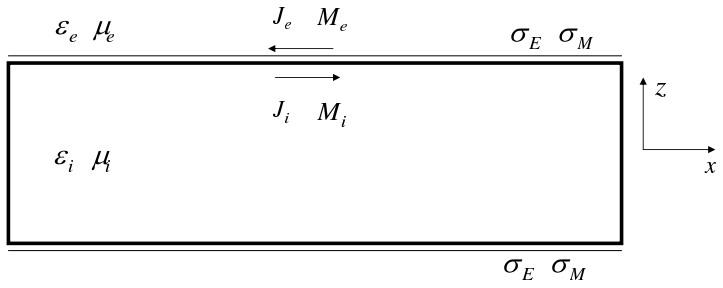

Figure 4-15: The 2-D longitudinal section of a waveguide with uniform electrical and magnetic surface conductivities σ_E and σ_M. The surface conductivities satisfy $\sigma_M = \sqrt{\frac{\mu_i}{\epsilon_i}}\sigma_E$. The waveguide length is $8\lambda_i$ and the cross section size is $0.7211\lambda_i \times 0.7211\lambda_i$. The relative permittivities of the waveguide and external medium are 11.9 and 1, respectively.

4.7.1 BEM Formulations

In this section, we use the boundary element method to analyze a waveguide with both electrical and magnetic surface conductivities. Fig. 4-15 shows the longitudinal cross section of the waveguide in xz plane, and $+x$ is the propagation direction. The permittivity and permeability of the exterior region and interior region are denoted by, ϵ_e, μ_e and ϵ_i, μ_i, respectively. The electrical and magnetic surface conductivities are denoted by σ_E and σ_M, respectively, and their ratio is fixed by $\frac{\sigma_M}{\sigma_E} = \frac{\mu_i}{\epsilon_i}$.

Similarly as in Sec. 4.1, the unknowns of the boundary element method are the equivalent electrical and magnetic currents $\mathbf{J}_e$, $\mathbf{M}_e$ on the exterior side of the surface and $\mathbf{J}_i$, $\mathbf{M}_i$ on the interior side of the surface. However, the existence of both σ_E and σ_M induces both electrical and magnetic currents on the surface as $J_{\text{ind}} = \sigma_E \mathbf{E}_{\tan}$ and $M_{\text{ind}} = \sigma_M \mathbf{H}_{\tan}$, and leads to a different boundary condiction, specifically,

$$-\hat{n} \times [\mathbf{E}_e(\mathbf{J}_e, \mathbf{M}_e) - \mathbf{E}_i(\mathbf{J}_i, \mathbf{M}_i) - \mathbf{E}_{\text{inc}}] = \sigma_M \mathbf{H}_{\tan}, \quad (4.47)$$

$$\hat{n} \times [\mathbf{H}_e(\mathbf{J}_e, \mathbf{M}_e) - \mathbf{H}_i(\mathbf{J}_i, \mathbf{M}_i) - \mathbf{H}_{\text{inc}}] = \sigma_E \mathbf{E}_{\tan}, \quad (4.48)$$

where $\mathbf{E}_{\text{inc}}$ and $\mathbf{E}_{\text{inc}}$ are the incident electric and magnetic fields of the Gaussian beam generated by a dipole in a complex space [64], $\mathbf{E}_{\tan}$ and $\mathbf{H}_{\tan}$ are the tangential electric and magnetic fields on the surface, and $\hat{n}$ denotes the exterior-pointed normal

unit vector. In the boundary conditions in (4.9)–(4.10) in Sec. 4.1, only the magnetic field has a jump and the tangential electric field is continuous across the boundary. Therefore, $\mathbf{E}_{\tan}$ in (4.10) is well defined on the surface and can be represented by the exterior tangential electric field operator or the interior tangential field operator or any linear combination of the two operators. In the boundary conditions (4.47)–(4.48) here, both the tangential electric and magnetic fields have a jump across the surface. The jump in the tangential fields makes a discontinuity at the surface and raises difficulty to exactly represent $\mathbf{E}_{\tan}$ and $\mathbf{H}_{\tan}$ using integral operators due to the equivalent currents. A straightforward compromise is taking an average of the tangential fields on the two side of the boundary, and they are

$$\mathbf{E}_{\tan} = -\frac{1}{2}\hat{n}\times\hat{n}\times[\mathbf{E}_e(\mathbf{J}_e,\mathbf{M}_e)+\mathbf{E}_i(\mathbf{J}_i,\mathbf{M}_i)+\mathbf{E}_{\text{inc}}], \tag{4.49}$$

$$\mathbf{H}_{\tan} = -\frac{1}{2}\hat{n}\times\hat{n}\times[\mathbf{H}_e(\mathbf{J}_e,\mathbf{M}_e)+\mathbf{H}_i(\mathbf{J}_i,\mathbf{M}_i)+\mathbf{H}_{\text{inc}}]. \tag{4.50}$$

The validity of this approximation for $\mathbf{E}_{\tan}$ and $\mathbf{H}_{\tan}$ will be discussed in the next section. Substituting (4.49)–(4.50) into (4.47)–(4.48) yields

$$\hat{n}\times\left[-\mathbf{E}_e(\mathbf{J}_e,\mathbf{M}_e)+\mathbf{E}_i(\mathbf{J}_i,\mathbf{M}_i)+\frac{1}{2}\sigma_M\hat{n}\times[\mathbf{H}_e(\mathbf{J}_e,\mathbf{M}_e)+\mathbf{H}_i(\mathbf{J}_i,\mathbf{M}_i)]\right] = -\hat{n}\times[\mathbf{E}_{\text{inc}}+\frac{1}{2}\sigma_M\hat{n}\times\mathbf{H}_{\text{inc}}], \tag{4.51}$$

$$\hat{n}\times\left[\mathbf{H}_e(\mathbf{J}_e,\mathbf{M}_e)-\mathbf{H}_i(\mathbf{J}_i,\mathbf{M}_i)+\frac{1}{2}\sigma_E\hat{n}\times[\mathbf{E}_e(\mathbf{J}_e,\mathbf{M}_e)+\mathbf{E}_i(\mathbf{J}_i,\mathbf{M}_i)]\right] = \hat{n}\times[\mathbf{H}_{\text{inc}}-\frac{1}{2}\sigma_E\hat{n}\times\mathbf{E}_{\text{inc}}]. \tag{4.52}$$

To reduce computational costs, the type II formulation is employed for fewer unknowns. The equivalent currents are therefore reduced to $\mathbf{J}$ and $\mathbf{M}$ in the way of

$$\mathbf{J}_e = -\mathbf{J}_i = \mathbf{J}, \tag{4.53}$$

$$\mathbf{M}_e = -\mathbf{M}_i = \mathbf{M}. \tag{4.54}$$

Substituting (4.53)–(4.54) into (4.51–4.52) yields the final version of the type II BEM

formulations with two sets of unknown currents **J** and **M** for the waveguide (or absorber) with both electrical and magnetic surface conductivities. In order to solve the equations, the unknown currents are approximated using the RWG basis functions on discretized triangle panels of the surface [1]. The equations are then discretized, and a system matrix is constructed and solved using an iterative method as discussed in Sec. 4.2.

4.7.2 Numerical Results and Analysis

A waveguide with uniform electrical and magnetic surface conductivities is analyzed using the boundary element method described in Sec. 4.7.1. The xz–plane cross section of the waveguide is shown in Fig. 4-15. The relative permittivities of the waveguide (silicon) and the external medium (air) are 11.9 and 1, respectively. The relative permeability of both the media are 1. The electrical and magnetic surface conductivities are fixed with the ratio $\frac{\sigma_M}{\sigma_E} = \frac{\mu_i}{\epsilon_i}$. The waveguide cross-section size is $0.7211\lambda_i \times 0.7211\lambda_i$, where λ_i is the wavelength in the interior region. The length of the waveguide is $8\lambda_i$.

The complex magnitudes of the electric fields along the central axis of the waveguide are plotted in Fig. 4-16, when σ_E is equal to 0.001S, 0.005S and 0.5S. The field exponentially decays at a fixed rate for each σ_E along the waveguide, reflects back at the end of the waveguide, and continues being dissipated on the way propagating backwards. On the field curve for $\sigma_E = 0.005$S, the radiation wave as described in Sec. 4.6 shows up because the propagating wave decays fast and becomes smaller than the inevitably excited radiation wave. Note that the decay rate increases from $\sigma_E = 0.001$S to $\sigma_E = 0.001$S, but it decreases for $\sigma_E = 0.5$S. This implies that the decay rate does not monotonically increase with the surface conductivities as we expected by the impedance match with the fixed-ratio pair of σ_E and σ_M.

We further show the decay rate versus the electrical surface conductivity σ_E in Fig. 4-17. Obviously, it still has the saturation phenomenon. But the decay-rate curve is different from the one with the electrical surface conductivity only in Fig. 4-11. In Fig. 4-11, the decay rate increases to a maximum value and then monotonically de-

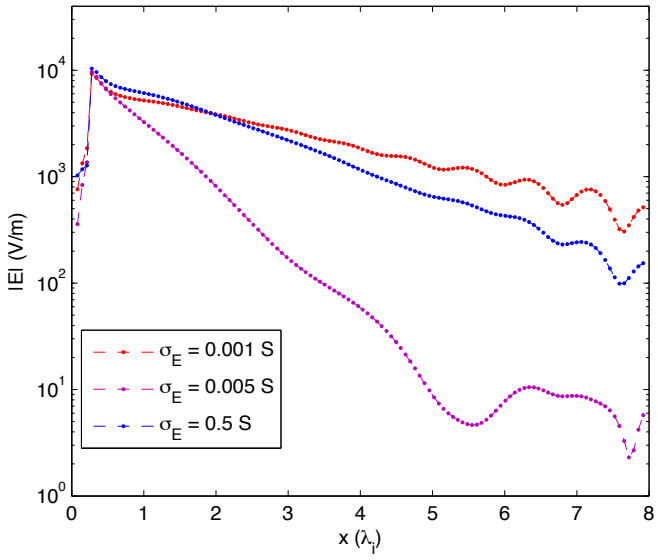

Figure 4-16: The complex magnitude of the electric field along the central axis inside a waveguide with electrical and magnetic surface conductivities σ_E and σ_M, respectively. The surface conductivities satisfies $\sigma_M = \frac{\mu_i}{\epsilon_i}\sigma_E$. The length of the waveguide is $8\lambda_i$.

creases with increasing σ_E. However, in Fig. 4-17, after reaching the maximum decay rate, the decay rate decreases and then converges to a constant value. This partially demonstrates that the match of impedance does dissipate power for large σ_E and σ_M. Nevertheless, it does not increase with the surface conductivities monotonically, which suggests that the approximation of the tangential fields using the average of the fields at the two side of the boundary in (4.49)–(4.50) becomes inaccurate for large surface conductivities.

We demonstrate the inaccuracy by deriving the boundary condition using a 1-D example in the z direction shown in Fig. 4-18. For simplicity, the permittivities and permeabilities are the same for the three regions, denoted by ϵ and μ in Fig. 4-18. Region 2 is the region with electrical and magnetic conductivities, and the width of region 2 is denoted by Δz. We denote the homogeneous electrical conductivity by $\sigma_{E,\Delta z} = \sigma_E/\Delta z$, parameterized by the width of region 2, and the ratio of the conductivities is always fixed by $\frac{\sigma_{M,\Delta z}}{\sigma_{E,\Delta z}} = \frac{\mu}{\epsilon}$. Taking a limit of $\Delta z \to 0$, region 2 becomes the boundary of region 1 and region 3, the electrical conductivity becomes

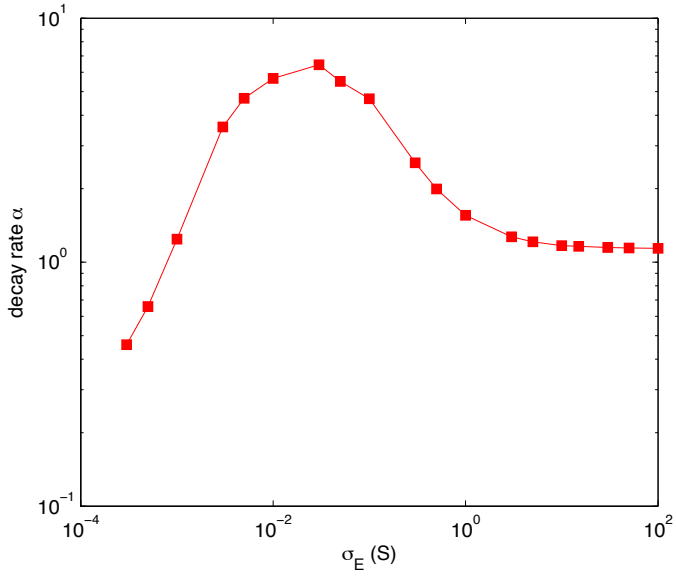

Figure 4-17: The numerically measured decay rate due to the electrical and magnetic surface conductivities versus the electrical surface conductivity. The magnetic surface conductivity scales proportional to the electrical surface conductivity, specifically, $\sigma_M = \frac{\mu_i}{\epsilon_i}\sigma_E$.

$\sigma_{E,\Delta z} = \sigma_E \delta(z)$, known as the surface conductivity, and the relation of the fields at the two sides of region 1 becomes the boundary conditions of region 1 and region 3.

Consider a TM mode plane wave with normal incidence in the z direction in region 1. Because the intrinsic impedance are matched at the interface of the three regions, the normal-incident fields can completely penetrate the interfaces without reflections. We denote the incident electric and magnetic fields at the left boundary of region 2 as $\mathbf{E}_1 = E_0\hat{\mathbf{y}}$ and $\mathbf{H}_1 = -H_0\hat{\mathbf{x}}$, and $E_0 = \sqrt{\frac{\mu}{\epsilon}}H_0$. The effective permittivity and permeability of region 2 are complex, and are denoted by $\epsilon_{\text{eff}} = \epsilon - j\frac{\sigma_{E,\Delta z}}{\omega}$ and $\mu_{\text{eff}} = \mu - j\frac{\sigma_{M,\Delta z}}{\omega}$. Therefore, the propagation constant in region 2 is

$$k = \omega\sqrt{\mu_{\text{eff}}\epsilon_{\text{eff}}} = \omega\sqrt{\mu\epsilon} - j\sqrt{\frac{\mu}{\epsilon}}\sigma_{E,\Delta z} = \beta - j\alpha, \tag{4.55}$$

where the real part is the real propagation constant, and the negative imaginary part is the decay constant $\alpha = \sqrt{\frac{\mu}{\epsilon}}\sigma_{E,\Delta z} = \sqrt{\frac{\mu}{\epsilon}}\frac{\sigma_E}{\Delta z}$ due to the electrical and magnetic conductivities. With the complex propagation constant k in region 2, the electric

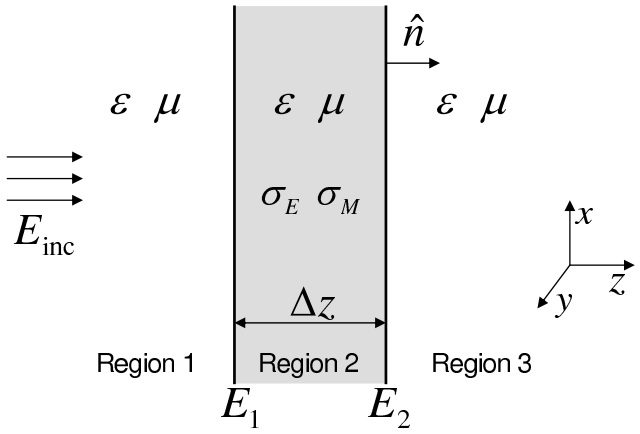

Figure 4-18: The geometry of a 1-D layered media in the z direction. The permittivities and permeabilities of the three region are identical, and denoted by ϵ and μ. The width of region 2 is denoted by Δz.

field at the right boundary of region 2 can be calculated by

$$\mathbf{E}_2 = E_0 e^{-\alpha\Delta z} e^{-j\beta\Delta z}\hat{\mathbf{y}} = E_0 e^{-\sqrt{\frac{\mu}{\epsilon}}\sigma_E} e^{-j\beta\Delta z}\hat{\mathbf{y}}. \tag{4.56}$$

Take a limit of $\Delta z \to 0$ as region 2 shrinks to be a surface, the electric field in (4.56) becomes $\mathbf{E}_2 = E_0 e^{-\sqrt{\frac{\mu}{\epsilon}}\sigma_E}\hat{\mathbf{y}}$. The boundary condition of the electrical field between region 1 and region 3 is

$$-\hat{\mathbf{z}} \times (\mathbf{E}_2 - \mathbf{E}_1) = E_0(e^{-\sqrt{\frac{\mu}{\epsilon}}\sigma_E} - 1)\hat{\mathbf{x}}. \tag{4.57}$$

This is the boundary condition for the whole range of conductivities for the normal incident TM wave, and different with the boundary condition in (4.51) in the BEM formulation. However, for small σ_E, the first-order approximation of (4.57) is

$$-\hat{\mathbf{z}} \times (\mathbf{E}_2 - \mathbf{E}_1) = -\sigma_E\sqrt{\frac{\mu}{\epsilon}}E_0\hat{\mathbf{x}} = \sigma_M\mathbf{H}_1. \tag{4.58}$$

This electrical field boundary condition in (4.58) is same as the boundary condition (4.51) used in the BEM, since $\mathbf{H}_1 \sim (\mathbf{H}_1 + \mathbf{H}_2)/2$ in the limit of small σ_E and σ_M. Similarly, the magnetic field boundary condition for small conductivities can be

derived, and it is

$$\hat{\mathbf{z}} \times (\mathbf{H}_2 - \mathbf{H}_1) = \sigma_E \mathbf{E}_1, \tag{4.59}$$

which is same as (4.52) in the BEM formulation.

As shown above, the BEM formulation in Sec. 4.7.1 is accurate only for small surface conductivities. The accurate representation of the jump in the tangential fields for large conductivities in the limit of $\Delta z \to 0$ is complicated, and (4.57) only shows the boundary condition for a simplified case (normal incidence in the identical exterior and interior regions). The derivation for the exact boundary conditions is out of the scope of this thesis. This section describes one approximate BEM formulation and it improves the saturation phenomenon by having the decay rate converging to a small value for large conductivities rather than converging to zero.

Chapter 5

Terminating Periodic Channels with Surface Absorbers

Truncating dielectric channels with a surface conductive absorber has been demonstrated to be an effective technique for simulating uniform cross-section waveguides with the boundary element method in Chapter 4. In this chapter, we examine the properties of a surface conductive absorber used to terminate infinitely long periodic channels, common in photonic applications. Unlike uniform channels, the periodic channel can be excited at a band-gap edge, where the group velocity is close to zero, resulting in a large transition reflection at the waveguide-absorber interface. We show that a surface absorber that can perform well when the waveguide system is excited with a large group-velocity mode may fail when excited with a smaller group-velocity mode, and give an asymptotic relation between the surface absorber length, transition reflections and group velocity. Numerical results are given to validate the asymptotic prediction.

5.1 Terminating A Sinusoidal-Shape Waveguide

Figure. 5-1 shows a 3-D waveguide with period-a sinusoidally corrugated sidewalls (sine waveguide) terminated by a surface conductive absorber of the same shape. The longitudinal cross section in the x–y-plane of the truncated sine waveguide is

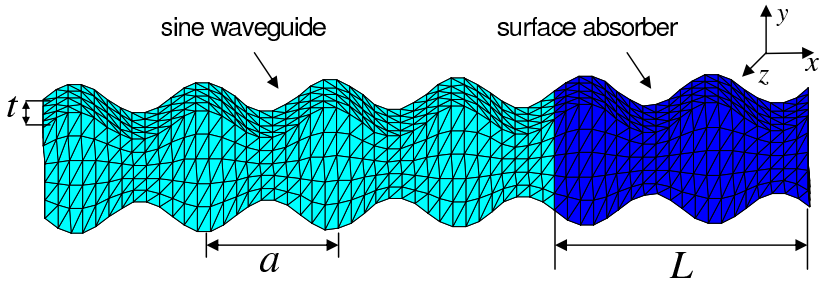

Figure 5-1: A 3-D discretized sine waveguide with a surface absorber attached. The period of the waveguide is denoted by a, the length of the absorber is denoted by L, and t denotes the thickness in the z direction. The relative permittivities of the waveguide and the exterior media are 11.9 and 1, respectively.

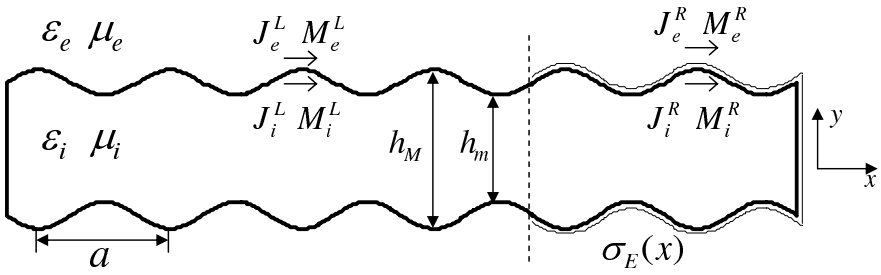

Figure 5-2: The 2-D longitudinal section of a sine waveguide with a surface absorber attached. The period of the sine waveguide and absorber is a. The maximum and minimum sizes in the y direction are denoted by h_M and h_m, respectively. The dashed line indicates the interface of the waveguide and absorber. The surface conductivity on the absorber is denoted by $\sigma_E(r)$.

shown in Fig. 5-2, where the dashed line indicates the position of the waveguide-absorber interface. The surface absorber remains the same sinusoidal shape as the waveguide in order that the gradual change in the absorptivity be the only violation of discrete translational symmetry.

The permittivity and permeability of the sine waveguide interior and the exterior are, respectively, denoted by ϵ_e, μ_e and ϵ_i, μ_i, where the subscripts e and i denote the exterior and the interior. The period of the sine waveguide is a. The thickness in the z direction is t. The maximum and minimum widths in the y direction are denoted by h_M and h_m, respectively, so that the width is $(h_M+h_m)/2+\sin(2\pi x/a)\cdot(h_M-h_m)/2$. The length of the absorber is L. The electrical surface conductivity is a Dirac delta function across the absorber surface, and its magnitude is denoted as $\sigma_E(\mathbf{r})$, with the

subscript E as a reminder that only electrical conductivity is being considered. The system is excited by a Gaussian beam propagating in $+\hat{x}$ direction. The Gaussian beam is generated by a dipole in a complex space (see Appendix A), and the real part of the dipole position is inside the waveguide, $\frac{1}{4}\lambda_i$ from the left end.

The sine waveguide and its surface absorber can be analyzed using the boundary element method with either type I or type II formulations in Sec.4.1. The unknowns of the BEM are the equivalent electrical and magnetic currents $\mathbf{J}_e^L$, $\mathbf{M}_e^L$, $\mathbf{J}_i^L$, and $\mathbf{M}_i^L$ on the exterior and interior sides of the waveguide surface and $\mathbf{J}_e^R$, $\mathbf{M}_e^R$, $\mathbf{J}_i^R$, and $\mathbf{M}_i^R$ on the exterior and interior sides of the absorber surface. The subscripts e and i indicate the exterior and interior sides of the surface where the currents are lying, and the superscripts L and R are a reminder of the region to the left of waveguide-absorber interface and the region to the right of the interface, respectively. The unknowns are approximated with the RWG function on discretized triangle pairs [1], and the RWG coefficients are determined by solving a linear system with boundary conditions enforced on the surfaces as shown in Sec. sec:appendix..

In this chapter, we use a dth-order monomial function for the surface conductivity $\sigma_E(\mathbf{r})$ along the x-axis of the absorber, specifically,

$$\sigma_E(\mathbf{r}) = \sigma_0(\frac{x - x_0}{L})^d, \tag{5.1}$$

where x_0 denotes the position of the waveguide-absorber interface. According to Sec.2.1, to fix the round-trip reflection for a single-mode excitation with absorbers of different properties, the conductivity coefficient σ_0 should be set to satisfy

$$\sigma_0 \sim \frac{V_g}{L}(d+1) \tag{5.2}$$

with a proportionality constant determined in part by the mode profile and logarithmic in the desired round-trip reflection. In this chapter, we fix the round-trip reflection to be very small (< -60 dB), so that we can focus on the transition reflections. This is a practical strategy because the transition reflections scale only logarithmically with the round-trip reflection parameter [24].

5.2 Numerical Results

5.2.1 A sine waveguide with a surface absorber attached

In this section, we discuss the numerical results of the sinusoidal-shape waveguide with a surface conductive absorber attached (Fig. 5-1) using the boundary element method. The sizes of the sine waveguide are $h_M = a$, $h_m = 0.5a$ and $t = 0.4a$, where a is the period of the sine waveguide. The relative permittivities of the waveguide and the exterior medium are 11.9 (silicon) and 1 (air), respectively. The relative permeabilities of both the media are 1. The lengths of the waveguide and the absorber are $20a$ and $15a$, respectively. We use a second-order surface conductivity function, specifically, $d = 2$ and $\sigma_0 = 0.006$S in (5.1). We examine the performance of this surface absorber by exciting at two different frequencies (or, equivalently, two different k values) of the lowest band.

First, the waveguide system is excited at $k = 0.304\frac{2\pi}{a}$, far away from the band gap edge, and thus the group velocity $V_g = 0.36c$ is relatively large (compared to the light speed in silicon $c/\sqrt{11.9} \approx 0.29c$). The complex magnitude of the electric field along the center axis of the sine waveguide and absorber is shown in Fig. 5.2.1. The dashed line indicates the position of the waveguide-absorber interface. Note that, close to the excitation source, the propagating mode interacts with inevitably excited radiation and evanescent modes to produce a transient field for $x \leq 10a$. At a greater distance from the source, the waveform becomes periodic with period a, which is consistent with Bloch's theorem for infinitely long periodic structures without reflections. The total reflection can be obtained using a harmonic inversion method to decompose the field into different k components [71, 72], and it is -54.4dB.

Then we excite the sine waveguide and the same surface absorber closer to the band edge, specifically, $k = 0.436\frac{2\pi}{a}$ and $V_g = 0.12c$. Fig. 5-4(a) shows the complex magnitude of the electric field along the waveguide and absorber. The waveform is far from periodic with period a, which implies a large total reflection. By numerical measurement, the total reflection for this excitation is -15.1dB. Note that Fig. 5-4(a) shows a greater absorption, and in turn a smaller round-trip reflection for this small

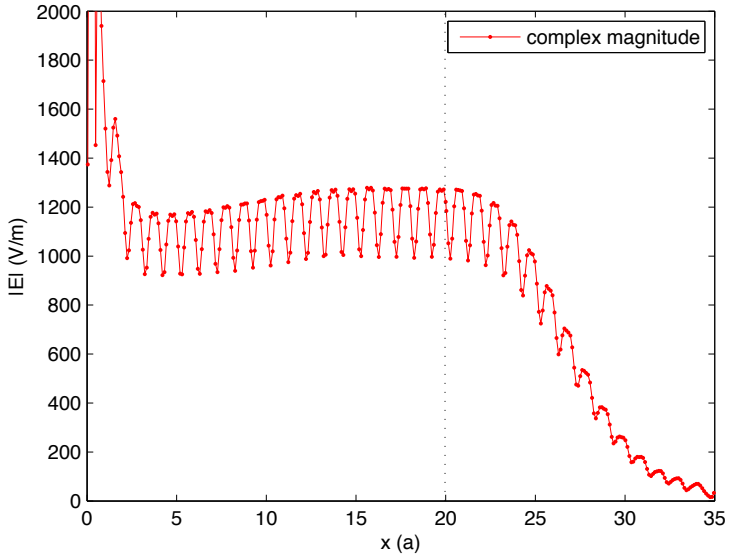

Figure 5-3: The complex magnitude of the electric field along the x-axis of a sine waveguide and a surface absorber, when the waveguide system is excited with $k = 0.304\frac{2\pi}{a}$. The conductivity-function coefficient $\sigma_0 = 0.006$S. The dashed line indicates the position of the waveguide-absorber interface.

group-velocity excitation. This is consistent with the prediction that absorption is proportional to $\frac{\sigma_0}{V_g}$, as mentioned in the last section. The small round-trip reflection indicates that the transition reflection is the dominate contribution to the total reflection.

However, in order for a fair comparison between the two excitations with the same-length absorber, the round-trip reflection should be fixed by reducing σ_0 for the small group-velocity excitation, as in (5.2). The smaller σ_0 will make the material transition at the waveguide-absorber interface smaller and lead to a smaller transition reflection. Fig. 5-4(b) shows the complex magnitude of the electric field when σ_0 is reduced to 0.002S. The numerically measured total reflection is -22.5dB. The transition reflection decreases when σ_0 is reduced, but it is still much larger than the transition reflection of the large group-velocity excitation. This is because the transition reflection increases as a power law in V_g, specifically, as $\sim V_g^{-(2d+4)}$, while it decreases only quadratically with σ_0 [24]. One should make the absorber longer to reduce the transition reflection when excited close to the band gap edge, and this is

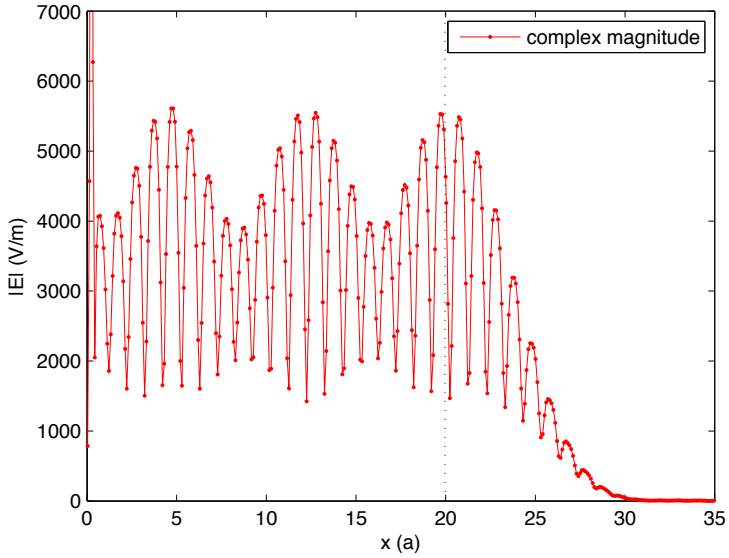

(a) $\sigma_0 = 0.006$S

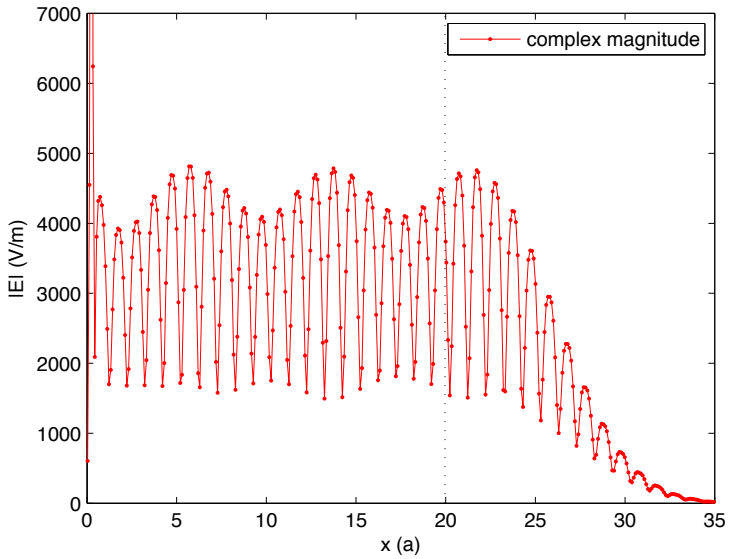

(b) $\sigma_0 = 0.002$S

Figure 5-4: The complex magnitude of the electric field along the x-axis of a sine waveguide and a surface absorber, when the waveguide system is excited with $k = 0.436\frac{2\pi}{a}$. The conductivity-function coefficient is different for each plot.

analyzed in the next section.

5.2.2 The absorber length versus group velocity

As a practical matter, one could repeatedly increase the absorber length L until the reflection decreases to a given tolerance. However, one would like some understanding of how this required L increases with decreasing V_g. In this section, we discuss that question both theoretically and experimentally for two choices of σ_0.

For a single-mode excitation, the round-trip reflection can be fixed by making σ_0 be proportional to $\frac{V_g}{L}$ for different excitations, according to (5.2). In this choice of σ_0, the transition reflection increases as a power law with decreasing absorber length and group velocity, as $R_t \sim L^{-(2d+2)} V_g^{-(2d+2)}$ (Sec. 2.1). In order to obtain same small transition reflection for small group-velocity excitations, the absorber length should be increased as the group velocity decreases, and asymptotically

$$L \sim V_g^{-1} \sim (\frac{\pi}{a} - k)^{-1}, \tag{5.3}$$

where we use $\Delta k = (\frac{\pi}{a} - k)$ to replace V_g because V_g is proportional to Δk [24] close to the band-gap edge and k is easier to obtain numerically. This asymptotic power law is independent of the order d of the conductivity function for this choice of σ_0.

In this example, we increase the absorber length L with V_g^{-1} for three conductivity profiles ($d = 1, 2, 3$) starting from $L = 8$ when $\Delta k = 0.18\frac{2\pi}{a}$ as shown in Fig. 5-5(a). The conductivity function coefficient σ_0 is chosen to be proportional to $\frac{V_g}{L}(d+1)$. Fig. 5-5(b) shows the total reflections for the three profiles as the group velocity decreases. The total reflections are roughly constant for each profile as predicted. The quadratic-profile absorber's reflection is about 10dB smaller than the linear one, while the cubic-profile absorber works no better than the quadratic-profile absorber.

Since increasing d increases the asymptotic rate at which the reflection decreases with L, one might initially conclude that d should be made very large—why not choose $d = 1000$? However, increasing d worsens the *coefficient* of the asymptotic reflection and also delays the onset of the regime in which the asymptotic $1/L^{2d+2}$ power law becomes valid, so for any given L there is some optimal choice of d. This tradeoff can be understood by re-examining the transition reflection coefficient derived

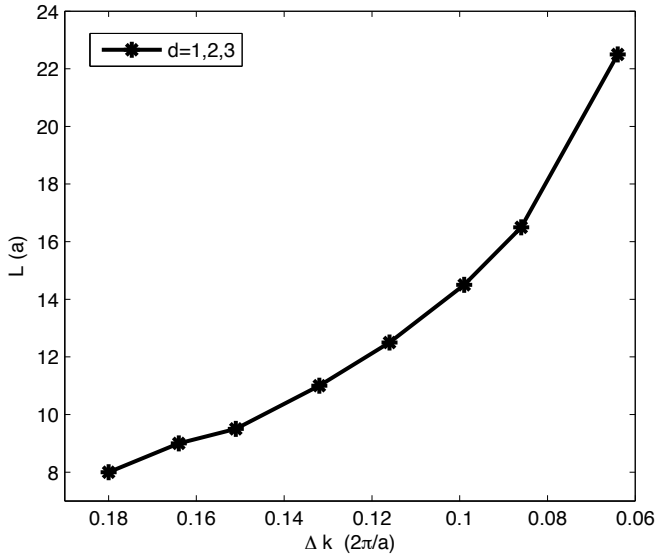

(a) The absorber length L required to obtain the same transition reflection as the group velocities decreases.

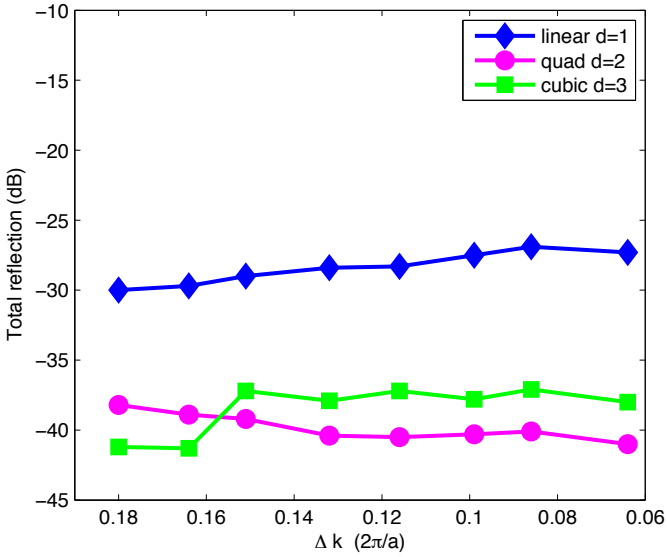

(b) The total reflections generated using the absorber length L in (a) for different group velocities.

Figure 5-5: The required surface absorber lengths and the corresponding total reflections for linear, quadratic and cubic conductivity profiles, as the conductivity linear factor σ_0 is proportional to $\frac{V_g}{L}(d+1)$. The group velocity is substituted with Δk.

using coupled-wave theory in (2.6). Note that in (2.6), $s^{(d)}(0^+) = d!$ if $s(u) = u^d$ defined in $u \in [0, 1]$ and hence the coefficient of the reflection scales as $(d!)^2$, rapidly

worsening the reflection *at a fixed* L as d increases. Furthermore, because the coupled-wave expression itself was only a first-order expansion valid for small reflections [24], increasing d delays the onset of the validity of this asymptotic analysis, since L must be large enough for a term proportional to $d!\sigma_0/L^d$ to be small. This phenomenon is apparent in Fig. 5-6(b), where for this choice of L a cubic profile ($d = 3$) is no better than a quadratic profile ($d = 2$), although for a larger L one would expect the cubic profile to become superior. The effect of different conductivity profiles was studied in more detail in our previous papers [24].

For multiple-mode excitations, the round-trip reflection is different for each mode because of different group velocity. The group velocities of the fastest and slowest mode are denoted by V_{gF} and V_{gS}, respectively. With the fact that a smaller group-velocity mode generates smaller round-trip reflection, the conductivity function coefficient σ_0 should be conservatively chosen for generating small round-trip reflection for the fastest mode and be roughly fixed by making σ_0 be proportional to $\frac{V_{gF}}{L}$. On the other hand, the transition reflection should be determined by the lowest mode, and be proportional to a different power law, $R_t \sim V_{gF}^2 L^{-(2d+2)} V_{gS}^{-(2d+4)}$ (Sec. 2.1). In order to gain same transition reflection, the absorber length would be proportional to

$$L \sim (\frac{V_{gF}}{V_{gS}})^{\frac{1}{d+1}} \frac{1}{V_{gS}}. \tag{5.4}$$

The equation suggests that a higher-order (larger d) conductivity profile asymptotically requires a shorter absorber to obtain the same transition reflection when the group velocity decreases. When $V_{gF} = V_{gS}$, it returns to the asymptotic relation (5.3) for the single-mode excitation.

For simplicity, we demonstrate the relation in (5.4) with a single-mode excitation by making $V_{gF} = 1$, and the conductivity coefficient σ_0 scales to $\frac{d+1}{L}$. Then the required absorber length asymptotically scales to $L \sim V_{gS}^{-\frac{d+2}{d+1}} \sim (\frac{\pi}{a} - k)^{-\frac{d+2}{d+1}}$. Figure 5-6(a) shows the required length of the surface absorber when the group velocity decreases for linear, quadratic and cubic conductivity profiles, respectively. Fig. 5-6(b) shows the corresponding total reflections of the surface absorbers for the three

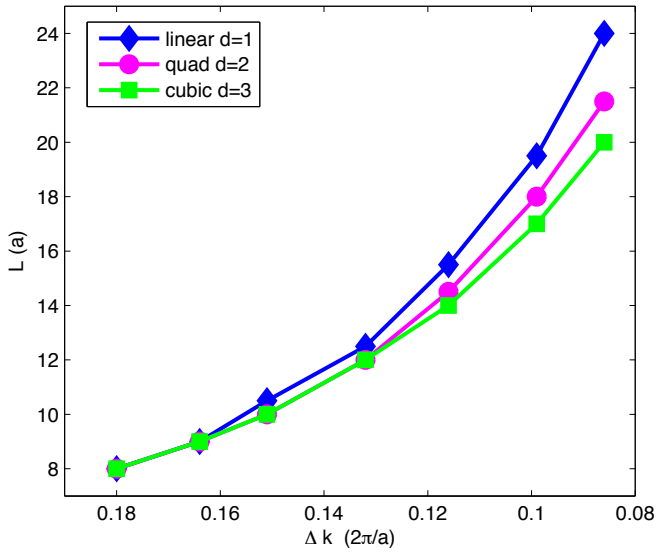

(a) The absorber length L required to obtain the same transition reflection as the group velocities decreases.

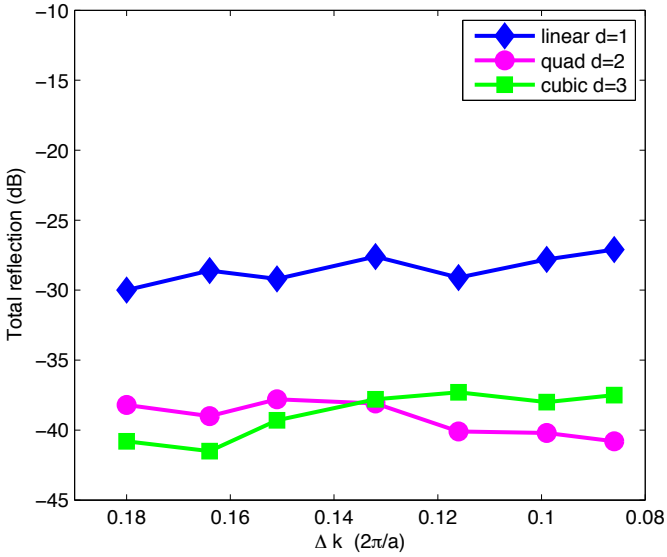

(b) The total reflections generated using the absorber length L in (a) for different group velocities.

Figure 5-6: The required surface absorber lengths and the corresponding total reflections for linear, quadratic and cubic conductivity profiles ($d = 1, 2, 3$), as the conductivity linear factor σ_0 is proportional to $\frac{d+1}{L}$. The group velocity is substituted with Δk.

profiles. Since the round-trip reflections are conservatively fixed by the σ_0 arrangement, the total reflections converge to the transition reflection as the group velocity decreases. As expected, the reflections are roughly fixed irrespective of group velocity for each profile.

As demonstrated by the two examples above with two kinds of σ_0 choices, for small group-velocity excitations, small transition reflections can be achieved by long surface absorbers, and the absorber length is consistent with the theoretical scalings of (5.4) or (5.3).

In this chapter, we described and implemented a surface conductive absorber with the boundary element method to truncate a periodic sinusoidal-shape waveguide. The varying surface conductivity can be easily incorporated into the two types of formulations. We showed that small reflections can be obtained with a short surface absorber when the waveguide is excited with a large group-velocity mode. However, the same-length absorber will generate large reflections if excited with a smaller group-velocity mode. We showed that the length of the absorber is required to increase according to a power law as the group velocity decreases in order to obtain the same transition reflection. This provides guidance for choosing the absorber length with different excitations. Numerical experiments verified our analytical predictions.

Chapter 6

Conclusions

In this thesis, we presented a novel numerical technique, a surface conductive absorber that is easily combined with the boundary element method, to eliminate the reflections due to the truncation of infinite channels. We illustrated this technique with a dielectric optical waveguide and described two types of BEM formulation to allow for varying the surface conductivity. We further discussed the non-monotonically increasing decay rate with the surface conductivity and presented methods to calculate the decay rate using perturbation theory and Poynting's theorem. We demonstrated that the surface conductive absorber is orders of magnitude more effective than the volume conductive absorber, and showed an asymptotic power-law convergence of the transition reflection with respect to the length of the absorber to verify that the smoothness of conductivity function determines the transition reflection.

The major advantages of the surface conductive absorber are: (1) the varying surface conductivity is easily implemented in BEM and can significantly reduce the transition reflections; and (2) the volume properties of the absorber are the same as the waveguide, so there is no interior cross section to discretize, eliminating a potential source of numerical reflections.

We further implemented the surface conductive absorber for terminating a periodic sinusoidal-shape waveguide. We showed that small reflections can be obtained with a short surface absorber when the waveguide is excited with a large group-velocity mode. However, the same-length absorber will generate large reflections if excited

with a smaller group-velocity mode. We showed that the length of the absorber is required to increase according to a power law as the group velocity decreases in order to obtain the same transition reflection. This provides guidance for choosing the absorber length with different excitations. Numerical experiments verified our analytical predictions.

Appendix A

Gaussian Beam Generated by a Dipole in A Complex Space

In this thesis, we mainly use a Gaussian beam as an excitation for waveguide channels in the simulation using boundary element methods to avoid large radiation waves inevitably excited. Since we had codes of excitations from a dipole, it is easier to implement the Gaussian beam generated by a dipole in a complex space. In this section, we show the derivation of the Gaussian beam due to a point current source in a complex coordinate system by following [63, 64].

For simplicity, but without loss of generality, we assume the source current is located at the origin of a homogeneous space. The Green's function of potentials in the space is the same as in (2.29), and it is

$$G(r) \sim \frac{e^{-jkr}}{r}, \tag{A.1}$$

where $r = \sqrt{x^2+y^2+z^2} = z\sqrt{1+(x^2+y^2)/z^2}$, and k is the wavenumber in the homogeneous space. We discuss the fields of the Gaussian beam generated by a dipole by splitting into far fields and near fields, due to different approximation tricks.

A.1 Far Fields

Assume the Gaussian beam propagates in the z direction. For far field ($|z| \gg 0$), since the fields are expected to focus in the vicinity close to the z axis, where $|x| \ll |z|, |y| \ll |z|$, we are allowed to make the paraxial approximation with first-order accuracy, and we obtain

$$\sqrt{1 + (x^2 + y^2)/z^2} \approx 1 + \frac{1}{2}\frac{x^2 + y^2}{z^2}, \tag{A.2}$$

and the distance r becomes

$$r = z + \frac{x^2 + y^2}{2z}. \tag{A.3}$$

We further approximate the distance r in the denominator of (A.1) with z, because the denominator is much less sensitive than the phase term, and substitute the r in the phase term of (A.1) with (A.3), and this yields

$$G(r) \sim \frac{1}{z} e^{-jk(z + \frac{x^2+y^2}{2z})} = \frac{1}{z} e^{-jk(\frac{x^2+y^2}{2z})} e^{-jkz}. \tag{A.4}$$

To generate the Gaussian beam propagating in the z direction, let $z = z + jb$. The Green's function becomes

$$G(r) \sim \frac{1}{z + jb} e^{-jk\frac{x^2+y^2}{2(z+jb)}} e^{-jkz} e^{kb}, \tag{A.5}$$

in which the coefficient can be written in an exponential form

$$\frac{1}{z + jb} = A e^{j\Phi(z)}, \tag{A.6}$$

and the real and imaginary parts of the first phase term in (A.5) can be separated as

$$-jk(\frac{x^2 + y^2}{2(z + jb)}) = -j\frac{k}{2}\frac{z}{z^2 + b^2}(x^2 + y^2) - \frac{kb}{2(z^2 + b^2)}(x^2 + y^2). \tag{A.7}$$

Define z-dependent terms $R(z)$ and $w(z)$

$$\frac{1}{R(z)} = \frac{z}{z^2+b^2} \tag{A.8}$$

$$w^2(z) = \frac{2(z^2+b^2)}{kb} \tag{A.9}$$

Then substituting $R(z)$ and $w(z)$ into (A.5) yields the potentials of the far fields of the Gaussian beam

$$G(r) \sim Ae^{kb}e^{-\frac{x^2+y^2}{w^2(z)}}e^{j\Phi(z)}e^{\frac{-jk(x^2+y^2)}{2R(z)}}e^{-jkz} \tag{A.10}$$

As seen in (A.10), the term $e^{-\frac{x^2+y^2}{w^2(z)}}$ determines the waist of the Gaussian beam along the z direction.

A.2 Near Fields

Since the equation (A.2) does not hold for the region close to the origin (source location), we need to derive the fields in this region in another way. The distance r is rewritten as

$$r = \sqrt{x^2+y^2+(z+jb)^2} = \sqrt{x^2+y^2+z^2-b^2+2jbz} = \beta + j\alpha, \tag{A.11}$$

and substituting it into the Green's function yields

$$G(r) \sim \frac{e^{-jk\beta+k\alpha}}{\beta+j\alpha}. \tag{A.12}$$

Consider the real and imaginary parts β and α of r in (A.11), which is the square root of a complex number. The square root of a complex function has discontinuities at certain axis depending on the choice of the principle value region. To guarantee the wave propagating outwards, β is required to be positive, and therefore, in (A.11), the principle value region in the complex domain should be $[-\pi, \pi]$ and the discontinuity of the square root occurs at the negative real axis. Thus the discontinuity of r in

(A.11) occurs at

$$x^2 + y^2 < b^2, \tag{A.13}$$

$$z = 0, \tag{A.14}$$

which represents a circular disk lying at the xy plane perpendicular to the beam propagating direction, with the center at the point source and radius b. On the two sides of this disk ($z = 0^+$ and $z = 0^+$), the values of r are discontinuous. The discontinuity of r leads to the discontinuity of the Green's function across the disk. The discontinuity of the potential implies that the point source in the complex coordinate has an equivalent source distribution on the circular disk in the real coordinate system. The beam is equivalently excited by this circular distributed source.

Furthermore, the sign of α in (A.11) is determined by the sign of the term bz, and it's obvious that they have the same sign, specifically, $\alpha > 0$, when $bz > 0$; and $\alpha < 0$, when $bz < 0$. According to (A.12), in the region where z has the same sign as b, the resulting positive α leads to large potentials, while in the region where bz is negative, the negative α leads to an exponentially small a potential. Therefore, the beam due to the point source in the complex coordinate is focused on one direction in the propagating axis z, and the direction is determined by the sign of the imaginary part b of the complex coordinate.

A.3 Numerical Illustrations

After the potentials are obtained, electric and magnetic field can be calculated from the potentials following (2.23)–(2.24). Here, we calculate the electric fields due to a point current source $J\hat{y}$ located at the origin in a free space, while the z coordinate is complex. The free-space wavelength λ is used as the dimension unit.

Figure A-1 shows the two non-zero components of the electrical fields at the yz plane where $x = 0$, and $b = 4\lambda$. As predicted in the last section, the beam is focused in the positive z direction. The waist of the beam gradually increases as propagating

along the z axis. We further show the electric fields, respectively, at $z = 0^+$ and $z = 0^-$ along the y axis in Fig. A-2. It is clearly seen that the fields on the two sides of $z = 0$ are discontinuous from $y = -4\lambda$ to $y = 4\lambda$, where the equivalent circular disk source is located. Beyond the region of $-4\lambda < y < 4\lambda$, the fields are continuous across the plane $z = 0$.

Figure A-3 shows the electric fields in the yz plane, when $b = 0.5\lambda$. The field diverges more in the x, y direction, and relatively more energy appears in the $-z$ direction. This is not surprising because when b is close to zero, the field pattern would be close to the pattern due to a point source in the real coordinate.

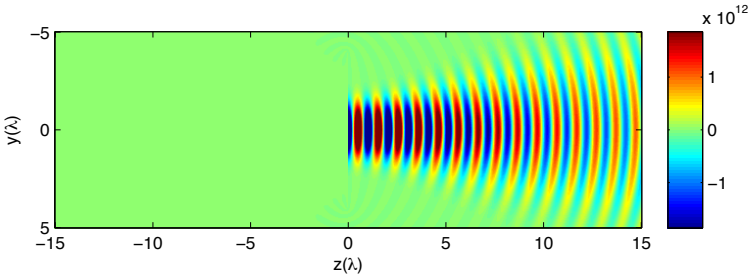

(a) E_y

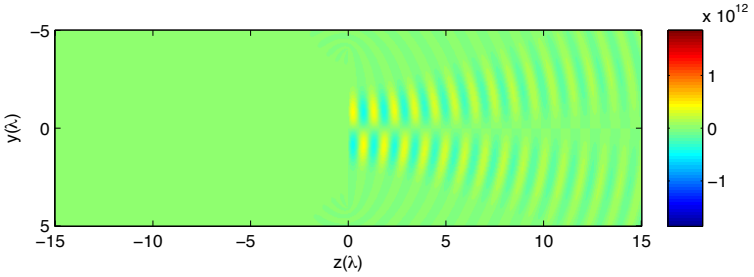

(b) E_z

Figure A-1: Electric fields in the yz plane due to a point current source at the origin in a complex coordinate, $b = 4\lambda$.

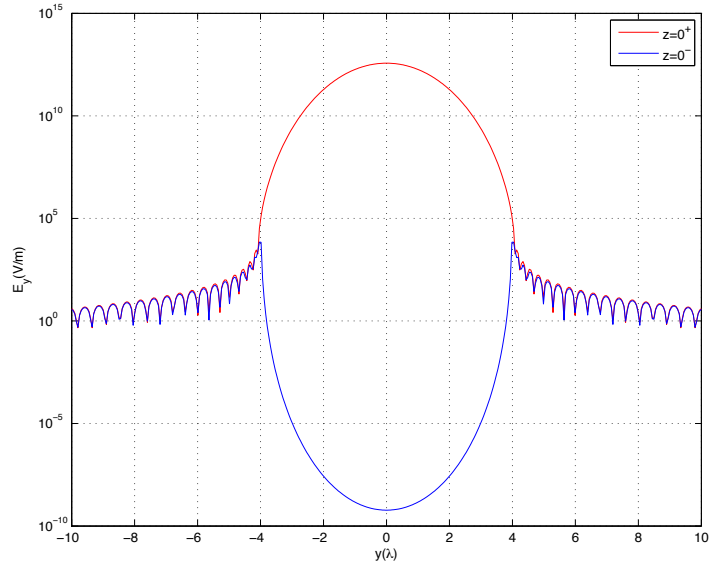

(a) E_y

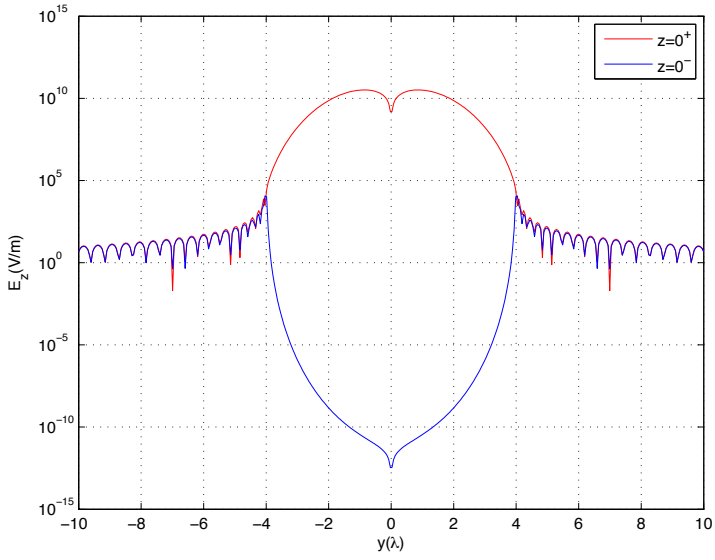

(b) E_z

Figure A-2: The electric fields at $z = 0^+$ and $z = 0^-$ along the y axis due to a point current source at the origin in a complex coordinate, showing the discontinuity of the electric fields across the $z = 0$ plane, and $b = 4\lambda$.

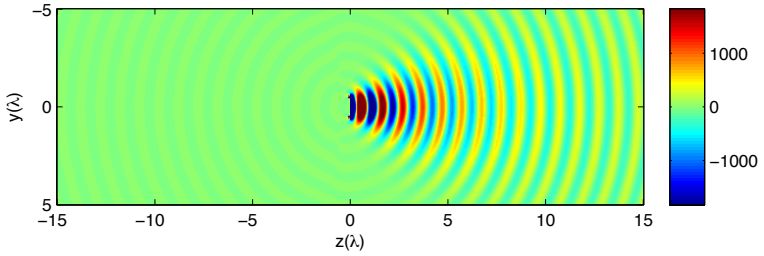

(a) E_y

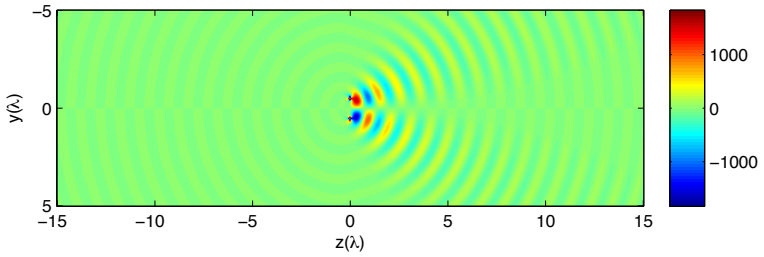

(b) E_z

Figure A-3: Electric field in the yz plane due to a point current source at theorigin in a complex coordinate, and $b = 0.5\lambda$.

Bibliography

[1] S. M. Rao, D. R.Wilton, and A. Glisson, "Electromagnetic scattering by surfaces of arbitrary shape," *IEEE Trans. Antennas Propagat.*, vol. 30, pp. 409–418, May 1982.

[2] J. D. Joannopoulos, S. G. Johnson, J. N. Winn, and R. D. Meade, *Photonic Crystals: Molding the Flow of Light*, 2nd ed. Princeton University Press, 2008.

[3] Y. Xu, R. K. Lee, and A. Yariv, "Propagation and second-harmonic generation of electromagnetic waves in a coupled-resonator optical waveguide," *J. Opt. Soc. Am. B*, vol. 17, no. 3, pp. 387–400, 2000.

[4] M. Soljacic, S. G. Johnson, S. Fan, M. Ibanescu, E. Ippen, and J. D. Joannopoulos, "Photonic-crystal slow-light enhancement of nonlinear phase sensitivity," *J. Opt. Soc. Am. B*, vol. 19, no. 9, pp. 2052–2059, 2002.

[5] H. Altuga and J. Vuckovicb, "Experimental demonstration of the slow group velocity of light in two-dimensional coupled photonic crystal microcavity arrays," *Appl. Phys. Lett*, vol. 86, 2005.

[6] M. L. Povinelli, S. G. Johnson, and J. D. Joannopoulos, "Slow-light, band-edge waveguides for tunable time delays," *Optics Express*, vol. 13, no. 18, pp. 7145–7159, 2005.

[7] R. Ramaswami and K. N. Sivarajan, *Optical Networks: A Practical Perspective,*, 2nd ed. Morgan Kaufmann, 2001.

[8] A. Y. Petrov and M. Eich, "Zero dispersion at small group velocities in photonic crystal waveguides," *Appl. Phy. Lett.*, vol. 85, p. 4866, 2004.

[9] D. Mori and T. Baba, "Wideband and low dispersion slow light by chirped photonic crystal coupled waveguide," *Opt. Express*, vol. 13, no. 23, pp. 9398–9408, 2005.

[10] L. H. Frandsen, A. V. Lavrinenko, J. Fage-Pedersen, and P. I. Borel, "Photonic crystal waveguides with semi-slow light and tailored dispersion properties," *Optics Express*, vol. 14, no. 20, pp. 9444–9450, 2006.

[11] D. Mori, S. Kubo, H. Sasaki, and T. Baba, "Experimental demonstration of wideband dispersion-compensated slow light by a chirped photonic crystal directional coupler," *Opt. Express*, vol. 15, no. 9, pp. 5264–5270, 2007.

[12] S. Kubo, D. Mori, and T. Baba, "Low-group-velocity and low-dispersion slow light in photonic crystal waveguides," *Opt. Lett.*, vol. 32, no. 20, pp. 2981–2983, 2007.

[13] K. O. Hill and G. Meltz, "Fiber Bragg grating technology fundamentals and overview," *J. lightwave Technol.*, vol. 15, no. 8, pp. 1263–1276, 1997.

[14] R. F. Harrington, "Boundary integral formulations for homogeneous material bodies," *Journal of Electromagnetic Waves and Applications*, vol. 3, no. 1, pp. 1–15, 1989.

[15] K. Umashankar, A. Taflove, and S. M. Rao, "Electromagnetic scattering by arbitrary shaped three-dimensional homogeneneous lossy dielectric objects," *IEEE Trans. Antennas Propagat.*, vol. 34, no. 6, pp. 758–765, June 1986.

[16] C. F. Wang, F. Ling, and J. M. Jin, "A fast full-wave analysis of scattering and radiation from large finite arrays of microstrip antennas," *IEEE Trans. Antennas Propagat.*, vol. 46, pp. 1467–1474, Oct. 1998.

[17] X. Q. Sheng, J.-M. Jin, J. Song, W. C. Chew, and C.-C. Lu, "Solution of combined-field integral equation using multilevel fast multipole algorithm for scattering by homogeneous bodies," *IEEE Trans. Antennas Propagat.*, vol. 46, no. 11, pp. 1718–1726, 1998.

[18] K. S. YEE, "Numerical solution of initial boundary problems involving Maxwell's equations in isotropic media," *IEEE Trans. Antennas Propagat.*, vol. 14, pp. 302–307, 1966.

[19] A. Taflove, *Computational Electrodynamics: the Finite-difference Time-Domain Method*. Artech House, 1995.

[20] J. P. Berenger, "A perfectly matched layer for the absorption of electromagnetic waves," *J. Comp. Phy.*, vol. 114, pp. 185–200, 1994.

[21] W. C. Chew and W. Weedon, "A 3D perfectly matched medium from modified maxwell's equations with stretched coordinates," *Microwave Opt. Technol. Lett.*, vol. 7, no. 13, pp. 599–604, 1994.

[22] Z. S. Sacks, D. M. Kingsland, R. Lee, and J.-F. Lee, "A perfectly matched anisotropic absorber for use as an absorbing boundary condition," *IEEE Trans. Antennas Propagat.*, vol. 43, no. 12, pp. 1460–1463, 1995.

[23] S. D. Gedney, "An anisotropic perfectly matched layer-absorbing medium for the truncation of FDTD lattices," *IEEE Trans. Antennas Propagat.*, vol. 44, no. 12, pp. 1630– 1639, 1996.

[24] A. F. Oskooi, L. Zhang, Y. Avniel, and S. G. Johnson, "The failure of perfectly matched layers, and towards their redemption by adiabatic absorbers," *Optics Express*, vol. 16, pp. 11 376–11 392, 2008.

[25] P. Sanchis, P. Bienstman, B. Luyssaert, R. Baets, and J. Marti, "Analysis of butt coupling in photonic crystals," *IEEE J. Quantum Elec*, vol. 40, no. 5, pp. 541–550, 2004.

[26] J. R. Phillips and J. K. White, "A precorrected-FFT method for electrostatic analysis of complicated 3-D structures," *IEEE Trans. Computer-Aided Design*, vol. 16, pp. 1059–1072, 1997.

[27] Z. Zhu, B. Song, and J. White, "Algorithms in fastimp: a fast and wideband impedance extraction program for complicated 3-D geometries," in *Proceedings of DAC*, 2003, pp. 712–717.

[28] L. Zhang, N. Yuan, M. Zhang, L. W. Li, and Y. B. Gan, "RCS computation for a large array of waveguide slots with finite wall thickness using the mom accelerated by p-fft algorithm," *IEEE Trans. Antennas Propagat.*, vol. 53, no. 9, pp. 3101– 3105, 2005.

[29] J. Song, C.-C. Lu, and W. C. Chew, "Multilevel fast multipole algorithm for electromagnetic scattering by large complex objects," *IEEE Trans. Antennas Propagat.*, vol. 45, no. 10, pp. 1488–1493, 1997.

[30] J. Y. Wu, D. M. Kingsland, J. F. Lee, and R. Lee, "A comparison of anisotropic PML to berenger's pml and its application to the finite-element method for EM scattering," *IEEE Trans. Antennas Propagat.*, vol. 45, no. 1, pp. 40– 50, 1997.

[31] D. H. Schaubert, D. R. Wilton, and A. W. Glisson, "A tetrahedral modeling method for electromagnetic scattering by arbitrarily shaped inhomogeneous dielectric bodies," *IEEE Trans. Antennas Propagat.*, vol. 32, no. 1, pp. 77–85, 1984.

[32] D. Pissoort and F. Olyslager, "Termination of periodic waveguides by PMLs in time-harmonic integral equation-like techniques," *IEEE Antennas and Wireless Propagat. Letters*, vol. 2, pp. 281–284, 2003.

[33] S. G. Johnson and J. D. Joannopoulos, "Block-iterative frequency-domain methods for maxwell's equations in a planewave basis," *Optics Express*, vol. 8, no. 3, pp. 173–190, 2001.

[34] D. M. Pozar, "Improved computational efficiency for the moment method solution of printed dipoles and patches," *Electromagn.*, vol. 3, pp. 299–309, Sept. 1984.

[35] K. L. Wu, M. Spenuk, J. Litva, and D. G. Fang, "Theoretical and experimental study of feed network effects on the radiation pattern of series fed microstrip antenna arrays," *Proc. Inst. Elect. Eng.*, vol. 138, pp. 238–242, June 1991.

[36] Y. Zhuang, K. L. Wu, C. Wu, and J. Litva, "A combined full wave CGFFT method for rigorous analysis of large microstrip antenna arrays," *IEEE Trans. Antennas Propagat.*, vol. 44, pp. 102–109, Jan. 1996.

[37] F. Ling and J. M. Jin, "Scattering and radiation of microstrip antennas using discrete complex image method and reciprocity theorem," *Microwave & Optical Technology Lett.*, vol. 16, pp. 212–216, 1997.

[38] L. N. Medgyesi-Mitschang, J. M. Putnam, and M. B. Gedera, "Generalized method om moments for three-dimensional penetrable scatterers," *J. Opt. Soc. Am. A*, vol. 11, no. 4, pp. 1383–1398, 1994.

[39] L. Zhang, "A fast 3d full-wave solver for nano-photonics," Master's thesis, MIT, 2007.

[40] B. H. Jung, T. Sarkar, and Y. S. Chung, "A survey of various frequency domain integral equations for the analysis of scattering from three-dimensional dielectric objects," *Progress In Electromagnetics Research*, vol. 36, pp. 193–246, 2002.

[41] H. C. V. D. Hulst, *Light scattering by small particles.* John Wiley & Sons, Inc, 1957.

[42] M. Kerker, *The scattering of light and other electromagnetic radiation.* Academic Press, 1969.

[43] C. F. Bohren and D. R. Huffman, *Absorption and Scattering of Light by Small Particles.* John Wiley & Sons, Inc, 1983.

[44] M. Born and E. Wolf, *Principles of Optics, electromagnetic theory of propagation, interference and diffraction of light*, 6th ed. Pergamon Press, 1984.

[45] J. R. Phillips and J. K. White, "A precorrected-FFT method for capacitance extraction of complicated 3-D structures," in *Proc. Int. Conf. Computer-Aided Design*, Santa Clara, CA, 1994, pp. 268–271.

[46] N. Yuan, T. S. Yeo, X. C. Nie, and L. W. Li, "A fast analysis of scattering and radiation of large microstrip antenna arrays," *IEEE Trans. Antennas Propagat.*, vol. 51, no. 9, pp. 2218–2216, Sept. 2003.

[47] X. C. Nie, L. W. Li, and N. Yuan, "Precorrected-FFT algorithm for solving combined field integral equations in electromagnetic scattering," *J. Electromagn. Waves Appl.*, vol. 16, no. 8, pp. 1171–1187, Aug. 2002.

[48] X. C. Nie, L. W. Li, N. Yuan, and T. S. Yeo, "Fast analysis of scattering by arbitrarily shaped three-dimensional objects using the precorrected-FFT method," *Microwave Opt. Technol. Lett.*, vol. 34, no. 6, pp. 438–442, Sept. 2002.

[49] X. C. Nie, L. W. Li, N. Yuan, T. S. Yeo, and Y. B. Gan, "A fast analysis of arbitrarily shaped homogeneous dielectric objects," *Microwave Opt. Technol. Lett.*, vol. 38, no. 1, pp. 30–34, July 2003.

[50] R. Coifman, V. Rokhlin, and S. Wandzura, "The fast multipole method for the wave equation: A pedestrian prescription," *IEEE Antennas Propag. Mag.*, vol. 35, pp. 7–12, 1993.

[51] D. Marcuse, *Theory of Dielectric Optical Waveguides*, 2nd ed. Academic Press, 1991.

[52] S. G. Johnson, P. Bienstman, M. A. Skorobogatiy, M. Ibanescu1, E. Lidorikis, , and J. D. Joannopoulos, "Adiabatic theorem and continuous coupled-mode theory for efficient taper transitions in photonic crystals," *Phys. Rev. E*, vol. 66, p. 066608, 2002.

[53] R. F. Harrington, *Time-Harmonic Electromagnetic Fields*. McGraw-Hill Book Company, 1961.

[54] K.-M. Chen, "A mathematical formulation of the Equivalence principle," *IEEE Trans. Microwave Theory Tech.*, vol. 37, no. 10, pp. 1576– 1581, 1989.

[55] R. F. Harrington, *Field computation by moment methods*. Macmillan, 1968.

[56] L. N. Trefethen and D. Bau, *Numerical Linear Algebra*. SIAM, 1997.

[57] D. R. Wilton, S. M. Rao, A. W. Glisson, D. H. Schaubert, O. M. Al-Bundak, and C. M. Butler, "Potential integrals for uniform and linear source distributions on polygonal and polyhedral domains," *IEEE Trans. Antennas Propagat.*, vol. 32, pp. 276–281, 1984.

[58] M. A. Khayat and D. R. Wilton, "Numerical evaluation of singular and near-singular potential integrals," *IEEE Trans. Antennas Propagat.*, vol. 53, pp. 3180–3190, 2005.

[59] J. H. Lee and J. White, "Complex-domain mapping for evaluating troublesome integrals in fast full-wave integral equation solvers," in *Microwave Symposium Digest, IEEE MTT-S International*, Atlanta, June 2008, pp. 1345–1348.

[60] J. H. Lee, "Fast methods for inverse wave scattering problems," Ph.D. dissertation, MIT, 2008.

[61] J. D. Jackson, *Classical Electrodynamics*, 3rd ed. Wiley, 1998.

[62] G. B. Arfken and H. J. Weber, *Mathematical Methods for Physicists*, 6th ed. Academic Press, 2005.

[63] H. A. Haus, *Waves and fields in optoelectronics*. Prentice-Hall Inc., 1984.

[64] E. Erez and Y. Leviatan, "Electromagnetic scattering analysis using a model of dipoles located in complex space," *IEEE Trans. Antennas Propagat.*, vol. 42, pp. 1620–1624, 1994.

[65] C. V. Loan, *Computational Frameworks for the Fast Fourier Transform.* Society for Industrial and Applied Mathematics, 1992.

[66] G. Strang, "A proposal for Toeplitz matrix calculations," *Studies in Applied Mathematics*, vol. 74, pp. 171–176, 1986.

[67] T. F. Chan, "An optimal circulant preconditioner for Toeplitz systems," *SIAM journal on scientific and statistical computing*, vol. 9, no. 4, pp. 766–771, 1988.

[68] T. F. Chan and J. A. Olkin, "Circulant preconditioners for Toeplitz-block matrices," in *SIAM Conference on Linear Algebra in Signals, Systems, and Control*, 1990, pp. 89–101.

[69] W. C. Chew, *Waves and Fields in Inhomogeneous Media.* New York: Van Nostrand, 1990.

[70] A. Ishimaru, *Electromagnetic Wave Propagation, Radiation, and Scattering.* Englewood Cliffs, New Jersey: Prentice-Hall, 1991.

[71] V. A. Mandelshtam and H. S. Taylor, "Harmonic inversion of time signals and its applications," *J. Chem. Phys.*, vol. 107, no. 17, pp. 6756–6769, 1997.

[72] S. G. Johnson, "Harminv software package," http://ab-initio.mit.edu/harminv.